Structural evolution of protective coatings for γ-TiAl based alloys

Dipl.-Ing. Martin Moser

Being a thesis in partial fulfilment of the requirements for the degree of a

Doctor of Montanistic Sciences (Dr.mont.)

at the University of Leoben

Leoben, May 2008

Affidavit

I declare in lieu of oath, that I wrote this thesis and performed the associated research by myself, using only literature cited in this volume.

Leoben, May 2008

Martin Moser

Acknowledgments

The successful completion of my PhD thesis was only achieved with the support and help of many people who made work and private life enjoyable during these years. Here is the right place for thanking them.

First of all I have to express my sincerest gratitude to my supervisor and friend Paul Mayrhofer. His knowledge, enthusiasm and passion for science as well as his endurance helping me solve problems were a great motivation. Without his guidance, advice and encouraging words this project would not have been possible. Our *Country* sessions and fruitful discussions there will not be forgotten.

I am very grateful to my diploma students Lukas Hädicke, Richard Rachbauer, and especially to my student coworkers Nezameddin Fateh, Birgit Grossmann, and Peter Raninger. Their dedication and commitment has been an immense support.

Also I am very indebted to all my coauthors for their valuable contribution to this thesis – Peter B. Barna, Reinhold Braun, Helmut Clemens, Mark W. Rainforth, Ian M. Ross, György Sáfrán, and Lajos Székely.

Many thanks to my friends, who accompanied me all these years throughout my studies and in the beginning of my PhD - Michael Bischof, Harald Chladil, Gert Gassner, Kerstin Kutschej, and Josef Wagner. They made the decision of starting a thesis in Leoben easy, and their assistance and "insider" knowledge eased many hurdles.

Special thanks to all my colleagues and friends of the Department of Physical Metallurgy, notably to Gerardo Fontalvo, Harald Köstenbauer, Martin Pfeiler and my office and project mates Jörg Paulitsch, Claudia Walter, and Florian Rovere for all the great times we shared during and off work. Further I want to thank Christian Mitterer for giving me the opportunity to learn from his experience.

Inexpressible thanks to my parents, my sister and my girlfriend Andrea, who motivated and encouraged me during the whole time. At the end of the day it was always them, who had to endure the stressed and weekend-working Martin, who cheered me up after setbacks or shared my happiness after successes. Without them it would have never been possible to reach this goal.

Table of Contents

1 Introduction

Within the last hundred years the global air temperature near the Earth's surface has risen by 0.74 °C [1]. Most scientists agree that the main cause of global warming since the mid-twentieth century is the increase in anthropogenic greenhouse gas emissions. One of the most important sources for these emissions is the combustion of fossil fuels [2]. Apart from the development of new and environmentally friendly concepts for power generation, existing technologies have to be improved to allow for a more effective and sustained utilization of fossil fuels with concomitantly reduced greenhouse gas emissions. This effort requires new developments in all fields of engineering, but will ultimately lead to the demand for new material design and application concepts.

Aviation is estimated to account for 3.5% of the total anthropogenic climate change [3]. Although aircraft are today more than 70% more fuel efficient per passenger-kilometer than 40 years ago, improvements in efficiency of additional 40 to 50% are anticipated by 2050 [3]. This progress can only be realized by the extensive application of new materials in aircraft design.

Replacing heavy steels or Ni-base superalloys in aircraft turbines gives rise to tremendous weight savings, and thus increases in turbine efficiency. Possible replacement candidate materials are titanium-aluminum alloys based on the intermetallic gamma (γ) –phase, so called γ-Titan-Aluminides (γ-TiAl). This class of alloys offers a 55% lower specific-mass and a 50% higher specific modulus and density-adjusted stiffness as compared to currently used materials [4]. Therefore, γ-TiAl is going to be used in next generation aircraft engines and flight tests are currently undertaken with γ-TiAl blades installed in the low-pressure section of a turbine [5].

Microstructural control and γ-TiAl alloy modification would allow for an application at temperatures up to 850 °C, however the poor long-term oxidation and corrosion resistance as well as limited wear and erosion protection at temperatures above 750 °C prohibit a wider utilization. As a consequence, coating systems have to be developed that provide efficient environmental protection and thermal insulation over the anticipated component lifetime.

Such coatings can only be realized on a basis of knowledge related to the synthesis-microstructure-property interplay and to the fundamental phenomena and pathways of structure formation in the selected coating materials. Therefore the aim of this thesis is to develop innovative coating systems, which can provide an effective and sustained protection for γ-TiAl, to identify optimal film compositions and processing routes, and to assess the interaction between the coatings and γ-TiAl. In accordance, two inherently different systems, a metallic coating based on the intermetallic Al_2Au phase, and a ceramic transition-metal Ti-Al-N based film, were chosen for development.

Metallic coatings based on intermetallic Ni-Al or Pt-Al phases have been successfully established in the surface protection of Ni-base superalloys [6]. Also, bulk Al-Au has high oxidation stability [7, 8]. Moreover, with their distinct coloration Al-Au coatings can be used as signal layers in critical components, which would optically indicate the need for refurbishment or the endpoint of utilization.

Due to their excellent ability of protecting components from corrosion and wear, Ti-Al-N coatings have found their way into a wide range of applications [9]. Alloying reactive elements such as yttrium is suggested to further improve mechanical properties, oxidation resistance and oxide scale adherence of bulk and coating materials [10-12]. Thus, the influence of varying amounts of the reactive element Y on structural, mechanical and protective properties of monolithically grown Y is investigated in detail.

The following chapters of this thesis provide a summary of the research activities and give an introduction into the used deposition and analyses techniques. Further, they contain results which are not included in the main experimental research outlined in the scientific publications presented at the end of this work.

Detailed results of microstructure and mechanical properties, as well as of the thermal stability of Al-Au coatings are presented in publication I and II, respectively. In publication III the oxidation resistance of the Al-Au films is discussed. The influence of Y addition on microstructure and composition of $Ti_{1-x}Al_xN$ is presented in publications IV. Publication V demonstrates that single-phase cubic $(Ti_{1-x}Al_x)_{1-y}Y_yN$ coatings can be grown by bipolar pulsed DC magnetron sputtering, and the influence of pulse parameters on the plasma, and film microstructure and mechanical properties is described. In publication VI the influence of coating and oxidation on the 4-point bending strength of a γ-TiAl based alloy is investigated.

2 Gamma-Titanium Aluminides

γ-TiAl based alloys exhibit numerous attractive properties which can fulfill the demand in advanced energy conversion systems for improved efficiency and ecologic compatibility through higher service temperatures, lighter weight, and higher operation speeds. Among these properties are the low density ($\rho \sim 3.8$ g/cm^3), high specific yield strength ($R_{p0.2}/\rho$), high specific elastic modulus (E/ρ), and good creep properties up to high temperatures [13, 14]. γ-TiAl alloys of engineering interest are composed of two intermetallic phases γ-TiAl (ordered face-centered tetragonal L1$_O$ structure) and α$_2$-Ti$_3$Al (ordered hexagonal DO$_{19}$ structure). The ductility and strength of two-phased γ-TiAl based alloys are controlled by the composition and microstructure [15]. Room temperature ductility varies with the Al-content and has a maximum around the two-phase composition Ti-48Al (in at.%). Therefore, γ-TiAl alloys of engineering interest are commonly based on Ti-(45-48)Al [15, 16]. Cr, Mn, and V, can further increase the ductility of γ-TiAl [17]. Better creep resistance through solid solution strengthening and oxidation protection is achieved by alloying Mo, W, Ta, and/or Nb [16-18]. Additions of B, Si, and C yield precipitation hardening and improve high temperature strength and creep resistance [19, 20]. Consequently, the composition of current γ-TiAl based alloys can be expressed as follows [13, 21]:

Ti – (45-48)Al – (1-4){Cr, Mn, V} – (1-10){Mo, W, Ta, Nb} – (0-1){B, Si, C}   (in at.%)

The microstructure and consequently mechanical properties of two-phased γ-TiAl based alloys may be adjusted within wide limits by appropriate heat treatments and thermomechanical processing. These microstructures are classified into *duplex*, consisting of a mixture of equiaxed γ-TiAl and lamellar grains, *nearly-lamellar*, composed of finely dispersed γ-TiAl grains in a lamellar grain-matrix, *fully-lamellar*, which has a coarse microstructure of grains or colonies of alternate γ-TiAl layers and α$_2$-Ti$_3$Al platelets in a defined crystallographic relation, and *near-gamma*, showing fine equiaxed γ-TiAl grains with dispersed α$_2$-Ti$_3$Al particles on the γ-TiAl grain boundaries [15].

Within this thesis, coatings were deposited on two different γ-TiAl based alloys, Ti-45Al-8Nb and Ti-47Al-2Cr-0.2Si. The former belongs to the class of high Nb containing so-called TNB-class alloys [22]. These alloys have yield strengths ($R_{p0.2}$) of up to 1000 MPa combined with plastic strains of ~2% at room temperature. Further, they show good

oxidation resistance and can subsequently be applied up to temperatures of 700 °C [21]. The typical microstructure of the Ti-45Al-8Nb alloy is presented in the polarized light micrograph in Fig. 2.1a. The TNB alloy has a very fine grained near-gamma structure. The average grain size is 5 µm.

The Ti-47Al-2Cr-0.2Si alloy exhibits a high room temperature ductility and excellent superplastic properties at elevated temperatures. However, due to the absence of Nb, Ta, or W the inherent oxidation resistance is poor [23]. As shown in the polarized light micrograph in Fig. 2.1b this alloy has a fine-grained, near-gamma microstructure with an average size of γ-grains of ~20 µm.

Generally it has to be remarked that the microstructure of the TNB alloy represents the material in the as extruded state, whereas the Ti-47Al-2Cr-0.2Si sheet has a microstructure as presented at the end of the processing route.
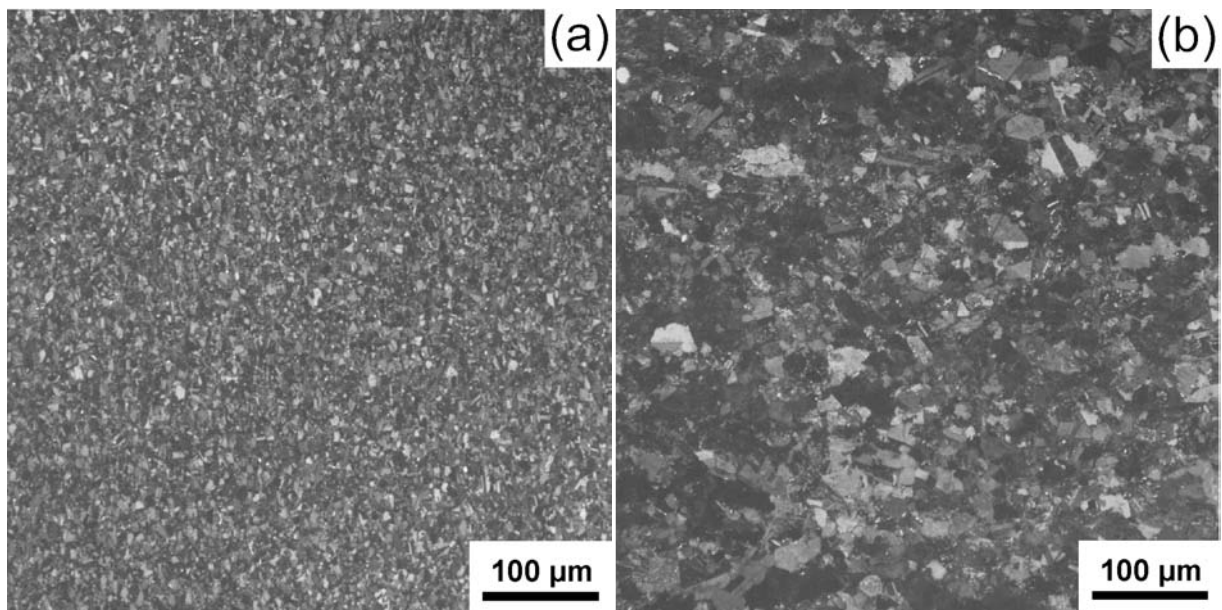

Fig. 2.1. Polarized light images of the typical microstructure of Ti-45Al-8Nb (a) and Ti-47Al-2Cr-0.2Si (b)

3 Coatings

Inherent properties of titanium based intermetallics, like the low ductility at room temperature, as compared to superalloys or steels, and the high diffusibility of Ti, requires the development of innovative, new and tailor made protective coating systems. Attention needs also to be paid on the coating process itself as interdiffusion during high temperature application could lead to intolerably high decreases in γ-TiAl mechanical properties [23, 24].

Two coating systems, developed and investigated within this thesis, are presented in the following.

3.1 Metallic Films

Surface oxidation and corrosion protection of Ni-based superalloys through the formation of intermetallic compounds from the Ni-Al, Cr-Al or Pt-Al systems have been commercially viable processes for many years [6]. Also, bulk Al_2Au is reported to be fairly resistant against oxidation [7, 8]. Therefore, films from the Al-Au system are also intended as protective coatings. Further, due to their distinct coloration, Al-Au coatings can act as signal-layers, marking the threshold for component refurbishment or the end of tool lifetime. Showing a reflectivity minimum at a wavelength of 545 nm, Al_2Au is magenta-coloured but depending on the Al/Au ratio the colouration can be adjusted between pink and dark-purple [26, 27].

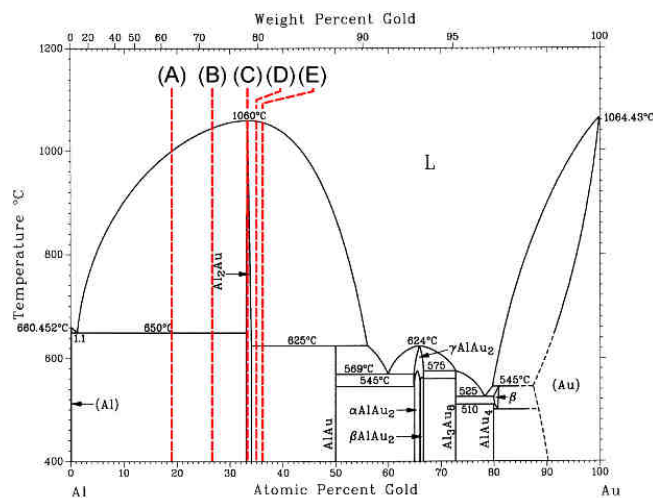
Fig. 3.1. Al-Au binary system [25].The coatings prepared with Al/Au ratios of 4.3 (A), 2.8 (B), 2.0 (C), 1.9 (D), and 1.8 (E) are indicated (Publication I).

The Al-Au system was first investigated and described as early as in the year 1890 by Roberts-Austin, who described the coloured Al_2Au phase and its high melting point [28]. Later, the system was investigated as compound formation in Al-Au bonds resulted in microelectronic component failures [7, 29-33].

According to the binary phase diagram, presented in Fig. 3.1, Al_2Au has a homogeneity range between 32.9 and 33.9 at.% Au at room temperature and a melting point of 1060 °C. Al_2Au crystallizes in the face-centred cubic (fcc) CaF_2 structure in which Al is located in the tetrahedral sites of an fcc unit cell formed by Au atoms (see Fig. 3.2a). As it was demonstrated in publication I by ab initio modelling of the electron density distribution in Al_2Au lattice planes, this intermetallic belongs to the salt-like Zintl phases with Al atoms acting as anionic compounds by building a sublattice which occupies the valence electrons from Au atoms acting as cations [27, 34]. As shown in Fig. 3.2b, between the Al atoms a typical metallic electron density distribution is present, where valence electrons are delocalized in a nearly free and uniform electron gas. In contrast, the Au atoms show a mixture of ionic and covalent binding characters with semi-localized electrons gathering between the Au atoms. In the Al,Au-(110) lattice plane a mixture of metallic, ionic and covalent bindings is present.
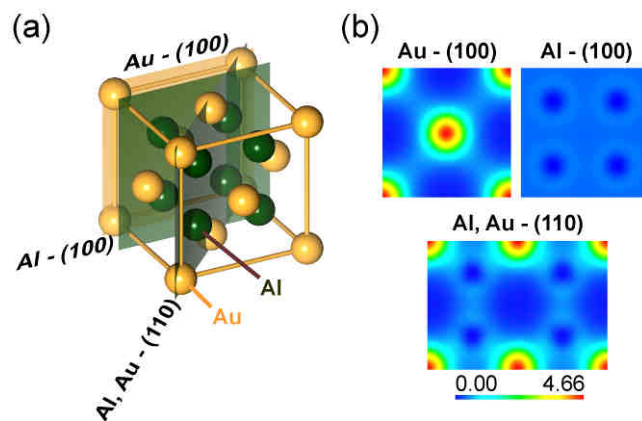

Fig. 3.2. (a) Schematic of the CaF_2 structure of Al_2Au indicating the Au-(100), Al-(100) and Al,Au-(110) crystallographic planes for the (b) ab initio calculated electron density distribution (Publication I [27]).

Within the Al-Au system five coatings with varying Al/Au at.% ratios of 4.3, 2.8, 2.0, 1.9, and 1.8 are investigated. Their composition according to the binary phase diagram is shown in Fig. 3.1. These films exhibit strong differences in their microstructure and hence mechanical, thermal and oxidation protective properties, despite the majority phase in all coatings is Al_2Au. The investigations of the single phase intermetallic Al_2Au films reveal it

with superior structural and mechanical characteristics and with better oxidation and corrosion resistance compared to the coatings having higher Al or Au contents. Further details on the investigations of the Al-Au films are presented in publications I, II, and III [27, 35, 36].

3.2 Nitride Films

Thin films of metal nitrides find widespread application as selective transmission coatings, diffusion barriers in microelectronics, hard wear resistant coatings on cutting tools, or as corrosion and abrasion resistant layers on optical and mechanical components. Especially transition metal nitrides are utilized as their specific bond structure of covalent, metallic, and ionic components is responsible for their excellent properties [9, 37].

Transition metal nitride coatings started their industrial applications about thirty years ago with binary systems like TiN or TiC. Both coatings have been studied extensively and are still heavily applied today. However, these binaries are a basis for the development of advanced ternary, quaternary or multi-nary films which entered industrial application in the early 80s.

3.2.1 Ti-Al-N

With the addition of aluminium to TiN a ternary $Ti_{1-x}Al_xN$ coating was introduced which exhibited excellent machining performance due to the better oxidation resistance, higher hardness and improved thermal stability as compared to TiN [38, 39].

TiN crystallizes in the face-centred cubic B1 rocksalt (NaCl) structure, while AlN is hexagonal B4 wurtzite (ZnS) structured [9, 40]. In thermodynamic equilibrium the solid solubility of AlN in TiN is small and reaches only ~5 mole% at 2750 °C. For higher AlN fractions at lower temperatures the equilibrium composition consist of cubic TiN and hexagonal AlN [41]. However, the extremely high cooling rates of ~10^{-13} K s^{-1}, as well as the limited atomic assembly kinetics during low-temperature plasma-assisted vapour deposition (as described in Chapter 4) allow the formation of supersaturated solid-solution $Ti_{1-x}Al_xN$.

Vapour deposition phase fields for a range of pseudo-binary nitride systems including TiN-AlN were first presented by Holleck [41], who predicted a stability regime in terms of temperature and AlN content at normal vapour deposition temperatures (300 – 700 °C).

Fig. 3.3 presents the structural evolution of $Ti_{1-x}Al_xN$ along the pseudo-binary TiN-AlN tie line. Substitution of Ti atoms with Al atoms in the fcc B1 structure of TiN results in solid-solution cubic $Ti_{1-x}Al_xN$. As a result of the substitution, the TiN lattice parameter *a* decreases from 4.255 to 4.146 Å for $Ti_{0.35}Al_{0.65}N$ due to the smaller size of Al atoms as compared to Ti [9, 42-44]. The maximum solubility limit within the cubic NaCl structure strongly depends on the deposition conditions [9]. Experimental investigations indicate a maximum solubility of ≤65 mole% AlN in fcc TiN [42, 45-48]. Both thermodynamic and ab-initio calculations predict a critical AlN value of ~70 mole% [49-51], and Ref. [44] reports that the metastable phase stability limit can be varied between 65 and 75 mole% by altering the Al distribution in the metal sublattice. Hence, mechanisms that influence the Al distribution during growth will also influence the metastable solubility limit. Generally, with deposition techniques that involve high ionization rates, like arc-evaporation [43, 48, 52] or arc-ion-plating [46] cubic $Ti_{1-x}Al_xN$ coatings with higher AlN mole fractions can be synthesised as compared to conventional magnetron sputtering [45, 53].
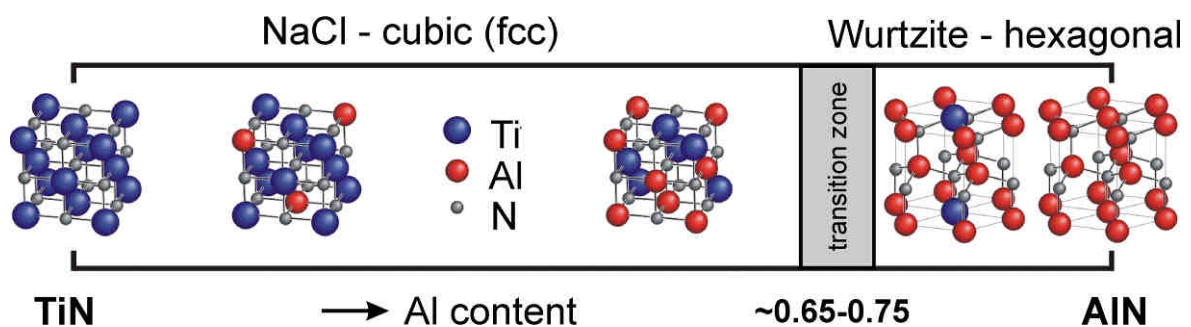

Fig. 3.3. Structural evolution along the pseudo-binary tie line TiN-AlN, analogue to [54]. The transition zone cubic TiN to hexagonal AlN is indicated by the gray area defined as described in literature [42, 44-48, 51].

Exceeding the metastable solubility limit results in the formation of a mixed cubic-NaCl and hexagonal-ZnS structure [42, 44-48, 51]. Above a transition zone, presented in Fig. 3.3, single-phase solid-solution hexagonal $Al_{1-x}Ti_xN$ forms, where Ti atoms substitute for Al in the ZnS-wurtzite unit-cell.

In correspondence to the structural evolution the mechanical, thermal and oxidation protection properties depend on the Al content. The substitution of Ti in the TiN phase by Al results in solid solution hardening (see Chapter 6.1.2). Therefore, hardness values increase from 20-28 GPa for TiN to 30-35 GPa for $Ti_{1-x}Al_xN$ with compositions close to the metastable solubility limit [42, 46, 52]. The elastic modulus exhibits a similar trend and

increases with increasing Al content. Exceeding the metastable solubility limit where the hexagonal phase is formed usually results in a decrease in hardness and modulus due to intrinsically lower mechanical properties of the wurtzite-type phase. Hexagonal AlN has a hardness below 20 GPa and modulus of ~190 GPa [42, 44, 46, 47].

Owing to the formation of a protective Al_2O_3 or $Ti_xAl_yO_z$ layer the oxidation resistance of fcc-$Ti_{1-x}Al_xN$ is increased to above 750 °C as compared to ~600 °C for TiN [42, 55-59]. The oxidation resistance also depends on the AlN mole fraction and can hence be increased with increasing Al content [42]. McIntyre reported of a layered oxide scale consisting of an outer Al_2O_3 scale and an inner TiO_x layer [60]. As oxidation is a time and temperature dependent process (see Chapter 7.1.3). The long-term oxidation behaviour of $Ti_{1-x}Al_xN$ is comparable to bulk Ti-Al alloys. At the initial stages of oxidation a bi-layered oxide scale is formed as described by Ref. [60], however with increasing oxidation time outward diffusion of Ti leads to the formation of a multi-layered scale consisting of a outer TiO_2 layer and an open and interrupted Al_2O_3 scale underneath, followed by a mixed Al_2O_3 + TiO_2 zone [61, 62]. The afore-mentioned case represents however the simplest example and more complex oxide scales can form depending on the alloy system and time/temperature regime.

In $Ti_{1-x}Al_xN$ the oxidation behaviour changes when the metastable solubility limit of AlN is exceeded. As soon as the hexagonal phase is formed, no layered oxide structure is observed. The oxidation resistance is reduced and is comparable to binary AlN [62-64].

3.2.2 Ti-Al-Y-N

Alloying yttrium can increase the oxidation resistance of bulk materials and coatings as it positively influences oxide scale adherence and supports the formation of a stable and dense oxide scale [65, 66]. Reactive elements (RE), such as yttrium, act as oxygen active ions and segregate to scale grain boundaries as well as to the metal-oxide interface due to the oxygen gradient across the scale. The segregation to the metal-oxide interface inhibits interfacial void growth and is therefore improving the oxide scale adhesion. Outward diffusion of RE ions to scale grain boundaries prevents outward cation transport and consequently slows down the oxide scale growth [11, 12, 66-70].

For Ti containing coatings improved corrosion- and oxidation resistance as well as grain refinement was reported when yttrium was alloyed [10, 71, 72].

The systematic investigation of the impact of increasing amounts of Y addition on structural, mechanical and protective properties of $Ti_{0.45}Al_{0.55}N$ coatings was one of the major tasks within this thesis. It is shown that the addition of Y to $Ti_{1-x}Al_xN$ decreases the metastable solubility limit of the cubic NaCl structure. Therefore, DC magnetron-sputtered single-phase cubic-$Ti_{0.45}Al_{0.55}N$ coatings develop a mixed cubic/hexagonal microstructure when 2-5 at.% Y are added, as shown in Fig. 3.4. Alloying 9 at.% Y to the metallic sub-lattice results in the formation of a predominantly hexagonal $(Ti_{1-x}Al_x)_{1-y}Y_yN$ coating [73]. These experimental results are confirmed by ab-initio calculations, as detailed in chapter 5.3.1. Consequently, with increasing ZnS-wurtzite phase fraction, mechanical and thermal properties as well as the oxidation resistance decrease.
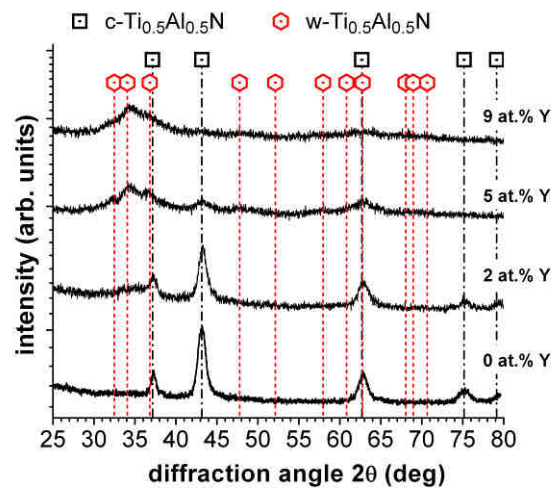

Fig. 3.4. X-ray diffraction pattern of as-deposited $(Ti_{1-x}Al_x)_{1-y}Y_yN$ films containing $y = 0$ ($Ti_{0.45}Al_{0.55}N$), 2 ($Ti_{0.42}Al_{0.56}Y_{0.02}N$), 5 ($Ti_{0.43}Al_{0.52}Y_{0.05}N$), and 9 at.% Y ($Ti_{0.38}Al_{0.53}Y_{0.09}N$) in the metallic sublattice (Publication IV [73]).

Yet, when films with $y = 2$ at.% Y are prepared by bipolar pulsed DC magnetron sputtering, as described in chapter 4.3.2, single-phase NaCl cubic $(Ti_{1-x}Al_x)_{1-y}Y_yN$ coatings can be synthesised [74]. These coatings combine the excellent mechanical properties of cubic-$Ti_{0.45}Al_{0.55}N$ with improved oxidation resistance through the reactive element yttrium.

Further details on the influence of Y and the deposition technique on mechanical and thermal properties are explained later in this thesis in chapters 5.2, 6.2 and 7.2, respectively. The investigations on $(Ti_{1-x}Al_x)_{1-y}Y_yN$ are furthermore discussed in detail in the publication IV and V.

4 Coating Synthesis

4.1 General

Depending on the application of the coated product, a wide variety exists for the formation of overcoats, films, or thin layers. Protective and high temperature resistant coatings are typically applied by thermochemical processes, like pack-cementation, mechano-thermal processes, like thermal or plasma-spraying or by chemical or physical vapour deposition.

In the pack-cementation process components are packed in a mixture of coating material, inert powder, e.g. aluminium oxide, and halide salt in sealed retorts and heated in protective atmosphere inside a furnace. At a given temperature the coating material reacts with the salt to form a metallic halide vapour, which forms the transport species. At the substrate surface the gas decomposes to form the coating by releasing the halide activator, which can then restart the process cycle. Typical temperatures where the modified surface zone forms range from 700 to 1000 °C over a period of several hours [75, 76].

Thermal spraying processes are based on the principle of heating and melting a rod, wire or powder stock, accelerating it by a high velocity stream of compressed air or other gases, which propel the material onto a pre-treated and sometimes heated substrate [77-80]. The plasma spraying process uses the heat of an e.g. Ar plasma (chapter 4.2), created by an electrical arc between electrode and nozzle, to melt the coating species. Here a plasma jet emanating from a plasma torch is used to boost the material towards the substrate [80-82]. The particles there deform and freeze, creating a layered coating which is commonly, rough and porous.

Vapour deposition processes like physical vapour deposition (PVD) and chemical vapour deposition (CVD) find widespread application ranging from the growth of semi-conductors in the micro-electronics industry to the formation of hard, wear resistant films on machining tools and components and are used in aerospace and automotive industry. Vapour deposition processes operate over a wide rage of pressures and temperatures and are characterized by a solid reaction product which nucleates and grows in an environment where vapour phase reactions occur.

In CVD processes the coating material is grown from gaseous precursors which chemically react and dissociated at the substrate surface requiring high thermal activation energies

with usual temperatures above 900°C. One of the most important advantage of the CVD process is to allow for deposition of geometrically complex components and large capacities. The drawback however is that the substrate has to endure the high deposition temperatures and the coating material variety is limited to the availability of precursors and chemical reactants [83-85].

In PVD processes metals, alloys or chemical compounds are evaporated in vacuum from a solid through thermal energy or particle bombardment. Additional elements or compounds can be introduced in the gaseous state, such as O_2, N_2, or CH_4 forming reaction products like oxides, nitrides or carbides in the so-called reactive-PVD process. After transport of the vapours, condensation, and film nucleation at the substrate take place [86]. Allowing substrate temperatures from lower than 100 to above 500 °C, and enabling the depositing of any metal, alloy or compound and a wide range of substrate materials, from polymers to metals and ceramics. Hence, the PVD process is extremely versatile and superior to any other deposition method [84, 85].

PVD processes are classified in two general categories: evaporation and sputtering. In the evaporation process the material is vaporized in high vacuum from an evaporation source by resistance or inductive heating, electron beam, lasers or arc spots. Depending on the evaporation method, a range of energy and ionization states of evaporated species is obtained [86, 87]. The sputtering process is based on the ejection of the deposition material from a source, i.e. by energetic particle bombardment. All coatings in this thesis were deposited by the sputtering process; therefore it is described in more detail in chapter 4.3.

4.2 Plasma

4.2.1 Fundamentals and Characteristic Parameters

A plasma -considered as the fourth state of matter- is defined as a quasi-neutral gas of charged and neutral particles characterized by a collective behaviour. Plasmas are in average electrically neutral but exhibit a high number of charged species, therefore they are called quasi-neutral [88].

In a plasma, the motion of charged species causes local concentrations of positive and negative electric charges. These charge concentrations create long-range Coulomb fields

that interact and affect the motion of particles at a distance from the charge concentration. Therefore, elements of the plasma affect each other, even at large distances, leading to the characteristic collective behaviour of a plasma [88]. An electron has a much higher velocity than a charged atom. Consequently, if there is an electrical field in a plasma, electrons move quickly in response to negate the field. The response of charged particle to reduce the effect of local electrical fields is called Debye shielding and the distance of which the charge would be neutralized is described by the Debye length λ_D [88, 89]:

$$\lambda_D = \sqrt{\frac{\varepsilon_0 \cdot k_B \cdot T_e}{n_e \cdot e^2}}\,, \qquad (4.1)$$

where ε_0 is the vacuum permittivity, k_B is the Boltzmann constant, e is the electron charge and n_e is the electron density. The electron temperature T_e represents the mean translational energy of electrons in a plasma [88]. In a first approximation the kinetic energies of electrons and ions have Maxwellian distributions. Due to the different kinetic energies of the plasma species, a plasma can have several temperatures at the same time. At low pressures an applied power preferentially heats the mobile electrons, whereas heavy ions effectively exchange energy by collisions with the background gas. Hence, the Maxwellian distribution of electrons is much different from the ion distribution and $T_e >> T_{ion}$ (the ion temperature). As the electron temperature is much higher than the temperature of ions, or the gas, the plasma is not in a thermodynamic equilibrium, and the overall species distribution is best described by T_e. Electrons have a very low heat capacity and the heat transfer of electrons to neutrals, ionized particles, or the surrounding walls of the vacuum facility is small. Therefore, these non-thermodynamic equilibrium plasmas, as they are typical for PVD processes, are also termed *cold plasmas*. In our case the plasma is excited and sustained by direct current (DC) voltage applied between two electrodes, the target and the substrate. After a gas-species-specific threshold-ionization-potential is surpassed, a glow discharge plasma is ignited. Thus, the known discharge-voltage current characteristic is formed with the regions of Townsend-, normal-, abnormal-, and arc discharge. Sputtering takes place in the abnormal discharge field [88-90].

The plasma, i.e. partially ionized gas, is composed of respective densities of electrons (n_e), ions (n_i), and neutral gas atoms (n_0) and due to the averaged neutrality $n_e = n_i$. The

parameter, that describes the density of the charged particles in a plasma is the degree of ionization f_i and defined as [88, 89]:

$$f_i = \frac{n_i, n_e}{n_i, n_e + n_0} .$$

(4.2)

In glow discharges of thin film processes typical values for f_i are ~10^{-4}. With a PVD typical gas density n_0 of 10^{14} cm^{-3}, ion and electron densities are usually $n_e = n_i \sim 10^{10}$ cm^{-3}. However, high density plasmas like in a magnetic field near a magnetron can reach f_i of ~10^{-2} or higher [88-90].

When an electrically isolated substrate is inserted into a plasma it will be struck by electrons and neutrals with their respective charge fluxes J_e and J_i. Due to their different velocities J_e is much higher than J_i resulting in a negative charging of the substrate. As the substrate charges negatively, ions are attracted and electrons are repelled, until a state of equilibrium is reached. The resulting potentials of the isolated substrate and within the plasma are termed floating potential V_f and plasma potential V_p. The plasma potential is usually more negative by several volts than the floating potential. Practically, for isolated substrates this means that the ions are attracted to the substrate by the potential difference of V_p-V_f and hence the ion energy E_i impinging on the substrate is $E_i = e\left|V_p - V_f\right|$. Only those electrons with enough initial kinetic energy can hit the substrate [81, 88-91].

The above described parameters and details of plasma are of course only brief examples which allow a better understanding of the plasma characterization and the magnetron sputter process detailed in the following.

4.2.2 Plasma Characterization

Langmuir and co-workers were the first to study phenomena in a plasma in the early 1920's, and it is said that it was Langmuir who in 1929 used the term "plasma" for the first time [92, 93]. Therefore a method to determine important parameters of a cold plasma like n_i, T_e, V_p, and V_f, and λ_D is named Langmuir measurement. Except from the Langmuir probe itself, which is placed into the plasma, the arrangement needs careful shielding and insulation against additional charging. In order to fulfil correct measurements a probe has to comply several specifications [88, 94, 95] :

- the plasma region has to be significantly larger than one Debye length to sustain the quasi-neutrality.
- the ion to electron temperature ratio has to be close to zero meaning that the ions are at room temperature and single ionized.
- the ion and electron mean free paths should be greater than the probe radius or the Debye length to ensure the probe-plasma situation is collisionless.
- the probe surface has to be much larger than the Debye length but very small compared to the plasma region to minimize the plasma disturbance.
- the insolating material of the probe has to be chemically inert and should have a small sputtering yield. Usually refractory metal wires are utilized.

The set-up of a cylindrical Langmuir tungsten wire probe as used in this thesis is shown in Fig. 4.1.
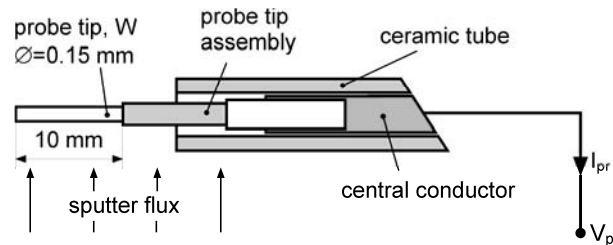

Fig. 4.1.Schematic of the Langmuir wire probe assembly used in this work [96].

Generally, in a Langmuir measurement, a probe voltage V_{Pr} is applied relative to the ground, and the responding probe current I_{Pr} measured. As I_{Pr} is the sum of the ion and electron current, $I_{Pr}=I_{ion}+I_e$, the Langmuir current-voltage trace has a characteristic non symmetrical shape, as shown in Fig. 4.2, comprised of three distinct regions. At a negative probe potential as compared to V_f, less electrons reach the target and mainly positively charged ions are collected. Consequently this section in the I-V trace is called *positive ion current region*. At a positively biased probe, as compared to V_p, only the flux of negatively charged particles, i.e. electrons is collected and current saturation occurs. This area is called *electron saturation region*. When V_p is less negative than the applied potential, $V_p > V_{pr}$, the probe collects only electrons with energies large enough to overcome the potential barrier. Thus, in this transition region, the probe current is the sum of electron and ion saturation current, $I_{pr}=I_e+I_{is}$. From this region T_e can be determined as here I_e is proportional to

$$I_e \propto e^{-e\left(\frac{V_{pr}}{k_B \cdot T_e}\right)}. \tag{4.3}$$

With $I_e = I_{pr} - I_{is}$, T_e is calculated from the slope of the linear region of an $\ln(I_e)$ vs. V_{pr} plot [88, 94, 95], see insert in Fig. 4.2. When T_e is determined, the ion flux density (J_i) and consequently the ion density n_i can be calculated by [97, 98]:

$$J_i = \frac{I_{is}}{e \cdot A_s} \quad \text{and} \quad J_i = n_i \sqrt{\frac{k_B \cdot T_e}{2\pi \cdot m_i}}, \tag{4.4}$$

where A_s is the surface of the cylindrical Langmuir probe ($A_s = 4.7$ mm^2) and m_i is the absolute ion mass. The plasma potential V_p can be obtained from a semi-logarithmic plot of $\ln(I_{pr})$ vs. V_{pr} and is the intercept of the extrapolated linear region of the curve at low probe current with the tangent to the plot in the electron saturation region [97, 98], see insert in Fig. 4.2.
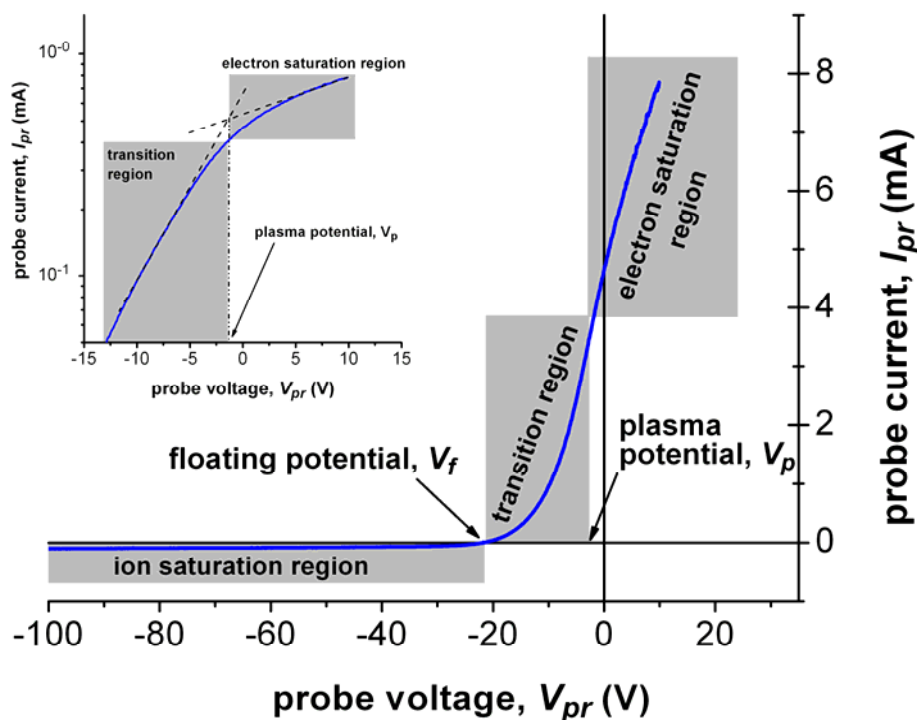

Fig. 4.2. Current-voltage trace measured with a Hiden ESP Langmuir probe used during pulsed DC sputtering of a Ti$_{0.49}$Al$_{0.49}$Y$_{0.02}$ target with 80 kHz and $t_{rev} = 4976$ ns in an 0.5 Pa N$_2$/Ar discharge.

In this thesis Langmuir plasma analyses were done on DC magnetron and pulsed DC magnetron discharges during sputtering from a Ti$_{0.49}$Al$_{0.49}$Y$_{0.02}$ target using a standard

Hiden ESP system. As presented in Fig. 4.3 and discussed in full detail in publication V [74], changes in the target voltage wave form in dependence of the reverse pulse length t_{rev} (further detailed in chapter 4.3.2), have a strong influence on the plasma parameters.

The plasma potential V_p (Fig. 4.3a) decreases with increasing positive pulse length from -7.2 V for the DC discharge to smaller negative values with increasing t_{rev}. V_p of a pulsed magnetron discharge with 250 kHz and t_{rev} = 1616 ns is +1.38 V. Consequently, the energy of the impinging ions E_i on the substrate or growing film at an applied bias potential V_B of -50 V also increases according to $E_i = e|V_B - V_P|$ from 42.8 to 51.38 eV when changing from DC discharge to 250 kHz pulsed DC with t_{rev} = 1616 ns [99-101]. The electron temperature T_e (Fig. 4.3b) increases with increasing reverse voltage time t_{rev} and reaches a maximum T_e of ~5 eV independent of the used frequencies.
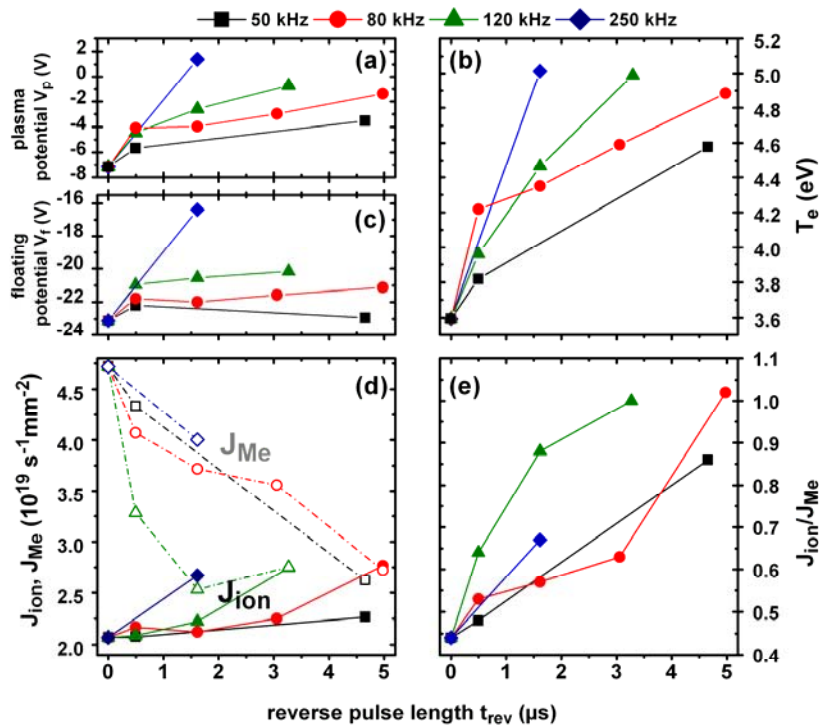

Fig. 4.3. Plasma potential V_p (a), electron temperature T_e (b), floating potential V_f (c), ion and metal flux J_{ion}, J_{Me} (d), and ion to metal ratio J_{ion}/J_{Me} (e) of DC magnetron sputtering (0 μs) and pulsed DC magnetron sputtering with 80 kHz and increasing t_{rev}.

Although the Langmuir data presented inhere are not time resolved and thus give time averaged values, the general trends observed are fully in-line with literature. Electron heating through discharge pulsing is discussed in Refs. [102-105] and occurs through stochastic heating caused by MHz ringing of the target voltage, as will be shown later in chapter 4.3.2. The increases in T_e and electron density lead to increases in V_f (Fig. 4.3a)

and ion fluxes (Fig. 4.3d). All investigated frequencies yield J_i increases with increasing reverse voltage time t_{rev} as presented in Fig. 4.3c.

Furthermore, from the pulsing induced reduction of sputter-on duty time with increasing t_{rev} the sputter rate decreases (as outlined in chapter 4.3.2). Hence, the metal flux J_{Me} arriving on the substrate during pulsed DC magnetron sputtering (DC-MS) decreases with increasing t_{rev} and thus the decreasing sputter rates can be accounted for by the shorter magnetron power on time. Consequently, as J_i increases and J_{Me} decreases with increasing t_{rev}, the ion-to-metal flux ratio J_i/J_{Me} increases with t_{rev}. In the case of a pulsing frequency of 80 kHz, J_i/J_{Me} increases from ~0.44 to 1.02 for increases in t_{rev} from 0 (DC-MS) to 4976 ns, respectively.

4.3 Magnetron Sputtering

4.3.1 DC Magnetron Sputtering

A sputtering process is characterized by a momentum transfer between atoms and the interaction of energetic particles with solid matter. A fast particle, usually from an inert gas e.g. an Ar ion, ejects an atom from a surface zone of a defined material called target [91]. In general a sputter system is composed of a cathode (target) and an anode (substrate), which are facing each other at certain distance in a vacuum chamber, indicated in Fig. 4.4. As discussed in the previous chapter, the inert gas ions are created in a glow discharge plasma and accelerated to the target. The latter consists of the material to be sputtered, and is well bonded to a water cooled copper backing plate to dissipate the heat created during ion bombardment. The number of sputtered atoms per incident particle is termed sputter yield S. A cosine law distribution of sputtered species is generally observed [83]. Both, the sputter yield and the angular distribution of sputtered atoms depend on the ion energy of incident particles, sputtered species, texture and grain size of the target [83, 106] and can be estimated as described in Chapter 5.3.2.

In a basic planar diode sputtering system high operating pressures have to be applied to allow enough ionizing collisions between target ejected secondary electrons and the working gas. When a magnetic field of a few Gauss is applied on the target, low enough to affect only electrons not ions, the electrons are concentrated near the target, which allows for lower applied sputter voltages. Instead of minimizing their loss of energy at walls, the

electrons collide predominantly with gas atoms, leading to high ionization efficiency. The increased ion density results in lower necessary gas pressures and thus higher deposition rates [83, 106].
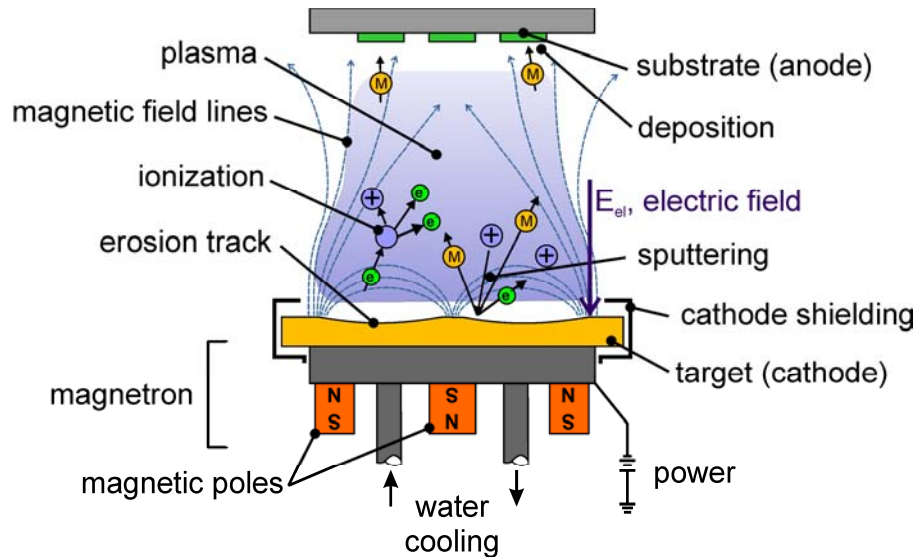

Fig. 4.4. A typical setup for unbalance magnetron sputter deposition (modified from [96, 106, 107]).

The systems using crossed electric and magnetic fields are termed magnetrons and are in practical sputter applications cylindrical, circular or planar. The latter one is used in this thesis as indicated in Fig. 4.4. The draw-back of this system is the non uniform target erosion trace due to the electron confinement, leading to the so-called sputter-, or erosion track.

For general applications two different magnetron systems are used; the conventional balanced magnetron (CBM) and the unbalanced magnetron system (UBM). In an UBM system as utilized in this thesis, outer and inner magnets have different strength. Therefore, in contrast to the CBM, only a part of the magnetic field is kept in the vicinity of the target, whereas other magnetic lines reach a wide range to the substrate. Hence, the plasma is not only confined near the target, but can also expand towards the substrate. This allows substrate heating through energetic particle bombardment, is improving diffusion and results in modified coating growth. The energy of the ion flux can be adjusted by varying the magnetic field or by applying a bias potential to the substrate [83, 100, 106]. In general the magnetic field mainly influences the ion density whereas the bias affects the ion energy.

In the case of the $(Ti_{1-x}Al_x)_{1-y}Y_yN$ films, the reactive magnetron sputtering method was used, where one film component, here nitrogen, is introduced into the deposition chamber in the gaseous state. The nitride component forms generally on the growing film. In the here utilized deposition setup the N_2/Ar partial pressure ratio was 0.4 at a total gas pressure of 0.5 Pa and a power density of 9 W/cm^2. Base pressure in this system was below 0.1 mPa and a bias voltage of -50 V was applied.

The Al-Au coatings were produced by non-reactive sputtering in an Ar glow discharge at a working gas pressure of 0.6 Pa and a magnetron power density of 2.7 W/cm^2. The substrates were -85 V biased. Base pressure in the system was 0.2 mPa.

4.3.2 Pulsed DC Magnetron Sputtering

In the mid-1990s pulsed DC magnetron sputtering was introduced to allow the deposition from dielectric targets and to circumvent target poisoning and subsequent target arcing during reactive magnetron sputtering [108, 109]. As presented in Fig. 4.5, during pulsed DC sputtering the polarity of the DC power, i.e. potential, at the target is alternated between negative and positive. During the negative pulse, t_{on}, normal sputtering takes place and ions are attracted to the target to eject atoms. When the positive reverse pulse, t_{rev}, is applied electrons from the plasma are attracted to the target. These electrons discharge positive charged poisoning layers and lead to a higher potential gap between plasma and target, yielding higher energies for the subsequently impinging ions, which further help eliminating a residual poisoning layer at the target [108, 110, 111]. When either magnitude and duration of t_{on} are greater than of t_{rev}, or the potentials of positive pulse and negative phase are different, as it was the case in this thesis, the method is called asymmetric pulsed DC sputtering (pulsed DC-MS).
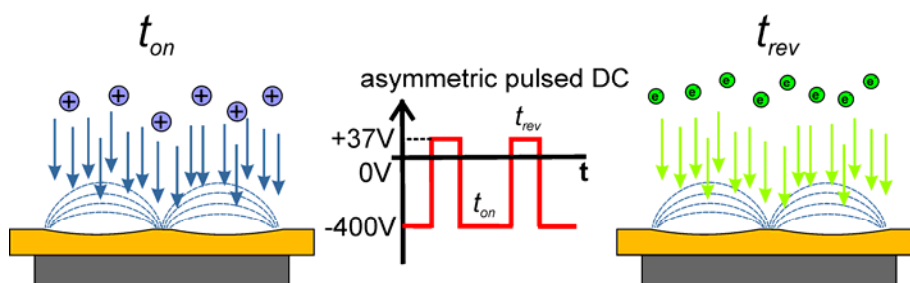

Fig. 4.5. Schematic of asymmetric pulsed sputtering. During the negative pulse, t_{on}, ions are attracted and during the positive pulse, t_{rev}, electrons are attracted to the target (modified from [108]).

Today, in conventional pulsed DC sputtering applications, pulse frequencies vary between 20-350 kHz. In most power supply units also t_{rev} can be adjusted to allow a modification of the pulse duty cycle which itself is the ratio between sputter on-time t_{on} and the overall period (t_{on}+t_{rev}).

Though, pulsed DC-MS has become a common tool for the application of dielectric materials, only few reports exist on the modification of microstructure, mechanical and physical properties of hard nitride coatings by this method [109, 112-115].
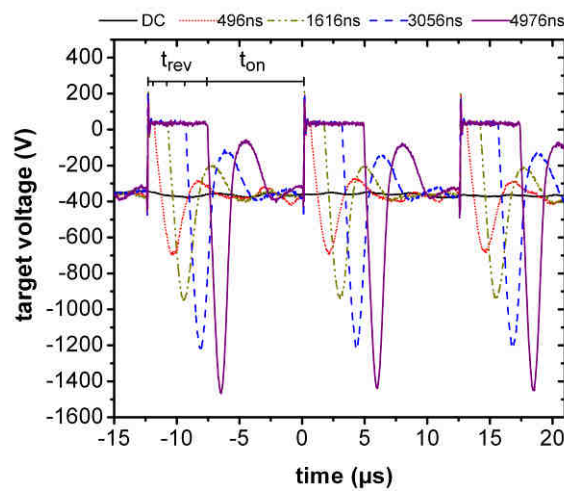

Fig. 4.6. Target voltage waveforms for DC magnetron sputtering and pulsed DC magnetron sputtering with 80 kHz and t_{rev} = 496 ns (dotted), 1616 ns (dash dotted), 3056 ns (dashed), and 4976 ns (solid) – Publication V [74].

Therefore, in this thesis the effect of asymmetric bipolar pulsing on the microstructure of $(Ti_{1-x}Al_x)_{1-y}Y_yN$ is investigated using an ENI RPG-50 generator, set to provide 400 W in power regulation mode (publication V, [74]). In consequence a chemical composition is chosen which is close to the metastable solubility limit as there the material is extremely sensitive to changes in the sputtering conditions. The pulsing frequency f of a +37 V reverse voltage pulse was varied between 50 and 250 kHz with a positive pulse length t_{rev} variation from 496 ns to a maximum of 8016 ns. Typical target voltage waveforms, as they are recorded during sputtering with 80 kHz and t_{rev} = 496, 1616, 3056, and 4979 ns, are presented in Fig. 4.6. The waveform strongly differs from the idealized voltage vs. time trace shown in Fig. 4.5, which is attributed to the nature of the power supply [74, 102-104, 116-118]. At voltage reversal high overshoots occur in the onset of t_{on} and t_{rev}. The observed fast fluctuation (MHz frequency) of target voltage above +200 V at the onset of t_{rev} is reported to be accompanied by strong increases in the target current [103, 104, 116,

117]. After this MHz ringing the reverse voltage flattens to +37 V during t_{rev}. On polarity alternation the target voltage overshoots the -350 V observed during DC mode for the 400 power regulation and the used $Ti_{0.49}Al_{0.49}Y_{0.02}$ compound target. Thereby the target peak voltage reaches -700 V for $t_{rev} = 496$ ns and increases to -1450 V for increasing t_{rev} to 4976 ns at the onset of t_{on} and levels off to about -350 V (Fig. 4.6). The high peak target voltages along with the MHz variation in the positive pulse region have strong impact on plasma parameters (see chapter 4.2.2) and consequently the microstructure and properties of the grown coating, as described in publication V [74].

One disadvantage of the pulsed magnetron sputtering of nitride coatings is a decreased deposition rate due to the pulsing induced reduction of deposition time, t_{on}. Here the sputter rate decreases from 44 nm/min for the DC-magnetron sputtered coating to 38, 37, 33, and 28 nm/min for 80 kHz pulsed DC-MS films deposited with deposited with $t_{rev} = 496$, 1616, 3056, and 4979 ns [74].

5 Thin Film Microstructure and Composition

5.1 Characterization

The understanding of structures and their origin strongly depends on the analyzing techniques and methods. Therefore, the three most prominent methods for structural characterisation used in this thesis are presented in the following.

5.1.1 X-ray Diffraction

X-ray diffraction (XRD) is a powerful, non-destructive method which allows the determination of structure, phase composition, texture, lattice constants and stresses of unknown crystalline materials by comparing the measured diffractogram to known standards [119-121]. In this thesis the X-ray diffractograms were recorded in Bragg-Brentano geometry, where only the diffraction from crystallographic planes with the plane normal parallel to the diffraction vector are investigated in accordance to Braggs' law [122]:

$$n \cdot \lambda = 2 \cdot d \cdot \sin \theta, \tag{5.1}$$

where constructive interference is observed when the path difference of travelling X-rays is an integral number n of the X-ray wavelength λ. The path difference is defined by the geometrical relation $2 \cdot d \cdot \sin \theta$, where θ is the angle of incoming X-rays and d (or d_{hkl}) is the lattice plane spacing which can be derived from the Miller indices (hkl) and the dimensions of the unit cell. Further information on methods and techniques of X-ray diffraction are presented in Refs. [119-121, 123].

By fitting a diffraction peak with a Pseudo-Voigt function, which is a linear combination of a Cauchy and a Gaussian function, domain sizes -i.e. crystallite sizes- and the lattice strain can be calculated. The domain size is a function of the Cauchy part of the Pseudo-Voigt function and corresponds to the average length of crystalline domains in the direction of the diffraction vector [124].

A typical X-ray diffraction analysis is presented in Fig. 3.4 where the phase distribution in dependence of the Y content is shown. From the peak positions of the single-phase cubic $Ti_{0.45}Al_{0.55}N$ film the lattice parameter a_c of the cubic structure of 4.178 Å was determined according to the Cohen-Wagner method [125]. A 25 nm crystallite size was calculated for

this coating employing the Pseudo-Voigt method. This domain size corresponds well to the ~22 nm column width measured in cross-section TEM analyses. Diffraction angle positions of the hexagonal phase are used to derive the lattice parameters a_w and c_w for hexagonal wurtzite $(Ti_{1-x}Al_x)_{1-y}Y_yN$, yielding $a_w = 3.075$ and $c_w = 5.295$ Å for y = 2 at.%, $a_w = 3.185$ and $c_w = 5.215$ Å for y = 5 at.%, and $a_w = 3.205$ and $c_w = 5.220$ Å for y = 9 at.%. The lattice parameters of the cubic phases in the films vary only within the error of measurement between $a_c = 4.178$ and 4.181 Å. These results are in good agreement with lattice parameters calculated by ab-initio and show the broad range of data which can be derived by the relatively simple X-ray diffraction technique. A deeper discussion of the above data is provided in publication IV [73].

5.1.2 Scanning Electron Microscopy

Scanning electron microscopy (SEM) is a standard method for the investigation of structures with sizes raging from tenth of nanometres to the cm scale. The SEM focuses a high energetic electron beam on the surface of a sample and detects and analyses the signals created by the interaction of the electron beam with the surface. These signals include secondary electrons, back scattered electrons and characteristic X-rays [83, 126].

The most common imaging mode monitors low energy secondary electrons. The brightness of the signal depends of the number of electrons reaching the detector. Therefore, steep surfaces and edges tend to be brighter than flat surfaces, leading to the characteristic three-dimensional image appearance.

Backscattered electrons are used to detect contrasts between different chemical compositions -i.e. areas with different average atomic number- as the signal brightness of backscattered electrons increases with the atomic number.

The elemental composition of a sample can be determined in a SEM by analysing the characteristic X-rays emitted by electron interaction with the sample. The method used in this thesis was energy-dispersive X-ray spectroscopy (EDX).

A typical example for a SEM investigation is presented in Fig. 5.1, of an Al_2Au coating isothermally oxidized for one month (672 hours) at 800 °C. Fig. 5.1a shows a secondary-electron cross-section image of the rough and porous oxide scale. A clear elemental contrast is visible in the back-scattered electron image of Fig. 5.1b and reveals the large diffusion zone of coating material into the γ-TiAl substrate. Together with the EDX line

scan in Fig. 5.1c the diffusion layers and oxide scale can be interpreted as follows: at the surface an oxide scale has formed composed primarily of Al_2O_3 with traces of TiO_2 from Ti diffusion from the substrate. Below there are two Au rich layers, of Al, Ti and Au. Underneath these layers a >30 µm diffusion zone of Au into the γ-TiAl substrate has formed [24]. Mores SEM analyses on as-deposited and oxidized material is presented in publication VI [127].
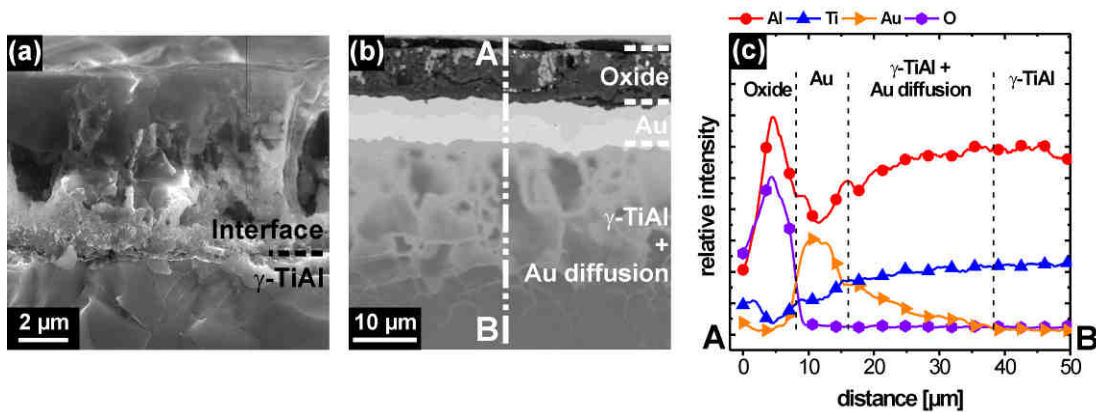

Fig. 5.1. (a) Secondary electron image, (b) back-scattered electron image, and (c) EDX line-scan of an Al_2Au coating on γ-TiAl oxidized for 672h at 800 °C (Publication VI [127]).

5.1.3 Transmission Electron Microscopy

Transmission electron microscopy (TEM) allows obtaining volume information of a thin specimen by the transmission of a high energetic electron beam. Similar to the SEM also in TEM signals from the electron-sample interaction can be taken for a wide band of analytical and imaging techniques. Combined with the high imaging resolution of less then 1 Å modern TEM systems (accordingly termed high-resolution TEM or HRTEM) are powerful tools for material analyses down to the atomic level.

The basic operation of a TEM can be divided into the recording of diffraction pattern or images, as shown in Fig. 5.2a and b, respectively, and depends on the strength of the intermediate lens. A diffraction pattern gets projected to the screen when the back focal plane of the objective lens is the object plane of the intermediate lens, whereas for projecting an image, the image plane has to coincide with the object plane of the intermediate lens.

Placing apertures in the back-focal plane of the objective lens allows imaging through the selection of electrons scattered in a specific direction. By utilizing only the primary beam

so-called bright-field (BF) images are recorded (Fig. 5.2c). Regions of the specimen that are thicker or more dense will scatter electrons more strongly and will appear darker in the image. This technique is also sensitive to lattice defects, such as staple faults, point defects or dislocations as the distortion of crystalline planes causes intensity variations in the image. Utilizing only the scattered electrons for imaging a so-called dark field (DF) image is generated (Fig. 5.2d). The above only presents a very brief overview on TEM techniques used in this thesis. Further and more detailed information on transmission electron microscopy is discussed in literature like Refs. [128-132].
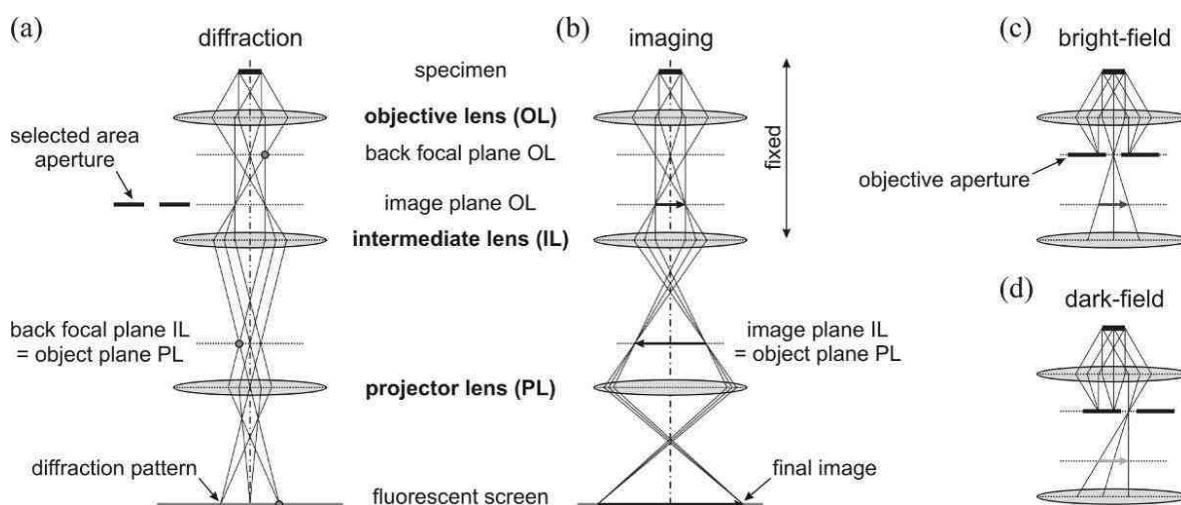

Fig. 5.2. Beam path for recording of (a) diffraction pattern and (b) images. The primary beam is used for bright-field (c) the scattered beam for dark-field (d) imaging. (from [54]).

Typical TEM images as taken and analysed in this thesis are discussed in chapter 5.2 and presented in Fig. 5.6 and Fig. 5.7 or are presented in publications I and V.

5.2 Structural Evolution during Film Growth

In PVD technology, the to-evaporate material determines the necessary deposition technique. The deposition parameters, however, influence nucleation and growth of particles condensing from the vapour phase, which, on their part, determine the coating microstructure and consequently the physical and mechanical properties of the deposited film.

Depending on the arrival rate, energy and substrate condition, impinging particles on the substrate can adsorb, desorb (re-evaporate), diffuse on the substrate surface and/or settle at low energy lattice sites. At high enough particle impinging rates, metastable and ultimately

stable clusters form through atom diffusion or direct capture of particles from the vapour phase. Large clusters may also grow at the expanse of smaller ones through Ostwald ripening [133]. Upon further growth of nuclei and clusters, they connect and coalescence leads to a continuous network of clusters, which ultimately results in full substrate coverage [83, 96, 133-135].

Formation of a critical cluster size which can act as nuclei requires the adsorption of several species from the vapour phase and surface diffusion as presented in Fig. 5.3. Subsequently, the combination of such nuclei and the formation of a three-dimensional coating, is called film growth [136]. The general steps of nucleation and growth are
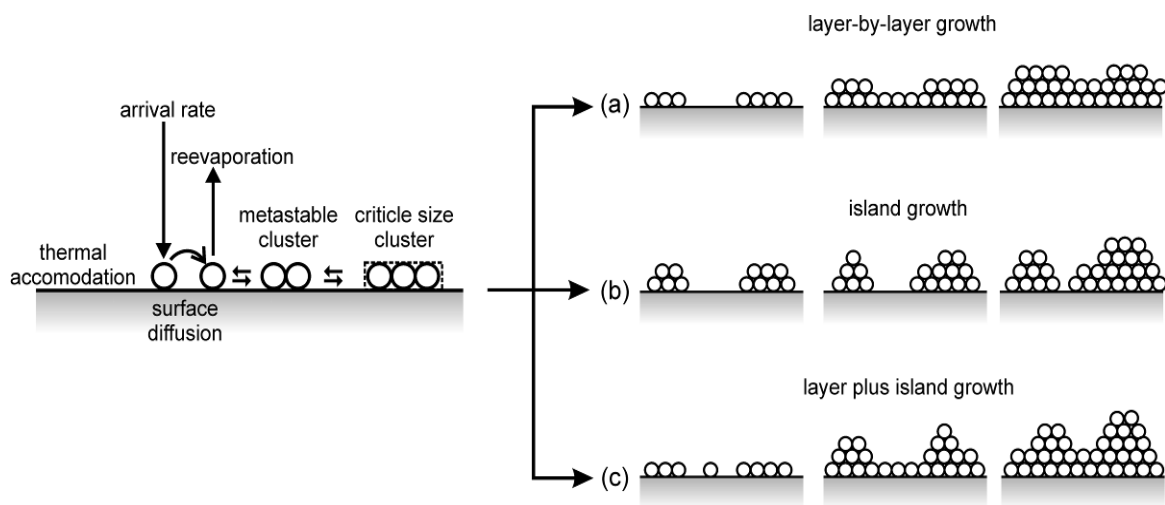

Fig. 5.3. Nucleation and schematic representation of the three standard growth models (a) layer-by-layer growth, (b) island growth, and (c) layer plus island growth (modified from [83, 96]).

schematically shown in Fig. 5.3(a) for layer-by-layer growth, Fig. 5.3(b) for island growth, and Fig. 5.3(c) for layer plus island growth. The differences are explained in more detailed in the next paragraph.

The shape of initially formed clusters depends on the surface energies of the free substrate surface, the film/substrate interface and the film surface to the vapour, and results ultimately in the film growth according to three basic models [83, 134, 135], as presented in Fig. 5.3(a), (b), and (c):

   (a) *Layer-by-layer growth* (Frank van der Merwe mode): Atoms are at least equally strong bonded to the substrate than to each other. Therefore the extension of the nuclei occurs in two dimensions resulting in the formation of planar layers.

(b) *Island growth* (Volmer-Weber mode): Atoms or molecules are more strongly bounded to each other than to the substrate, and subsequently grow in three dimensions to form islands.

(c) *Layer plus island growth* (Stranski-Krastanov mode): This is a combination of the preceding two modes. After the formation of one or two monolayers, subsequent layer growth becomes unfavourable and islands form.

Further, film growth is characterized by several basic processes such as shadowing, desorption, surface diffusion, and bulk diffusion. Shadowing is a result of the surface roughness of the substrate and the angle of impingement of the arriving atoms. The activation energies of surface and bulk diffusion are related and proportional to the melting point of the condensate (T_M). In dependence of the substrate temperature (T_s) one or more of these processes dominate the coating growth and lead to a distinct coating morphology. Therefore, the ratio between T_M and T_s, the homologous temperature (T_S/T_M), is the basis of structure-zone models (SZM), which correlate the observed microstructure with the predominant processes and deposition parameters.

The first who introduced a basic SZM were Movchan and Demchishin who identified three different zones but only considered T_S/T_M as variable [139]. Thornton added the gas pressure as second variable and noted an additional zone between 1 and 2, the transition zone T [137]. The SZM according to Thornton is given in Fig. 5.4a.
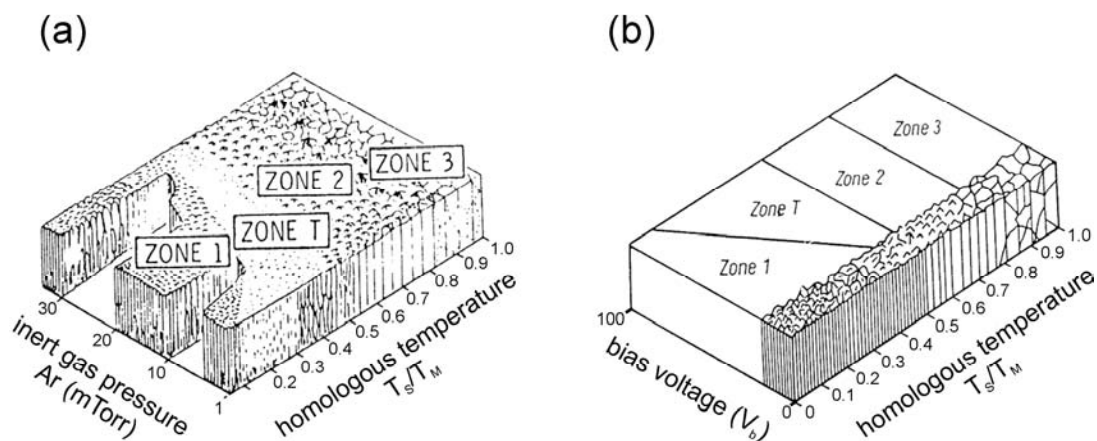

Fig. 5.4. (a) Structure zone model (SZM) after Thornton [137], (b) modified SZM for ion assisted PVD after Messier [138].

Within the last decades many authors further developed SZMs for various structure influencing factors and contributed to an in-depth understanding of the structure develop-

ment underlying processes. Practically all of them use the terminology introduced by Movchan and Demchishin (zone 1 to 3) and Thornton (zone T) [99, 133, 138, 140-147].

Generally, there is no sharp boundary line between the different structure zones but rather a smooth transition. Overall the zones differ from each other by their predominant form of diffusion [106, 140]:

In *zone 1* the homologous temperature is low and surface diffusion in negligible. It is known as ballistic zone deposition as the only motion of atoms which affects the deposition is the direction of the arriving vapour. Thus crystal planes of high condensation probability grow preferentially. Shadowing effects lead to a microstructure of amorphous or defect-rich crystalline columns separated by voids. The coating surface is very rough consisting of voids and cones.

When T_S/T_M is increased also the self-surface diffusion of ad-atoms increases but grain boundary migration is still limited. The result is a transition *zone T* microstructure of dense-packed and fibrous columns but still a high defect density. The structure develops by competitive growth of differently oriented crystals and is inhomogeneous along the thickness featuring fine V-shaped grains at the interface and thick columns at the film surface.

Surface and interface diffusion has become the significant factor in *zone 2* resulting in a straight and homogenous columnar structure with a preferred orientation perpendicular to the plane of lowest surface energy. The columns are less defected and often feature a facetted surface.

In *zone 3* the high homologues temperature allows bulk diffusion and grain boundary movement. The structure consists therefore of wide isotropic or equiaxed columns, or globular grains and a smooth and bright surface.

As shown by Thornton (Fig. 5.4a), increasing gas pressure shifts the structure zones 1 and T to higher homologous temperatures. Increasing gas scattering of the sputtered species and the absorbed Ar limit the surface diffusion, which consequently needs higher energies, i.e. T_S/T_M, to be activated. Temperatures in zone 2 and 3 are high enough to still allow diffusion. Therefore, there is only a minor effect of increasing Ar pressure on these two structure zones [137].

Messier et. al. separated the effects of thermal- and bombardment-induced mobility of ad-atoms by the investigation of structure development with increasing bias voltage (Fig. 5.4b). At low ion bombardment (low V_b) zone T is small or even not existing. Surface mobility increases with ion bombardment, which supports the nucleation stage of film growth leading to a broadening of zone T in expense of zone 1 with increasing V_b. As temperature induced surface and bulk diffusion is the governing factor in zone 2 and 3, these microstructures are not affected by the increased bias voltage [138].

Structure zone models for novel multi-component coatings can strongly differ from the above presented SZMs. Small amount of alloys, dopant components or impurities lead to recurrent nucleating and with high alloy concentrations a second phase may form. The dependence of continuous renucleation on the homologous temperature is investigated by Grovenor et. al. [147] and presented in Fig. 5.5. Zone 1, which is featuring a very fine grained and equiaxed microstructure is widened to higher temperatures on the expense of zone T and zone 2. In zone T renucleation leads to the formation of columns composed of several stacked grains, whereas at higher temperatures at zone 2 and 3 high ad-atom mobility results in the formation of columnar grains.
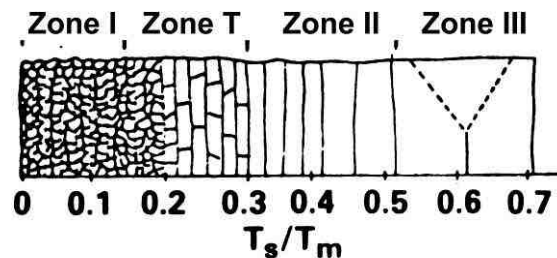

Fig. 5.5. Modified SZM after Grovenor, showing the effect of continuous renucleation on film structure [147].

Starting from the ideal SZM, Barna and Adamik investigated the influence of increasing amount of impurities on the coating structure [140, 148]. At low levels of impurity the grain growth at coalescence is not limited however decreased mobility at contaminated surfaces reduces further grain growth, resulting in smaller column widths than according to the ideal SZM. At medium impurity levels a competitive structure according to zone T develops, as grain growth is already limited at the coalescence stage resulting in randomly oriented first crystals. At high levels of alloy or impurity concentration crystal growth is periodically blocked by the formation of a crystal surface covering impurity layer. The film

is composed of three-dimensional equiaxed globular grains with random orientation according to zone 3. Thus, at high impurity levels zone 1 can even boarder zone 3 [148].

Depending on the coating, composition and deposition method used, the films grow with a wide range of morphologies and structures.

In the case of the Al-Au coatings the film with Al/Au ratio of 1.85 has a ternary phase structure composed of metastable Au, AlAu, and Al_2Au. With an Al/Au ratio of 2.0 the coating grows (311) textured single phase Al_2Au and the film with an Al/Au ratio of 4.32 is composed of Al and Al_2Au. Cross-sectional TEM analyses, as shown in Fig. 5.6, reveal a coarse grained, porous (bright areas) structure of Al_2Au, with Au (darkest areas) and AlAu phases for the ternary Al/Au = 1.85 (Fig. 5.6a), and a dense, columnar micro-structure for the single-phase Al_2Au coating (Fig. 5.6b). The binary Al/Au = 4.32 film exhibits again a coarse grained but layered structure of Al_2Au with nanosegregation of Al and metallic Al phases (bright areas - Fig. 5.6c), as described in publication I [27].
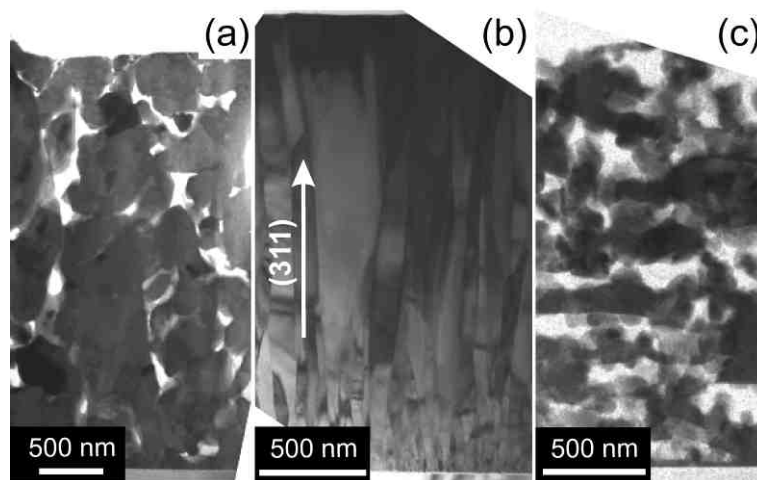

Fig. 5.6. Bright-field TEM cross sections of as-deposited Al-Au coatings with Al/Au at.% ratios of 1.85 (a), 2.00 (b), and 4.32 (c) (indicated in the binary phase diagram Fig. 3.1) – Publications I and II [27, 35].

From detailed TEM investigations and a critical literature study it was possible to suggest growth mechanisms for the individual coating compositions and morphologies described above. During crystallization of the single phase Al_2Au film, from a vapor with an Al/Au ratio of 2, this phase has the highest energy of formation among other neighboring intermetallic species which further promotes the growth of Al_2Au [149]. As Al_2Au phases are nucleating from the very beginning the nucleation density is high [150]. Thus, a high number of Al_2Au crystallites grow competitively in zone T morphology on a layer-by-layer basis or from Al_2Au tetrahedrons in vapor flux direction as described in Refs. [151, 152].

During growth of the film with an Al/Au ratio of 4.32 the Al_2Au phase nucleates first due to its highest energy of formation, hence, excess Al segregates to form Al domains, as no other intermetallic phase is on the Al-rich corner of the binary phase diagram (see Fig. 3.1). For Al-Au diffusion couples with Al/Au > 2, the formed phases are always Al_2Au and Al [149]. At different temperatures only the growth rates of the Al-Au phases formed are influenced [33]. The diffusionally governed phase separation allows the growth of larger Al_2Au domains as compared to the single-phase Al_2Au film. Based on the limited time for diffusion processes during the growth of the films, excess Al forms nano-segregations within the Al_2Au domains, as the growth rate is $\sim 1.6 \cdot 10^{-9}$ m/sec and the diffusion of Al on Al is around 10^{-15} m^2/sec at the deposition temperature of ~ 300 °C [153, 154].

During growth of coatings with an Al/Au ratio of 1.85 the Al_2Au and AlAu phases form according to their heat of formation of -126.8±6.3 kJ/mol and -77.0±4.2, respectively [149]. Additionally, metallic Au grows metastable due to the limited atomic assembly kinetics during low temperature deposition processes and transforms upon annealing to $AlAu_2$, see publications I and II [27, 35]. $AlAu_2$ is an intermediate product in the diffusion path to form the intermetallic phases Al_2Au or AlAu from Al-Au couples [31, 149]. Kirkendall voiding is reported for Al-Au thin film couples, the formation of voids in the films with Al/Au=1.85 is thus attributed to this process [7, 30].

More details on Al-Au coating morphologies, growth conditions and their impact on thermal stability are presented in publication I [27], publication II [35], and publication III [36].

The single phase cubic $Ti_{0.45}Al_{0.55}N$ coating grows with a dense columnar structure. The columns have evolved from competitive growth according to zone T. A primarily hexagonal wurtzite phased $Ti_{0.38}Al_{0.53}Y_{0.09}N$ film containing 9 at.% Y in the metallic sublattice has a very fine texture of featherlike, small-diameter grains elongated in the growth direction. This structure originates from continuous renucleation of cubic and hexagonal phases and is described in more detail in publication IV [73].

A new and more complex growth mechanism was found for the $(Ti_{1-x}Al_x)_{1-y}Y_yN$ films with y = 2 at.% Y. Close to the substrate the coating exhibits a dense columnar structure with a growth direction perpendicular to the substrate surface, according to zone T. At a certain distance from the interface the growth direction is tilted to the substrate normal. Selected area electron diffraction pattern (SAED) reveal a single phase cubic NaCl <200> textured

structure at the substrate near part and a mixture of <200> and <111> textured cubic and <002> textured hexagonal phases in the tilted region as indicated in Fig. 5.7b. Further, increasing reverse voltage lengths, t_{rev}, during asymmetric bi-polar sputtering lead to increasing thicknesses of the single phase cubic <200> textured interface-near layer.
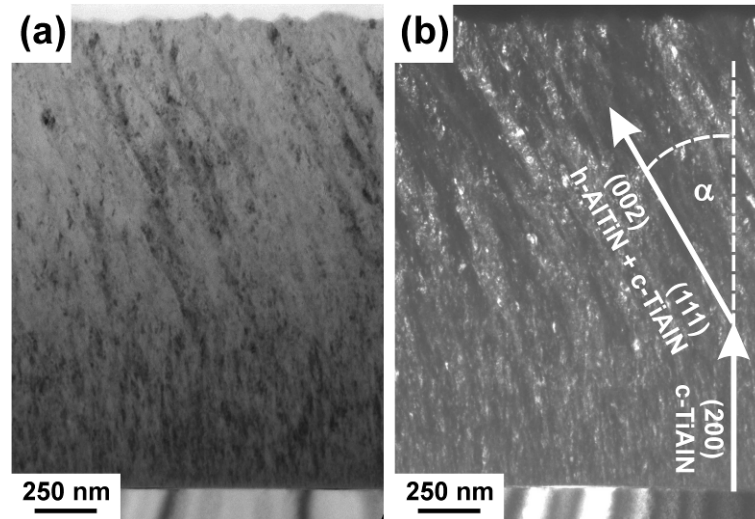

Fig. 5.7. (a) Bright-field and (b) dark-field TEM cross sections of $Ti_{0.49}Al_{0.49}Y_{0.02}N$ produced by 80 kHz pulsed DC magnetron sputtering with t_{rev} = 496 ns. The two growths zones are indicated in (b).

For this structure a growth mechanism based on energetic and crystallographic considerations is suggested as follows:

Texture formation in magnetron sputtered TiN based films is governed by the need for minimization of the surface energy and the accumulated strain energy [155], where at small thicknesses the surface energy is the dominating factor and at larger thicknesses the accumulated strain-energy, which increases linearly with the thickness [156, 157]. Thus, for TiN based coatings a <200> texture can be expected at small thicknesses, as the {200} planes have the lowest surface energies [158-161]. Refs. [162, 163] report for TiN an anisotropy of the elastic moduli E with $E_{200}<E_{220}<E_{111}$ and hence the accumulated strain energy U decreases from <200> to <220> to <111> textured films. Therefore, starting from a critical thickness during film growth a transition from <200> to <111> texture occurs. Furthermore, it is reported that within an epitaxial multilayer arrangement between cubic TiN and hexagonal AlN the cubic (111) TiN planes are tilted by ~20° from the hexagonal [001] AlN direction [164]. The crystallographic relation for an epitaxial matching between cubic TiN and hexagonal AlN lattices can be described as [164, 165]:

$$-\{111\}_{TiN} \langle 110 \rangle_{TiN} \| \{002\}_{AlN} \langle 110 \rangle_{AlN}.$$

This is the orientation dependence in the afore mentioned films between cubic and hexagonal phases. Therefore, it is proposed that the tilted columnar growth, which is only observed in the cubic-hexagonal binary phase region with <111> textured cubic phases, is the result of the hexagonal phase formation as presented in more detail in publication V [74].

Additionally, the hexagonal phase formation benefits from the higher mean diffusion length of Al on cubic (100) surfaces compared to (111), as it is shown for Ti on TiN, and the lower absorption energy of Al compared to that of Ti on TiN [37, 161, 166]. A possible explanation is that as soon as cubic (200) and (111) grains coexist, surface diffusion leads to a preferential cubic (111) growth and, combined with the above orientation dependence, to the nucleation and growth of (002) hexagonal crystals due to the faster Al diffusion compared to Ti.

The increases in thickness of the cubic <200> layer in expense of the tilted cubic and hexagonal structure can be explained by the J_i/J_{Me} increase with increasing reverse voltage lengths t_{rev} (see chapter 4.2.2), as high J_i/J_{Me} ratios lead to a preferred <200> growth [99, 101]. Further, the decreasing Al/Ti composition ratio results in the stabilization of the cubic structure below the metastable solubility limit [74, 99, 101].

A more detailed discussion on the structural evolution and growth mechanisms of the bipolar pulsed $(Ti_{1-x}Al_x)_{1-y}Y_yN$ coatings is presented in publication V [74].

5.3 Modelling

Computational modelling gives rise to a better understanding of the underlying physics of material- or process behaviour and is therefore an excellent tool to underpin scientific investigations and to complement traditional theoretical and experimental approaches. The two methods used in this thesis are presented in the following.

5.3.1 Ab-initio Calculations

The term ab-initio describes that calculations are made from first principles and neither empirical data nor material parameter input is used for computation. Ab-inito calculations

performed for this thesis are based on the density-functional theory (DFT) which allows the investigation of the ground state of atoms, molecules and condensed phases. The advantage of the DFT method is that it uses the electron density as the basic quantity of calculation instead of solving the many-body electronic wave function i.e. Schrödinger-equation. It therefore makes the calculation of multi-electron systems possible at a reasonable computational effort [167, 168].

In this thesis the ground state and stability of PVD condensed phases was calculated using the Vienna Ab-initio Simulation Package (VASP) [169].
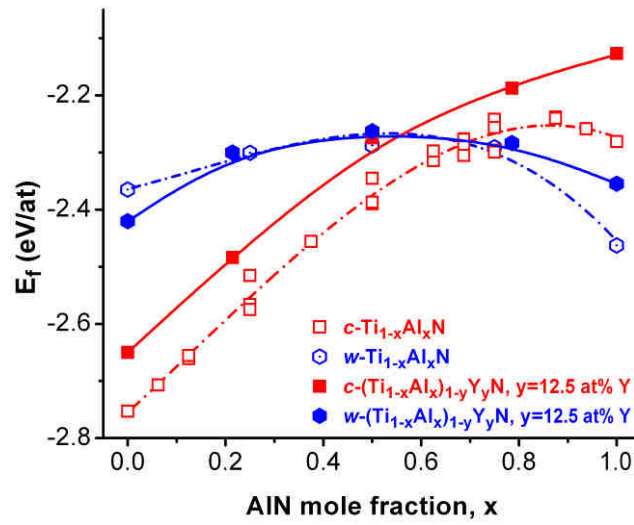

Fig. 5.8. The energy of formation E_f as a function of AlN mole fractions x for c-$Ti_{1-x}Al_xN$ and w-$Ti_{1-x}Al_xN$ (dash dotted line and open symbols) compared to E_f of c- and w-$(Ti_{1-x}Al_x)_{1-y}Y_yN$ with y=12.5 at.% Y at the metallic sub-lattice (solid line and full symbols) [44, 73] – Publication IV.

Fig. 5.8 shows a typical ab-initio calculation preformed for this thesis. It presents the energy of formation (E_f) distribution of cubic (c-) and hexagonal-wurtzite (w-) $Ti_{1-x}Al_xN$ as a function AlN mole fraction and compares it to the E_f distribution of c- and w-$(Ti_{1-x}Al_x)_{1-y}Y_yN$. For $Ti_{1-x}Al_xN$ the larger negative values of the cubic phase for x below ~0.69 indicate a preferred crystallization in the cubic modification [44]. Adding 12.5 at.% Y to the metallic sub-lattice equally substituting for Al and Ti results in $\geq$0.07 eV/at smaller negative E_f values for c-$(Ti_{1-x}Al_x)_{1-y}Y_yN$ over the entire x range. For the hexagonal modification w-$(Ti_{1-x}Al_x)_{1-y}Y_yN$ the E_f data for x in the AlN range 0.25-0.75 differ only by $\leq$0.01 eV/at from those of the Y-free w-$Ti_{1-x}Al_xN$. Comparing however the E_f data for cubic and hexagonal $(Ti_{1-x}Al_x)_{1-y}Y_yN$ with y=12.5 at.% suggests a preferred cubic modification for AlN mole fractions x below ~0.56. Consequently, the metastable

solubility limit for AlN in c-(Ti$_{1-x}$Al$_x$)$_{1-y}$Y$_y$N decreases from ~0.69 to 0.56 with increasing Y content from $y=0$ to 12.5 at.%, respectively. These computed data are in excellent agreement with experimental results from XRD (see Fig. 3.4) and TEM analyses suggesting a structural change from single-phased cubic to mixed cubic-hexagonal and further to an hexagonal-dominated microstructure (with cubic traces) by increasing the Y content from 0 to 3 or 5, and to 9 at.%, respectively. More details are presented in publication IV [73].

5.3.2 Sputter Process Modelling

In this thesis a calculation of the sputter yield Y_S and angular distribution of sputtered species α_S was performed using the Monte Carlo algorithm based TRIM group of programs which computes the stopping and range of ions into matter (SRIM) using a quantum mechanical treatment of ion-atom collisions [170]. The program builds on the binary collision approximation, where the movement of ions in the implanted sample (target) is treated as a succession of individual collisions between the recoil ion and atoms of the sample. With the program component TRIM (Transport of Ions in Matter) the effect of ions on complex multi-component target materials can be simulated and target damage, as well as quantity and angle of sputtered species are recorded. A full description of the calculation and the program package is presented in Refs. [170-172]. A screenshot of the SRIM calculation platform and collision cascade plots is shown in Fig. 5.9.
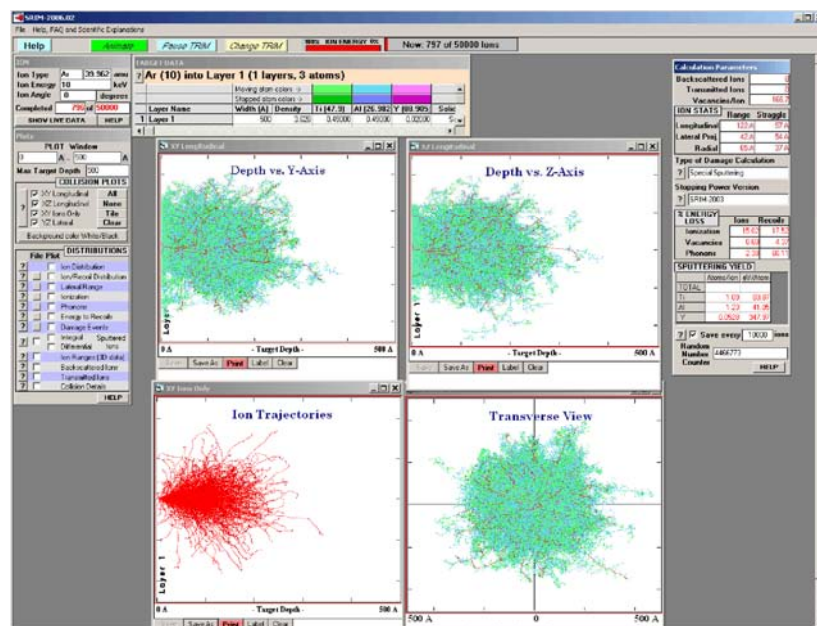

Fig. 5.9. Screenshot of a typical SRIM calculation showing the collision cascades and calculation as well as the data output sidebars [170].

The in the calculation used energies of the working gas ions, Ar^+ and N_2^+, are derived from the peak target voltages measured during DC- and pulsed DC-sputtering (see Fig. 4.6). Thus, the ion energies were set to 400 eV for DC-magnetron sputtering, and 900 and 1500 eV for pulsed DC-magnetron sputtering with t_{rev} = 1616 and 4979 ns, respectively. For DC-magnetron sputtering the sputter yields with Ar^+ and N_2^+ ($Y_{S, Ar}$ and $Y_{S, N2}$) are 3.9 and 3.3 for Al, and 3.6 and 3.1 for Ti, respectively. These values are comparable to those reported for single component targets [83, 89, 173]. Hence, the obtained sputter-yields for Ar^+ and N_2^+ suggest Ti/Al ratios of 0.85 and 0.86, respectively, and a metal sublattice composition of 54 at.% Al and 46 at.% Ti as presented in Fig. 5.10a and b. With increasing ion energy the sputter yield for Ti increases stronger than that for Al. The Ti/Al ratios are 0.86 and 0.88 for sputtering with 900 eV and 1500 eV Ar ions and 0.89 and 0.90 for sputtering with 900 eV and 1500 eV N_2 ions.
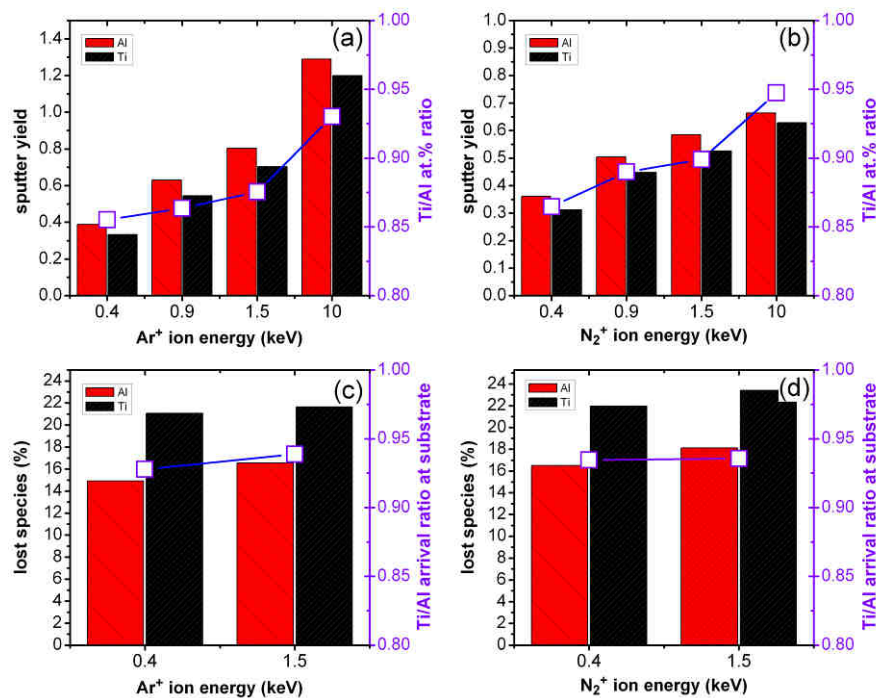

Fig. 5.10. Sputter yield and resulting Ti/Al at.% ratio at the substrate for Ar^+ (a) and N_2^+ (b) sputtering. The percentage of species sputtered at an angle larger than 25° (species do not reach the substrate) and the resulting Ti/Al substrate arrival ratio for Ar^+ (c) and N_2^+ (d) sputtering.

Generally, atoms are sputtered from the target in a range of directions proportional to a cosine distribution including the angel of incidence [174, 175]. Thus, a number of sputtered species does not reach the substrate. For the deposition arrangement utilized, the threshold angle from the target normal for atoms to impinge on the substrate is 25°. Hence,

~15% and ~21% of the Al and Ti atoms sputtered from a $Ti_{0.5}Al_{0.5}$ compound target are lost with 400 eV Ar^+. Using 400 eV N_2^+ as sputtering species ~17% Al and ~22% Ti would be lost (see Fig. 5.10c and d). Consequently, the different losses for Ti and Al atoms suggest a Ti/Al ratio of ~0.93 at the substrate. Together, the different sputter yields and losses for Ti and Al atoms suggest a Ti/Al ratio of ~0.79 for sputtering a $Ti_{0.5}Al_{0.5}$ compound target with Ar^+ ions having 400 eV. This value is in perfect agreement to the observed Ti/Al film ratio of 0.79±0.02 obtained during DC sputtering of a $Ti_{0.5}Al_{0.5}$ target, as reported in Refs. [47, 73].

Increasing the ion energy to 1500 eV results in a loss of 17 and 22% of Al and Ti and 18 and 23% of Al and Ti using Ar^+ and N_2^+ for sputtering, respectively. Consequently, the Ti/Al ratios of film forming species would increase from 0.93 to 0.94 with increasing ion energies from 400 to 1500 eV (Fig. 5.10c and d).

As presented in publication V, SRIM results were in excellent agreement with the coating compositions derived from SEM EDX analyses and helped thus in the understanding of the origin of the changes in chemical composition observed for the pulsed-magnetron sputtered films.

6 Mechanical Properties

In the development of protective coatings good mechanical properties are one key factor. They depend primarily on the binding strength, the thin film microstructure, its composition and constituents and are therefore a result of the deposition parameters and methods used for coating production. The most important strengthening mechanisms for the thin films produced in this thesis are presented in the following and the method of choice for hardness measurement, nanoindentation, is presented in chapter 6.2.

Further, a protective coating has to preserve the mechanical integrity of the subjacent substrate, which is from additional importance for γ-TiAl alloys and their intrinsically low fracture toughness. Therefore, the influence of coatings on the ductility of a γ-TiAl base alloy is investigated and the used technique presented in chapter 6.3.

6.1 Strengthening Mechanisms

The strength of crystalline materials is characterized by the resistance against deformation, which on its part is connected to the movement of dislocations. Therefore, mechanisms that limit dislocation movement will ultimately result in increased strength and hardness. Some of these processes are activated and others can be reduced through thermal input. Consequently, this chapter and chapter 7.1 on thermally activated processes are strongly interrelated.

6.1.1 Strain Hardening

Energetic particle bombardment during film growth affects the growth process of the material and generates lattice defects as presented in Fig. 6.1. When an incoming particle has high enough energy to knock atoms out of their lattice position, secondary collisions, and subsequently collision cascades form (Fig. 6.1a). In contrast to high energetic bombardment the cascade is not isotropic, resulting in strong atomic motion and rearrangement of the lattice. The impinging atoms as well as recoil species may also be implanted into the subsurface lattice. When energy and flux of the impinging ions are increased an increasing number of interstitials and vacancies is produced in the lattice from atomic displacements in collision cascades (Fig. 6.1b). These point defects result in an

increased density of extended defects and form two-, and three-dimensional defects such as dislocations, grain boundaries or voids [176, 177].
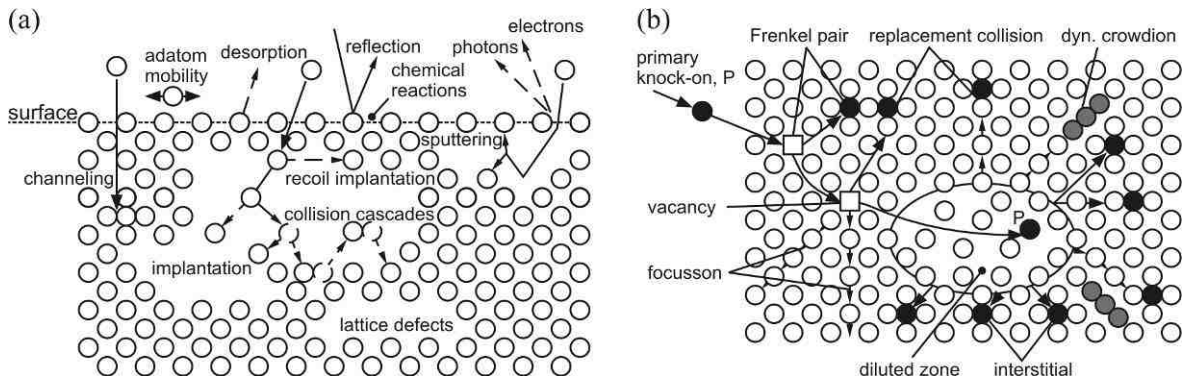

Fig. 6.1. (a) Effects of ion bombardment on a growing film and (b) interaction of an impinging high energetic particle with a metal lattice [96] (based on [176, 178, 179].

Strain hardening is also called *work- or defect hardening* especially for steels, and is caused by lattice defect – dislocation and/or dislocation – dislocation interactions. Dislocations as well as lattice defects, such as interstitials, have local strain fields around the lattice disturbance. For edge dislocations, for example, they are compressive above the slip plane and tensile below. When a moving dislocation meets the strain field of a lattice defect, i.e. interstitial or dislocation, it is either attracted or repulsed, which can lead to defect annihilation or to dislocation pile-up. Further, dislocations can intersect resulting in kinks or jogs, which also hinder further dislocation movement. Therefore, moving dislocations through such strain fields requires additional shear stresses to be applied. Consequently, a material with a high defect density appears harder and stronger [176].

As a consequence of ion bombardment and the growth process (chapter 5.2) poly-crystalline coatings have defect densities of $\sim 10^{12}$ cm^{-1} in the as-deposited state, comparable to highly deformed metals [83].

6.1.2 Solid Solution Hardening

The term solid solution depicts a system where alloying elements are integrated into the lattice of a crystalline metallic matrix. Depending on the atomic assembly two forms of solid solution are distinguished. If the alloying element is small compared to the matrix atoms, they sit preferable in interstitial lattice sites, Fig. 6.2a. On the other hand when atoms have similar sizes, the alloying elements may take the lattice space of matrix atoms, resulting in a substitutional solid solution, Fig. 6.2b. If two alloy components show

preferred bonding to each other as compared to elements of the same species, ordered solid solutions form, as presented in Fig. 6.2c. The solubility of one element in the crystalline matrix of an other can range from total insolubility to absolute solubility and for substitutional solutions is depending on the difference in atomic radius, in electronegativity, and in the difference in valence electrons. Also, solubility is generally limited when two species crystallize in different crystalline structures. As mentioned earlier, in equilibrium conditions the solubility limit of hexagonal AlN in cubic TiN is only ~5 mol.%. However, PVD processes allow the formation of metastable $Ti_{1-x}Al_xN$ solid solutions with up to 70 mole% AlN (chapter 3.2.1).
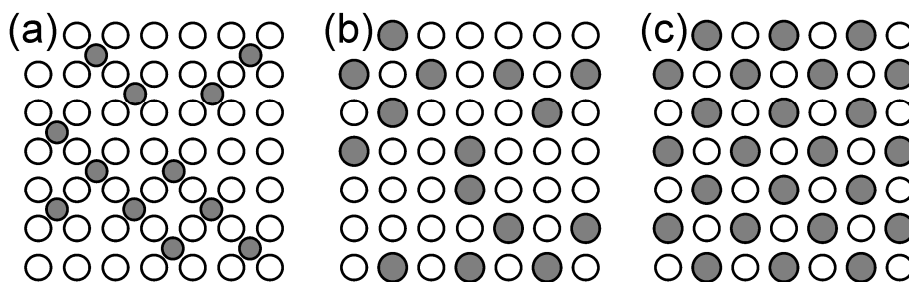

Fig. 6.2. Schematic of three different forms of solid solutions. (a) Alloying elements sit on interstitial sites; alloying elements substitute the hosting atoms randomly (b) or ordered (c). (modified from [180]).

Solid solution hardening is the result of changed bonding characteristics and alloy element interaction with dislocation movement where three different mechanism play a major role [180]: (1) *Paraelastic interactions*: due to the different size of alloying atoms compared to the matrix species, tensile or compressive stresses arise in the crystal lattice, which can act repulsively on dislocation movement. (2) *Dielastic interactions*: as binding energies in the neighbourhood of an alloying element are changed, also the shear modulus changes as compared to the pure metal leading to a hindered dislocation movement. (3) *Chemical interactions*: the staple fault energy generally decreases with increasing alloy content. With decreasing staple fault energy, however, the delamination width of dislocations to form partial dislocations increases, which in turn reduces the total energy. Therefore alloy elements (especially interstitials) diffuse to places around dislocations to reduce the staple fault energy. During dislocation movement a retarding force acts on the dislocation due to the changing alloy concentration environment [180].

Solid solution hardening is an often observed phenomenon in thin film systems. A famous examples is the herein discussed $Ti_{1-x}Al_xN$ system (see chapter 3.2.1, [42, 46, 52]), but also Ti-Zr-N [39, 181], or Cr-Al-N [182-184] show this mechanism of hardening.

6.1.3 Precipitation Hardening

Small particles embedded in the matrix of a material can considerably add to the strengthening due to their impeding effect on the movement of dislocations. Such particles, e.g. oxides or borides, can be given to the alloy already during the production process and are termed dispersoides. Particle or phases that form during thermal treatment of a solid solution are called precipitates. For precipitation hardening in addition to form and size, also their type of interface to the host matrix is from essential importance.

When a precipitation has coherent or semi-coherent interfaces with the matrix the crystallographic lattice planes are disturbed and distorted. In that case dislocations can move by cutting through the precipitation (Fig. 6.3, left side). To do so they have to overcome the energies needed to create new interfaces and anti-phase boundaries as well as paraelastic and dielastic interactions, resulting in increasing stresses necessary for the movement of dislocations. This increase in shear stress $\Delta\tau$ scales with the square root of particle size: $\Delta\tau_c \propto \sqrt{d_T}$ [176, 180, 186].
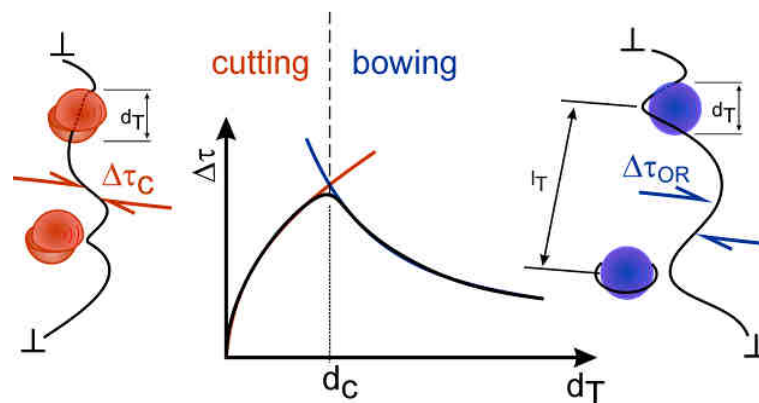

Fig. 6.3. Strengthening in dependence of dispersoide or precipitation size. $d_T^{0.5}$ dependence from cutting stress, and d_T^{-1} dependence from bowing stress yield a peak stress value at a critical particle size d_c (modified from [185]).

If a particle or precipitation has an incoherent interface with the matrix, dislocations cannot cut through, but have to bow out between two particles until they curl around the obstacle (Fig. 6.3 right side). Behind the particle anti-parallel dislocation parts meet, recombine, and a free dislocation can move-on, leaving a dislocation loop behind. This so called Orowan-mechanism participates to the overall strengthening increase by the decrease of particle spacing with each additional dislocation loop and by interactions between loop dislocations and incoming dislocations. For this mechanism the critical shear stress

decreases with increasing particle size ($\Delta\tau_c \propto \dfrac{1}{d_T}$), as at a given volume fraction of

particles the distance l_T between the particles increases. [176, 180, 186, 187].

Therefore, the critical shear stress for cutting of particles and precipitations increases by $\sqrt{d_T}$ until the Orowan-stress is reached leading to decreasing $\Delta\tau_c$ as it becomes easier for the dislocation to bypass the obstacle than to cut through it. This is schematically presented in Fig. 6.3.

6.2 Nano-Indentation

Indentation tests, or *hardness tests*, are amongst the most commonly applied methods for testing mechanical properties of a material. In traditional indentation tests, like those defined by Vickers, Brinell, or Rockwell, a hard tip with known mechanical properties (e.g diamond) is pressed into a material of unknown properties. The load placed on the indenter tip is increased until it reaches a user defined peak value. At this point, the load is kept constant for a certain time and/or removed. The area of residual indentation imprint is measured and the hardness, *H*, is defined as the maximum load, P_{max}, divided by the residual area A_r:

$$H = \frac{P_{\max}}{A_r} \tag{6.1}$$

A schematic of an indentation with a pyramidal indenter is presented in Fig. 6.4a. Upon loading with the force F the elasto-plastic behaviour of the material causes indentation to a depth h_{max}. The indenter, however, is in contact to the material only for the depth h_c. Due to the elastic recovery of the material the residual imprint after indentation has only the depth h_r [188, 189].

For the investigation of thin films the indentation depth has to be reduced to ~10% of the coating thickness [188] to minimize the influence of the substrate underneath, and therefore the applied load has to be low. Consequently, the residual imprint area is only a few square micrometers or even smaller, which would require SEM or atomic force microscopy for measuring the contact area.
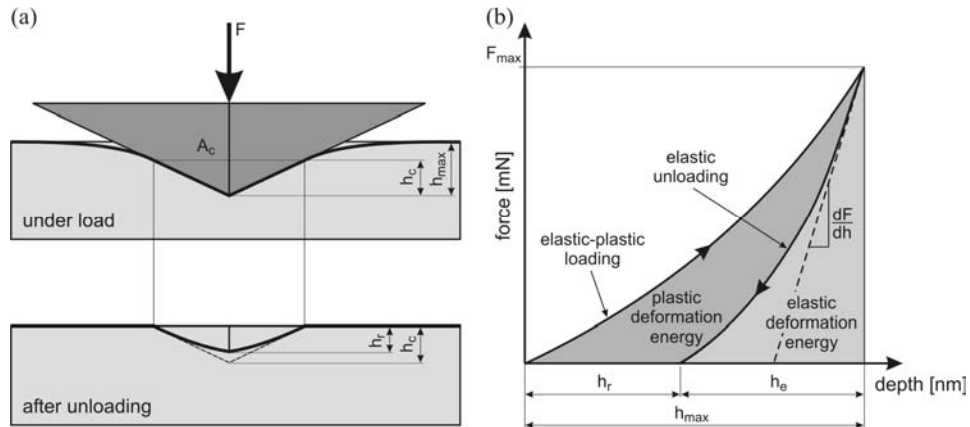
Fig. 6.4. (a) Schematic illustration of an indentation with a pyramidal indenter. (b) Schematic of a load-displacement trace [54].

Therefore, the method of choice for hardness measurements of thin films is depth sensing indentation or nano indentation. Here, the depth of penetration of an indenter into the sample material and the applied load are recorded and plotted in a load-displacement curve. From the load displacement traces (Fig. 6.4b) and the known geometry of the indenter the hardness and indentation modulus can be calculated. This requires however a well defined geometry of the indenter. In this work a Berkovich tip was utilized, which has the form of a three sided pyramid with a face-angle of 65.27° [188]. Another advantage of nano-indentation is, that the small indentation region as well as the computer controlled measuring equipment, allow a high number of indents on one sample, which provides excellent statistics and therefore good and reproducible hardness and modulus data.

The Oliver and Pharr method is widely accepted for evaluation of load-displacement curves and was also applied in this work. It uses a power law relation to fit the unloading segment of the load-displacement curve. According to the standard only the upper 80% of the unloading curve should be fitted for proper stiffness evaluation [190].

Here, the hardness of the produced coatings was not only measured in the as-deposited state but also after annealing to investigate the influence of microstructural changes on the mechanical properties. An example of such hardness versus annealing temperature curves is presented in Fig. 6.5.

The figure clearly demonstrates how thermally activated processes like recovery and decomposition –discussed in detail in chapter 7.1– lead to increases and decreases in hardness. Further, the intrinsically lower hardness of the hexagonal wurtzite AlN as compared to NaCl TiN is mirrored by the bimodal cubic- and hexagonal $Ti_{0.41}Al_{0.57}Y_{0.02}N$,

and hexagonal $Ti_{0.38}Al_{0.53}Y_{0.09}N$ coatings which have hardnesses of 23.54±1.39 and 22.21±0.44 GPa, respectively, as compared to single phase cubic-$Ti_{0.45}Al_{0.55}N$ with an averaged hardness of 34.59±2.83 GPa at room temperature.
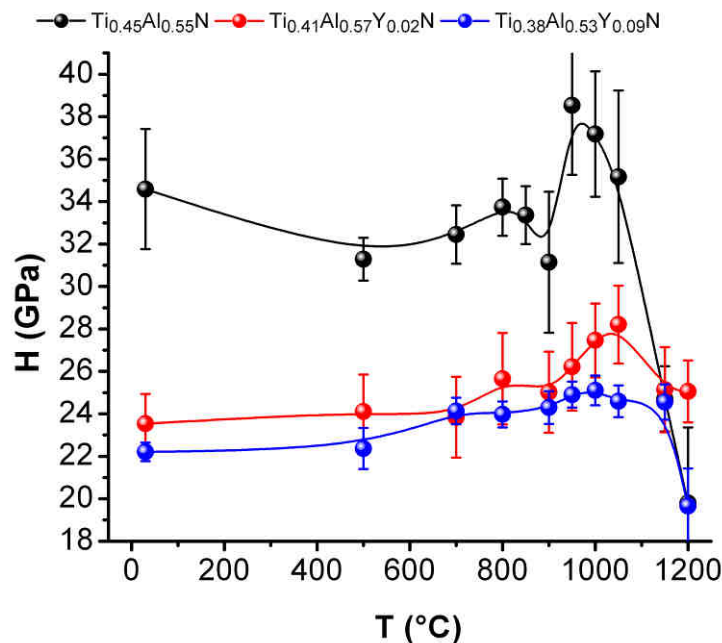

Fig. 6.5. Hardness distribution with annealing temperature of single phase cubic-$Ti_{0.45}Al_{0.55}N$, bimodal cubic- and hexagonal $Ti_{0.41}Al_{0.57}Y_{0.02}N$, and hexagonal $Ti_{0.38}Al_{0.53}Y_{0.09}N$.

Further details on this investigation are provided in Ref. [191]. In this thesis investigations of hardness and elastic modulus are presented also in publication I and publication V for Al-Au coatings and $(Ti_{1-x}Al_x)_{1-y}Y_yN$, respectively.

6.3 Substrate Ductility

When a coating is applied there is always atomistic interaction between the condensing material and the substrate at deposition temperature through ion bombardment or diffusion. Also, in subsequent annealing steps coating to substrate interaction may occur through interdiffusion of coating material in the substrate and vice versa resulting in a disturbed and mixed zone which may span from a couple of nanometres to hundreds of micrometer or more.

For brittle substrate materials, such as γ-TiAl based alloys, this interaction is from especial interest as it leads to a further deterioration of toughness and ductility. Therefore, in this

thesis the influence of coatings on the ductility of a γ-TiAl base alloy was investigated by four-point-bending tests.
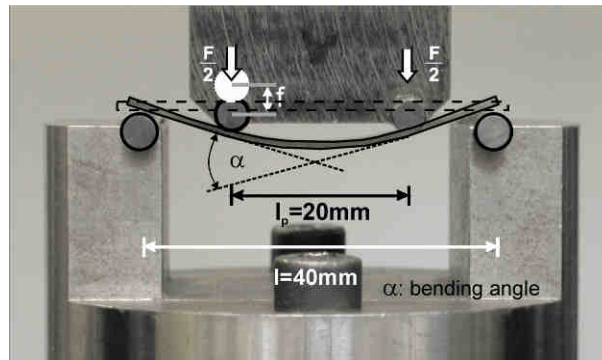

Fig. 6.6. Setup of the four-point-bending test as used for the investigations in this thesis – Publication VI [24, 127].

In this destructive test a sample is positioned movable in a universal testing machine. An upper stamp provides an increasing force until the sample breaks. A typical experimental arrangement is presented in Fig. 6.6. From the force versus cross-head displacement traces the bending strength R_{bb} is calculated according to [192, 193]:

$$R_{bb} = \frac{3}{2} \frac{F \cdot (l - l_p)}{bh^2},$$ (6.2)

where F is the applied force, l is the distance between the lower rolls, l_p is the distance between the upper rolls, b is the width of the sample and h its thickness. The maximum bending angle α as well as the strain ε in the outer fibre are given by

$$\alpha = 2 \cdot \arctan \frac{f}{0.5 \cdot (l - l_p)},$$ (6.3)

and

$$\varepsilon = \frac{4 \cdot h \cdot f \cdot c}{l_p^{\,2}},$$ (6.4)

where f is the cross-head displacement, c is a geometry factor for the bending cell, which was 0.27 for the Zwick instrument used inhere [24, 127].

The effect on the ductility of different coatings applied on a Ti-47Al-2Cr-0.2Si γ-TiAl based alloy is presented in Fig. 6.7. The uncoated material has an R_{bb} of 893±55 MPa and an α of 39.0±2.2°. Applying PVD CrAlYN or Al$_2$Au coatings on γ-TiAl results in small decreases in R_{bb} to 855±26 and 865±8.5 MPa, respectively (Fig. 6.7a). The bending angle however shows stronger decreases due to the inherent brittleness of the coatings and is

23.3±2.5° for CrAlYN coated, and 27.3±0.3° for Al_2Au coated γ-TiAl (Fig. 6.7b). Nevertheless, the performance of the PVD coatings is similar or better than found for commercial coatings like plasma-sprayed CoNiCrAlY, and pack-cementated Al-Cr or Ni-Al. Especially the pack-cementated coatings lead to strongly decreased ductility of the investigated γ-TiAl based alloy, which has only an R_{bb} of ~420 and 270 MPa and α below 10° when Al-Cr or Al-Ni coatings are applied, respectively.
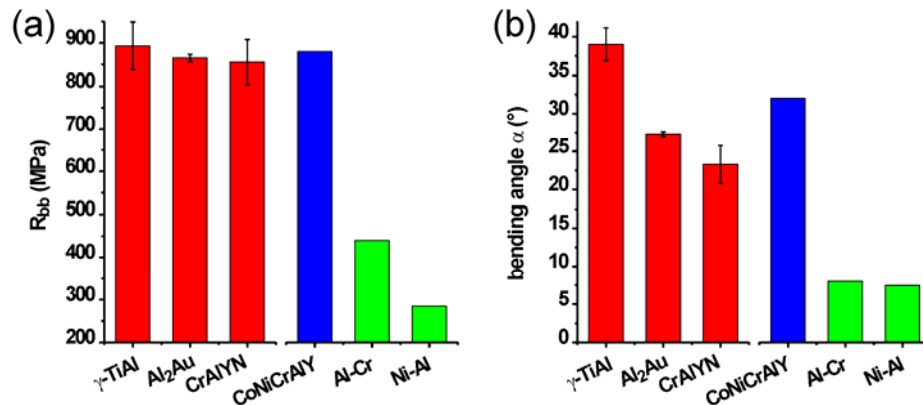

Fig. 6.7. Bending strength (a) and bending angle (b) of uncoated and coated γ-TiAl.

The investigations on the influence of coatings and oxidation on the bending strength γ-TiAl is presented in full detail in publication VI [24].

7 Thermal Stability

Upon thermal load, processes in materials are activated, allowing them to reach a low energy state. These processes are always accompanied by atomistic and structural changes and may lead to stress relaxation through recovery and recrystallization. During decomposition or transformation from metastable phases into their stable constituents stresses and strains can even increase. Therefore, it is essential in the development of protective coatings, to acquire good knowledge and understanding on extent and activation of such processes [37, 43, 83, 177].

Further, one key requirement for the herein developed coatings is to provide effective and sustained protection against oxidation of γ-TiAl base alloys. Consequently, this mechanism was studied in detail.

7.1 Thermally Activated Processes

Macroscopic changes in composition due to the random motion of individual atoms are called diffusion. Diffusion is a spontaneous process, and simply the statistically outcome of random motion, which may be driven by concentration gradients. Diffusion increases the entropy of a system and generally allows for decreases in the Gibbs free energy, and is therefore the requirement for an energetically driven process [176, 180].

There are several mechanisms of diffusion, which all need a certain thermal activation. Generally, the diffusion coefficient D determines the amount of observable transport commonly in cm^2/s, is depending on both, the diffusing species and the diffusion environment (lattice, grain-boundary, surface), and increases exponentially with temperature according to the Maxwell-Boltzmann relation:

$$D = D_0 \cdot e^{-\frac{Q}{k_B T}}, \tag{7.1}$$

where D_0 is the diffusion constant, depending amongst others on diffusing species and lattice, Q is the activation energy, k_B is the Boltzmann constant and T is the temperature [83, 180].

For interstitial solid solutions an atom can jump to the neighbouring interstitial lattice site. If the interstitial atom is small diffusion can be easy. For substitutional atoms diffusion is more difficult as the neighbouring lattice site is most likely occupied. Some possibilities

for atomic exchange are presented in Fig. 7.1, like direct atomic exchange (5), ring exchange (4), interstitial jumps (3, 2), or the jump to a vacancy position (1). Of the above mentioned mechanisms the interstitial has the smallest activation energy and is therefore the most likely to occur, whereas the activation energy for a direct atomic exchange is relatively high [180]. Vacancy diffusion plays a high role in crystalline films due to the high defect density from the low temperature growth out of the vapour phase (see chapter 6.1.1).
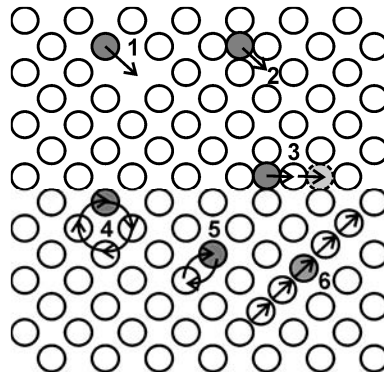

Fig. 7.1. Mechanisms of self diffusion: (1) jump to vacancy, (2) direct interstitial jump, (3) indirect interstitial jump, (4) ring exchange, (5) atomic exchange, (6) crowdion [180].

As the movement of atoms on a surface or interface is less disturbed, diffusion is much faster there. Thus, the activation energies for grain-boundary, dislocation and surface diffusion are lower than for lattice diffusion. Consequently, such heterogeneities or defects serve as diffusion paths, which short circuit the lattice. Small grain sizes, high defect densities and a large surface-to-bulk ratio in PVD thin films make diffusion along these pathways the dominating mechanism for coating materials. Diffusion through the lattice needs higher activation and therefore will onset at higher temperatures [83, 176, 180].

An example for high temperature diffusion of Au from decomposing Al_2Au into the γ-TiAl substrate material is presented in Fig. 5.1. Au rich layers form through Al surface diffusion by the formation of Al_2O_3. These are the source for further Au diffusion into γ-TiAl along grain boundaries, which are clearly visible by the high Au mass contrast.

7.1.1 Recovery and Recrystallization

Recovery and recrystallization occur in any crystal with a large concentration of non-equilibrium defects. This is highly valid for PVD coatings, where recovery and recrystallization processes will take place upon annealing at elevated temperature. These

processes result in a modified coating microstructure and consequently changed properties [177].

During recovery crystal defects heal in several stages according to their thermodynamic stability. The extent of recovery depends on annealing time and temperature, as well as on the energy stored in the crystal matrix (stress or strain), which can further act as driving forces. Recovery includes processes like the filling of vacancies by interstitial atoms, or the condensation of vacancies to vacancy clusters. Further, dislocations can annihilate through gliding, climbing or cross slipping, depending on the (stored) energy available. If excess dislocations can not be removed by annihilation, they will move into low energy configurations in the form of regular arrays or low angle grain boundaries [83, 106, 180].

Recrystallization involves the formation of new, low energy and strain free grains, which subsequently grow on the expense of the original or recovered microstructure. Recrystallization occurs through the formation and movement of high angle grain boundaries, and the removal of residual lattice defects. This is in contrast to recovery which comprises only the rearrangement and annihilation of point and line defects. Driven by a dislocation density gradient, the kinetic of recrystallization is dependent on nucleation and growth energies and is described by the S-shaped Johnson-Mehl-Avrami equation. After an incubation time, needed for nucleation of recrystallization, the fraction of recrystallized material rises rapidly until two crystals impinge on each other, resulting in a decreasing recrystallization rate until zero at full recrystallization. After this *primary recrystallization* process, a *secondary recrystallization* may follow, which is characterized by the growth of larger grains on the expense of small ones [83, 106, 176, 180].

As mentioned, recovery and recrystallization are driven by the need to reduce stored energy in the lattice. Consequently, these processes are accompanied by decreases in coating stress which can be investigated by a biaxial-stress temperature measurement as shown in Fig. 7.2. Here, biaxial stresses are analysed in-situ during vacuum annealing up to 700 °C from the measured curvature (r) of a Si(100) substrate using the modified Stony method [194-196]:

$$\sigma = \frac{E_S}{1-\nu_S} \frac{t_S{}^2}{6 \cdot t_C} \left(\frac{1}{r} - \frac{1}{r_0} \right), \tag{7.2}$$

where σ is the biaxial stress and the first term $E_S \cdot (1 - \nu_S)^{-1}$ is the biaxial elastic modulus of the substrate, ν_S is the Poisson's ratio of the substrate and r_0 indicates the radius of curvature prior to deposition. t_S and t_C denote the substrate and coating thickness, respectively. If the coating is very thin compared to the substrate ($100 \cdot t_C \leq t_S$) and comparable elastic moduli are given for the coating and substrate, the Stony equation is valid and the error involved in the equation is usually smaller than the experimental error of approximately 5% [194-196].
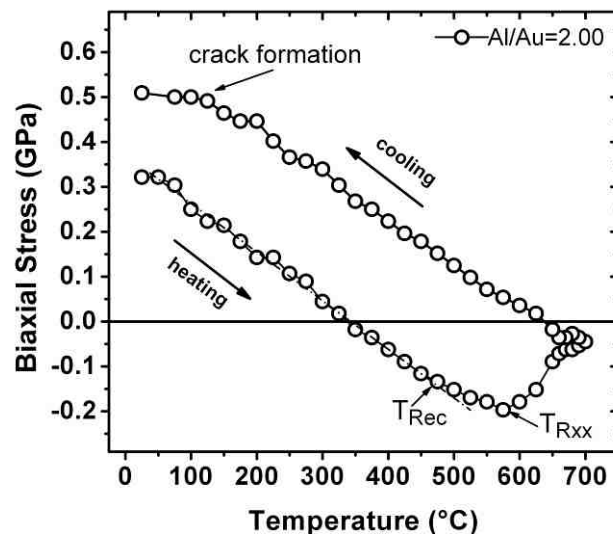

Fig. 7.2. Biaxial-stress temperature measurement cycle of the Al$_2$Au (Al/Au = 2.0) coating. The onset temperatures of recovery (T_{Rec}) and recrystallization are indicated (T_{Rxx}).

In the as deposited state, at room temperature, the Al$_2$Au film has tensile stresses of 0.31 GPa. Heating the film-substrate composite leads to a reduction of tensile stresses indicating that the coefficient of thermal expansion α is larger than that of the silicon substrate ($\alpha_{Si} = 3.55 \times 10^{-6}$ K^{-1}) [197]. During heating and cooling, the film/substrate composite follows the linear thermo-elastic line for temperatures where no recovery, recrystallization or plastic deformation takes place [198, 199]. The linear thermo-elastic behavior of the single-phase Al$_2$Au film ranges from 25 to 475 °C, well beyond the deposition temperature of 300 °C. The deviation above 475 °C suggests the onset of recovery which is followed by recrystallization above 575 °C – i.e. 0.65 of the homologues temperature for Al$_2$Au ($T_m = 1060$ °C)– and the subsequent reduction of thermally induced compressive stresses. Upon cooling at temperatures below 200 °C, crack formation results in a deviation from the thermo-elastic behavior, see Fig. 7.2. More details on the biaxial measurements done on the Al-Au coatings are provided in publication II.

7.1.2 Decomposition

In a solid solution the driving force of a system to decompose is described by the mixing enthalpy H_0. It is the energy a system of A and B atoms gains ($H_0 > 0$) or looses by creating AB-bonds from AA- and BB- bonds. Therefore, when $H_0 > 0$ a solid solution will decompose into its stable constituents.

Decomposition can take two pathways as presented in Fig. 7.3. In continues decomposition (Fig. 7.3a) seed crystals form though thermal fluctuations. These seed crystals have a composition far from the matrix, but close to the concentration of the equilibrium phase c_a'. When a critical crystallite size is reached, the grains can grow further by atomic diffusion processes creating a depletion zone of B atoms in the solid solution by the growth and enrichment of the B crystallites formed [51, 176, 180].
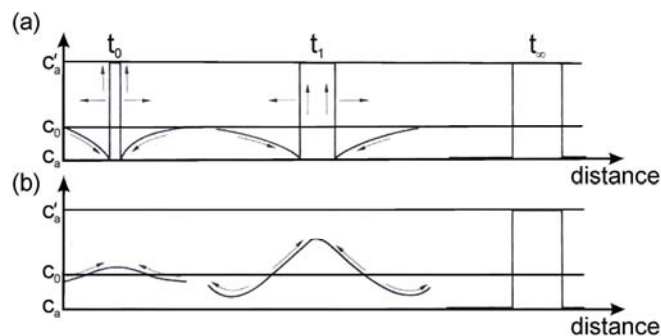

Fig. 7.3. Two possible pathways of decomposition ($t_1 \rightarrow t_2 \rightarrow t_\infty$). (a) through nucleation and growth of a second phase (downhill diffusion) and (b) through spinodal decomposition (uphill diffusion). c_a and c_a' are the equilibrium concentration of decomposed phases (modified from [176]).

In contrast to the continues decomposition, which requires a certain incubation time for the creation of a super-critical crystallite, the spinodal decomposition is a spontaneous process, where the equilibrium concentration is not reached immediately but through continues amplification until thermal equilibrium is reached Fig. 7.3b.

Generally, spinodal decomposition requires a solid solution composition in a miscibility gap near the maximum of the free energy versus concentration distribution as presented in Fig. 7.4. At decomposition at the concentration c_1 the free energy of the solid solution is given by the energy G_1, which is higher than the free energy of the decomposed material G_{1D}, given by the line c_1' – c_1''. Therefore, decomposition into the solid constituents is accompanied by a gain of free energy, which amplifies with further decomposition. Diffusion in spinodal decomposition moves in direction of concentration increase (uphill

diffusion) in contrast to the concentration equilibration in continuous decomposition. As a consequence of the above, spinodal decomposition is limited to the fraction of the G vs. c curve which is concavely bend, the region between the two inflection points, where $\partial^2 G/\partial c^2 = 0$. Thus, when $\partial^2 G/\partial c^2 < 0$ a solution is intrinsically unstable and will rapidly decompose into two phases via spinodal decomposition, whereas if $\partial^2 G/\partial c^2 > 0$ the solution is metastable and phase separation will take place via continuous decomposition [176, 180, 200].
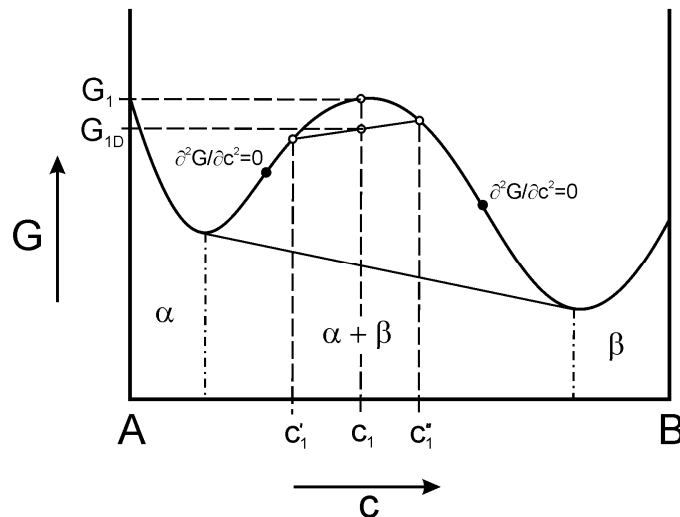

Fig. 7.4. Free energy distribution versus concentration of phase B at a constant temperature (modified from [180]).

Spinodal decomposition was observed and calculated for $Ti_{1-x}Al_xN$, where the spinodal decomposition at room temperature is predicted between AlN mole fractions x ~ 0.20 – 0.99 [43, 51, 201]. In Fig. 6.5 (chapter 7.2) $Ti_{0.45}Al_{0.55}N$ was found with a hardness maximum at 950 °C which is alleged to spinodal decomposition. At this temperature the calculated phase-diagram, showing the binodal and spinodal of $Ti_{1-x}Al_xN$ [51], predicts spinodal decomposition of $Ti_{0.45}Al_{0.55}N$ at 950 °C into 64 mole% $c\text{-}Ti_{0.70}Al_{0.30}N$ and 36 mole% $c\text{-}Ti_{0.04}Al_{0.96}N$. The further separation into the thermodynamically stable constituents requires nucleation processes.

7.1.3 Oxidation

Oxidation is generally described as a chemical reaction where one reactant is an electron donator and another is an electron acceptor. The latter is reduced by the electron addition. Therefore, oxidation chemically describes the loss of electrons and is always accompanied by a reduction reaction which is described as the gain of electrons [202].

At ambient temperatures engineering materials are either already oxidized, or an oxide layer protects the underlying material from further oxidation or slows down the reaction to very long time scales. Thus, at ambient temperature oxidation is not often of real concern, whereas required activation energies can be exceeded at elevated temperatures leading to drastically increased oxidation rates.

If an oxide is stable and non-volatile it remains on the metal surface resulting in the formation of an oxide scale, which forms in dependence of the reactant diffusion rates, the rate of oxygen supply to the outer surface, and the molar volume ratio of oxide to metal. The rate of oxidation is controlled by the slowest process at any given time. Due to the formation of oxides and the accompanied incorporation of oxygen atoms to the material, oxidation occurs with an increase in mass which can be measured. The formation of volatile oxides results in the reduction of sample weight [202-204].

These time dependent weight increases at a certain temperature are divided into three categories dependent on the shape of the weight gain versus time plot [202]:

(a) *Linear growth*, for which the rate of reaction is independent of time. This form is observed when the oxide is unable to hinder further access of oxygen to the metal surface, or if the oxide scale is not covering the entire sample surface. Linear scale growth is typical for high temperatures.

(b) *Parabolic growth*, where the mass increase distribution is inversely proportional to the square root of time. Here diffusion through the scale is the rate determining factor, as transport of metal and oxide ions becomes slower with scale thickness. The parabolic law is common for most metals.

(c) *Logarithmic growth*, where after fast initial oxide formation, the oxidation reaction reduces to nearly zero. This scale growth law is often observed at low temperatures of up to 400 °C, when a dense oxide layer forms, which impedes oxide inward diffusion. A typical example is aluminium below 50 °C.

The diffusion of species through a forming oxide scale is schematically presented in Fig. 7.5. Here the scale growth is governed by the inward diffusion of anions (oxygen) and cation vacancies (holes, h^+) and the outward diffusion of metal cations and electrons. This ionic transport across the growing oxide layer controls the rate of scale increase. Charge neutrality is achieved by the movement of h^+ and e^-.
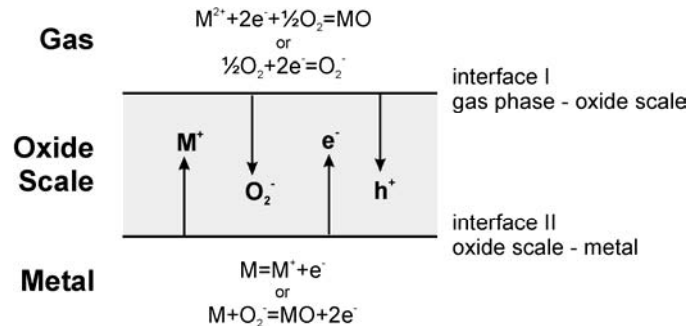
Fig. 7.5. Simplified model for diffusion controlled oxidation (modified from [96, 202]).

As discussed above, diffusion is faster along surfaces and grain boundaries (chapter 7.1). Therefore, these interfaces also act as pathways for oxidation [202-204]. Reactive elements such as yttrium are beneficial for oxide scale growth as they segregate to the metal-oxide scale interface and scale grain boundaries. This inhibits interfacial void growth, which is improving scale adhesion. The diffusion of RE outward along grain boundaries inhibits outward cation transport [11].

The above is only a very brief discussion of the complex field of oxidation. More detailed information on the theory and oxidation protective films is given in Refs. [202-206].
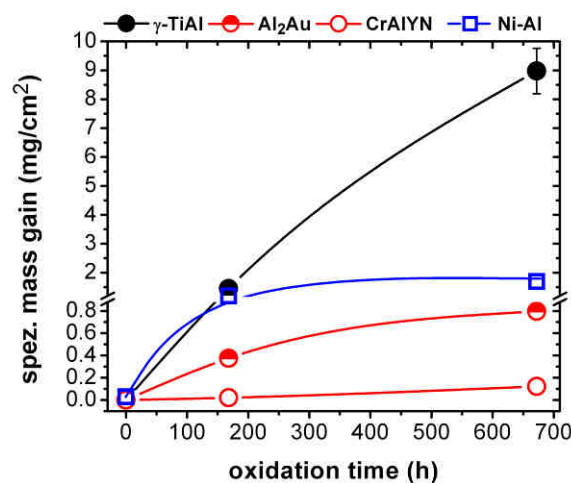

Fig. 7.6. Specific mass change as a function of time during isothermal oxidation in air at 800 °C of Al$_2$Au coated, CrAlYN coated and Ni-Al coated γ-TiAl compared to uncoated γ-TiAl (Publication VI [127]).

An example for an oxidation investigation conducted in the framework of this thesis is presented in Fig. 7.6 by a plot of the specific mass gain at 800 °C of uncoated, Al$_2$Au, and CrAlYN coated-, and Ni-Al pack-cemented γ-TiAl [127]. The unprotected γ-TiAl exhibits a rapidly increasing mass gain to 1.45±0.15 and 8.97±0.78 mg/cm^2 for t = 168 and 672 h, respectively. The coated materials have a much lower mass gain which is only 0.79±0.002

and 0.12±0.003 mg/cm^2 after 672 h at 800 °C for Al$_2$Au and CrAlYN, respectively. The specific mass gain of Ni-Al coated γ-TiAl of ~0.8 mg/cm^2 is comparable to Al$_2$Au but almost 8 times higher than for CrAlYN coated γ-TiAl. However, the shape indicates a logarithmic mass gain law, whereas the oxidation behaviour of Al$_2$Au fits to a parabolic function [15, 23]. Excellent oxidation behaviour is observed for the CrAlYN coating, which can be related to the oxidation retarding effect of the reactive element Y [207].

More details on oxidation testing and subsequent coating material investigations are presented in publication VI [127].

7.2 Thermal Analysis

The term thermal analysis generally refers to measurement methods where physical and/or chemical properties of a substance are determined as a function of time or temperature during exposure to a controlled temperature program [208, 209].

In this thesis simultaneous thermal analyses (STA) was utilized, which combines differential scanning calorimetry (DSC), thermo-gravimetric analysis (TGA), and mass spectrometry (MS).

DSC is a technique which measures the heat quantity, i.e. enthalpy, which is generated or consumed during a physical or chemical reaction. Reactions that result in an enthalpy increase are called endothermic and include melting and evaporation. When the enthalpy is decreased the reaction is termed exothermic. Such reactions include decomposition or crystallization. The heat flow to or from a sample is analysed by using a differential thermocouple that measures the temperature difference between the sample and a reference. Mass changes due to evaporation, oxidation or chemical reactions are measured by TGA. The measurement is done by electromagnetically or optoelectrically compensated balances. The mass spectrometer measures the mass to charge ratio of evaporated particles. More details on the MS unit are given in Refs. [208, 209].

Accordingly, STA allows a combined investigation and correlation of chemical reactions, their influence on sample mass, and the associated determination of evaporated or consumed species.

In this thesis thermal decomposition in inert atmosphere as well as under oxidative conditions was investigated by STA mostly by the continuous (dynamic) method at a

constant heating rate, whereas oxidation was also monitored by isothermal measurements. The scans were conducted on powdered coating material or on films deposited on inert substrates [35, 36, 191]. More details on the used equipment, sampling technique and temperature program are given in Refs. [54, 96].

An STA investigation of $(Ti_{1-x}Al_x)_{1-y}Y_yN$ films with $y = 0, 2, 9$ at.% Y is presented in Fig. 7.7. Powders of the coatings after chemical removal from the low alloyed steel foil substrates [35, 191, 210] are heated in inert Ar atmosphere to 1400 °C at a constant heating rate of 20 °C/min. Together with the hardness versus temperature plot shown in Fig. 6.5 and XRD pattern taken after sample annealing to temperatures slightly higher than the corresponding DSC peaks (not shown here), the thermal decomposition of the $(Ti_{1-x}Al_x)_{1-y}Y_yN$ coatings can be interpreted as follows:

During heating of the $(Ti_{1-x}Al_x)_{1-y}Y_yN$ films four exothermic reactions (a, b, c, and d indicated in Fig. 7.7) appear, which, however, have different origins depending on the Y mole fraction and the concomitantly different microstructure (see chapter 3.2.2, Fig. 3.4).

The $Ti_{0.45}Al_{0.55}N$ coating (Fig. 7.7, black line) has a single phase cubic microstructure. Upon annealing to around the deposition temperature of 550 °C, a decrease in hardness is observed but no changes in the XRD pattern. The exothermic reaction a_0 in the DSC curve Fig. 7.7a is therefore attributed to recovery and relaxation processes. A strong increase in hardness to ~38 GPa (from ~35 GPa at room temperature - Fig. 6.5) is observed at 950 °C, the temperature of the second reaction b_0, which is associated with the formation of coherent cubic AlN rich domains through spinodal decomposition of $Ti_{0.45}Al_{0.55}N$. At 1100 °C, the peak temperature of the third reaction c_0, the coating hardness has decreased to below 30 GPa. By XRD cubic TiN reflexes can be detected along with c-AlN and c-$Ti_{1-x}Al_xN$. The hardness decrease therefore results form the decomposition of the solid solution into TiN and the coarsening of c-AlN domains. Reaction d_0 at ~1300 °C is alleged to the transformation of c-AlN to hexagonal AlN, and to recrystallization through the total decomposition of the residual solid solution to c-TiN and h-AlN. This exothermic reaction is superimposed by the endothermic evaporation of super-stoichiometric nitrogen. This evaporation process is accompanied by a decrease in sample mass as shown in the TGA scan Fig. 7.7b and identified by MS in Fig. 7.7c by monitoring the N_2 content in the instrument atmosphere.

$Ti_{0.41}Al_{0.57}Y_{0.02}N$ (Fig. 7.7, red line) has a mixed cubic and hexagonal microstructure, resulting in a hardness of only 23.5 GPa at room temperature. Upon annealing to above 450 °C, the onset temperature of the first exothermic reaction a_2 observed in the DSC scan (Fig. 7.7a) is again associated with recovery effects. Reaction b_2 has a slightly higher enthalpy than b_0 of the Y free film. It is an effect of the decomposition of $c\text{-}Ti_{1-x}Al_xN$ domains, which is accompanied by the formation of c-AlN and hexagonal-$Ti_{1-x}Al_xN$, as indicated by the increase in peak intensity in the XRD pattern above 900 °C. Around the temperature of b_2 the hardness increases to 25.6 GPa and increases further to a peak value of 28.2 GPa at ~1100 °C (Fig. 6.5). This corresponds to the temperature of reaction c_2 which origins from the formation of c-TiN and h-AlN domains and resulting increased lattice strain. Reaction d_2 exhibits recrystallization and is accompanied by a mass loss of nitrogen (Fig. 7.7b) as observed for the $Ti_{0.45}Al_{0.55}N$ coating.
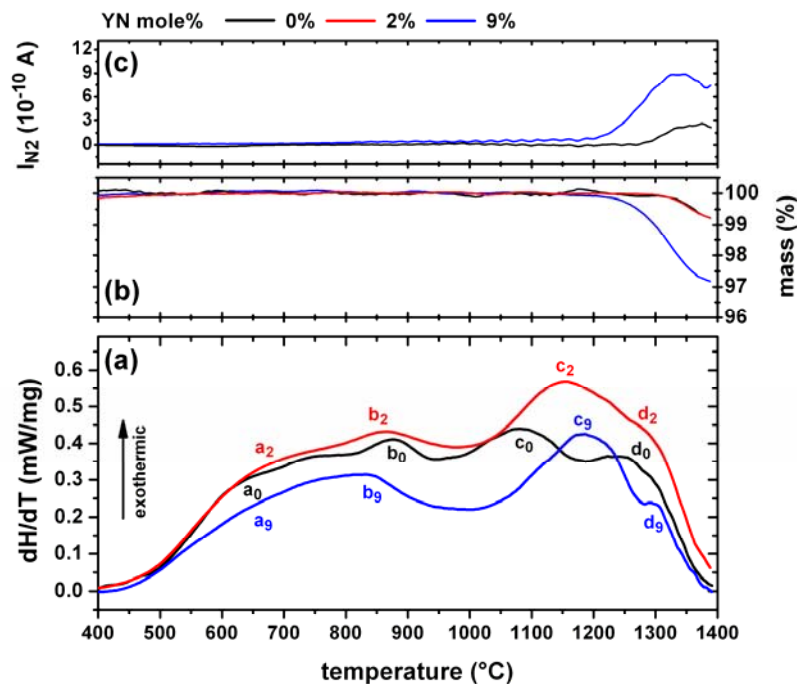

Fig. 7.7. Simultaneous thermal analysis in Ar atmosphere of single phase cubic-$Ti_{0.45}Al_{0.55}N$ (0 at.% Y), bimodal cubic- and hexagonal $Ti_{0.41}Al_{0.57}Y_{0.02}N$ (2 at.% Y), and hexagonal $Ti_{0.38}Al_{0.53}Y_{0.09}N$ (9 at.% Y): (a) DSC, (b) TGA, (c) MS monitoring N_2 [191].

The $(Ti_{1-x}Al_x)_{1-y}Y_yN$ coating with 9 at.% (Fig. 7.7, blue line) has a primarily hexagonal microstructure and a hardness of only 22.3 GPa at room temperature. After recovery and relaxation above 500 °C (DSC reaction a_9), first c-YN and h-AlN evolve from decomposition of the solid solution. The subsequently increased lattice strain results in a slightly higher hardness of 24.1 GPa, which further increases to 25.1 at 1000 °C (Fig. 6.5).

The latter increase is a result of the formation of c-TiN from hexagonal $(Ti_{1-x}Al_x)_{1-y}Y_yN$. Annealing to even higher temperatures above c_9 leads to a decrease in hardness due to the decomposition of the residual cubic- and hexagonal $(Ti_{1-x}Al_x)_{1-y}Y_yN$ solid solution and the formation of c-TiN and h-AlN domains. At the temperature of d_9, the equilibrium phases recrystallize and YN domains coarsen. This reaction is again superimposed by the evaporation of N_2 (Fig. 7.7c) and the subsequent mass loss (Fig. 7.7d).

8 Summary and Conclusion

γ-TiAl based alloys are considered for high temperature applications in aerospace and automotive industry due to their numerous attractive properties like low density, high yield strength and good creep resistance. However, their inherently low ductility and the fast formation of non protective TiO_2 scale upon oxidation above 750 °C limit their utilization at elevated temperatures. Therefore, coating systems have to be developed which not only provide protection against oxidation and high temperature corrosion, but can also preserve the mechanical properties of this class of alloys.

The structural evolution in dependence of coating composition and its influence on thermal stability, oxidation resistance and interaction with the γ-TiAl substrate material was investigated by two model PVD coating systems, metallic films based on the intermetallic Al_2Au phase and transition-metal nitride films based on $Ti_{0.5}Al_{0.5}N$.

Al-Au coatings with Al/Au at.% ratios between 1.85 and 4.32 were developed by unbalanced magnetron sputtering. Despite the majority phase in all films is the Zintl-type intermetallic Al_2Au, the microstructures of the various coatings differ significantly. Coatings with high Al contents like Al/Au = 4.32 have a binary microstructure, with a platelet like assembly of Al and Al_2Au phases of which the latter features layered nanosegregation of Al within its domains. When films are produced with high Au contents, i.e. Al/Au = 1.85, they grow with a globular, equiaxed and porous ternary phase structure composed of Al_2Au, AlAu, and Au. A dense columnar structure with strong (311) texture is observed for single phase Al_2Au. This phase has the highest energy of formation among neighbouring intermetallic phases. Consequently, it forms first upon nucleation. When the Al/Au atomic ratio in the vapour is 2, single-phase Al_2Au grows competitively according to zone T, resulting in the observed columnar structure at larger coating thicknesses. During deposition of a film with Al/Au = 4.32 the amount of Al, which is not consumed for Al_2Au formation, segregates to form Al domains. Due to the limited time during this diffusionally governed growth process, excess Al forms also nanosegregations within the Al_2Au domains. During growth of the Al/Au = 1.85 coating, the intermetallic phases nucleate and grow according to their heats of formation ($E_{f,Al_2Au} > E_{f,AlAu}$) The metallic Au phase forms metastable as a consequence of the limited atomic assembly kinetics often observed during low temperature plasma assisted vapour deposition and transforms into

intermetallic $AlAu_2$ and further to Al_2Au and $AlAu$ upon annealing. The formation of voids in this coating is attributed to the Kirkendall effect. Due to the metallic phases and pores present in the coatings with high concentration of Al and Au, these films have lower hardnesses but are tougher than the single phase Al_2Au film.

As a consequence of the different morphologies, the structural stability upon thermal load varies dramatically with coating composition. In coatings with high Au contents, i.e. Al/Au = 1.85, AlAu and $AlAu_2$ intermetallic phases, formed during deposition and from the metastable Au phase, melt at ~625 °C, whereas for coatings with Al/Au = 4.32 nanometer scale Al segregations encapsulated within the Al_2Au domains result in a reduction of the melting point of Al to 575 °C. Therefore, as the coatings with high Al or Au ratios grow phases with low melting points, theses materials are not suitable as high temperature protective films.

A single-phase Al_2Au coating, on the other hand, showed no detectable mass gain by oxidation in dynamic thermal analyses up to its melting point of 1060 °C. High-temperature XRD reveals Al_2Au with a retained microstructure up to a temperature of 850 °C, where Al_2O_3 formation through Al depletion is observed. Al_2O_3 forms a dense and protective scale resulting in a logarithmic mass gain behaviour in thermal cycling tests at 750 and 850 °C for 1000 h, and a considerably lower mass gain than observed for unprotected γ-TiAl.

Therefore, single-phase Al_2Au provides excellent oxidation protection up to temperatures of 850 °C due to the formation of a dense Al_2O_3 scale.

Mechanical testing of an Al_2Au coated γ-TiAl after one month of oxidation at 800 °C revealed an unacceptable decrease in ductility of the base material, due to the diffusion of Au along grain boundaries into the γ-TiAl substrate.

Metastable solid-solution $Ti_{1-x}Al_xN$ films have excellent physical, mechanical and chemical properties when they are grown in the fcc cubic NaCl structure. The addition of the reactive element yttrium is beneficial for the improvement of oxidation resistance in many materials as Y segregates to scale grain boundaries and inhibits outward cation transport. Therefore, one of the principle tasks in this thesis was to investigate the influence of yttrium addition on microstructure, mechanical properties and thermal stability of $Ti_{0.45}Al_{0.55}N$ coatings.

Based on XRD and TEM investigations it is revealed inhere that the cubic stability range of $Ti_{1-x}Al_xN$ is shifted to lower AlN mole fractions with the addition of yttrium. Alloying only 1 at.% Y to single-phase cubic $Ti_{0.45}Al_{0.55}N$ results in the formation of a binary phase composition of cubic- and hexagonal-$(Ti_{1-x}Al_x)_{1-y}Y_yN$. A coating with $y = 8$ at.% Y already has a predominantly hexagonal microstructure. Ab-initio calculations and XRD peak analyses show that Y substitutes for Al and Ti in the solid-solution lattice, and preferentially occupies lattice positions in the hexagonal phase. Calculations of the energy of formation of cubic- and hexagonal modifications of $Ti_{1-x}Al_xN$ and $(Ti_{1-x}Al_x)_{1-y}Y_yN$ predict that the addition of 12.5 at.% yttrium to $Ti_{1-x}Al_xN$ decreases the metastable solubility limit of the cubic structure by 23% from 0.69 to 0.56 AlN mole fractions.

Due to the intrinsically lower mechanical properties and decreased oxidation resistance of the hexagonal phase, cubic $(Ti_{1-x}Al_x)_{1-y}Y_yN$ films with maximum Al content have to be produced to guarantee a sustained protection of the γ-TiAl substrate material.

Applying bi-polar pulsed DC magnetron sputtering with low frequencies and long positive pulse duration results in the formation of single-phase cubic $(Ti_{1-x}Al_x)_{1-y}Y_yN$ coatings with $y = 2$ at.% Y. This improvement in phase composition can be accounted for by modified plasma conditions such as increased electron temperatures and ion-to-metal ratios with increasing pulse durations. These changes are further accompanied by an increasing Ti/Al at.% ratio.

In addition to the modified phase composition also the coating morphology of bi-polar pulsed DC magnetron sputtered $(Ti_{1-x}Al_x)_{1-y}Y_yN$ films changes in dependence of the positive pulse length. When coatings are prepared by DC magnetron sputtering, i.e. the positive pulse length is zero, or with low positive pulse lengths, the films grow with a cubic <200> texture at the interface near region with the growth direction perpendicular to the substrate surface. With increasing coating thickness and consequently increasing accumulating strain energies the <111> orientation becomes preferred, which is accompanied by the formation of <0002> orientated hexagonal crystals. As a consequence of the combined growth and an orientation relation between <111> cubic and <0002> hexagonal phases, the columnar structure in this zone is tilted to the substrate normal. However, with increasing positive pulse durations and therefore increasing ion-to-metal ratios in the vapour flux and Ti/Al at.% ratios in the coating, the cubic <200> textured

microstructure is stabilized to larger thicknesses or even throughout the total coating diameter.

Therefore, at longest positive pulse durations and low pulse frequencies single-phase cubic $(Ti_{1-x}Al_x)_{1-y}Y_yN$ coatings with <200> texture can be grown, which have the excellent mechanical properties of $Ti_{1-x}Al_xN$ films and increased oxidation stability due to the incorporation of yttrium.

In conclusion, by systematically analysing the microstructure and evolution of two inherently different coating systems this work provides important pathways for the further development of protective coatings for γ-TiAl based alloys. It is demonstrated that the PVD process is an excellent tool for protective coating deposition, and is especially for γ-TiAl superior to processes like pack-cementation or electro-plating which are well established for Ni-base superalloy protection. Nevertheless, future coating designs have to adopt system approaches of γ-TiAl alloys, which are not sensitive to the deposition process and subsequent coating-substrate interaction, and of a coating material that provides effective and sustained protection for the substrate.

9 References

[1]   IPCC, Summary for Policymakers, Intergovernmental Panel on Climate Change, Cambridge University Press, Cambridge, United Kingdom and New York, NY, USA, 2007.

[2]   M.R. Raupach, G. Marland, P. Ciais, C. Le Quere, J.G. Canadell, G. Klepper, C.B. Field, Proc. Natl. Acad. Sci. U. S. A. 104/24 (2007) 10288.

[3]   IPCC, SPECIAL REPORT - Aviation and the Global Atmosphere, Intergovernmental Panel on Climate Change, Cambridge University Press, Cambridge, United Kingdom and New York, NY, USA, 1999.

[4]   E.A. Loria, Intermetallics 8/9-11 (2000) 1339.

[5]   M. Weimer, T. Kelly, *Gamma TiAl Applications at GE Aviation*, oral presentation given at the TMS 2008 annual meeting: Structural Aluminides for Elevated Temperature Applications Symposium, New Orleans, 2008.

[6]   G.H. Meier, in: H.J. Grabke, M. Schütze (Eds.), Oxidation of Intermetallics, Wiley-VCH, Weinheim, 1996, p. 15.

[7]   C. Xu, C.D. Breach, T. Sritharan, F. Wulff, S.G. Mhaisalkar, Thin Solid Films 462-463 (2004) 357.

[8]   H.C. Shih, Z. Metallkd. 71/9 (1980) 577.

[9]   S. PalDey, S.C. Deevi, Materials Science and Engineering A 342/1-2 (2003) 58.

[10]   L.A. Donohue, I.J. Smith, W.D. Münz, I. Petrov, J.E. Greene, Surf. Coat. Technol. 94-95 (1997) 226.

[11]   B.A. Pint, Oxidation of Metals 45/1-2 (1996) 1.

[12]   K. Przybylski, G.J. Yurek, Mater. Sci. Forum 43 (1989) 1.

[13]   H. Clemens, A. Lorich, N. Eberhardt, W. Glatz, W. Knabl, H. Kestler, Zeitschrift für Metallkunde/Materials Research and Advanced Techniques 90/8 (1999).

[14]   F. Appel, M. Oehring, in: C. Leyens, M. Peters (Eds.), Titanium and Titanium Alloys: Fundamentals and Applications, Wiley-VCH, Weinheim, 2003, p. 89.

[15]   H.-P. Martinz, H. Clemens, W. Knabl, in: G. Kneringer, P. Rödhammer, P. Wilhartitz (Eds.), 14th International Plansee Seminar, Plansee AG, Reutte, 1997, p. 887.

[16]   Y.W. Kim, Acta Metallurgica Sinica Series A, Physical Metallurgy & Materials Science 8/4-6 (1995) 319.

[17]   S.-C. Huang, in: R. Darolia, J.J. Lewandowski, C.T. Liu, L. Martin, D.B. Miracle, M.V. Nathal (Eds.), Structural Intemetallics, TMS, Warrandale, PA, 1993, p. 299.

[18]   T.T. Cheng, M.R. Willis, I.P. Jones, Intermetallics 7/1 (1999) 89.

[19]   P.I. Gouma, M. Karadge, Mater. Lett. 57/22-23 (2003) 3581.

[20]   J.P. Chevalier, M. Lamirand, J.L. Bonnentien, Materials Research Society Symposium Proceedings, 2005, p. 145.

[21] H. Chladil, Doctoral Thesis, Department Physical Metallurgy and Materials Testing, Montanuniversität Leoben, Leoben, 2007.

[22] F. Appel, U. Brossmann, U. Christoph, S. Eggert, P. Janschek, U. Lorenz, J. Müllauer, M. Oehring, J.D.H. Paul, Adv. Eng. Mat. 2/11 (2000) 699.

[23] H.-P. Martinz, H. Clemens, W. Knabl, in: Y.-W. Kim, D.M. Dimiduk, M.H. Loretto (Eds.), Gamma Titanium Aluminides - The Minerals, Metals & Materials Society, Warrandale, Pa., 1999, p. 829.

[24] M. Moser, P.H. Mayrhofer, H. Clemens, Structural Aluminides for Elevated Temperature Applications, The Minerals, Metals & Materials Society, 137th Annual Meeting Proceedings, Wiley-VCH, New Orleans, 2008, p. in print.

[25] M. Li, C. Li, F. Wang, D. Luoa, W. Zhang, J. Alloys Compd. 385 (2004) 199.

[26] C. Mitterer, H. Lenhart, P.H. Mayrhofer, M. Kathrein, Intermetallics 12 (2004) 579.

[27] M. Moser, P.H. Mayrhofer, I.M. Ross, W.M. Rainforth, J. Appl. Phys. 102/2 (2007).

[28] W.C. Roberts-Austen, Proc. R. Soc. London, A 41 (1891) 341.

[29] C.W. Horsting, 10th IEEE Annual Proceedings, Reliability Physics Symp., Las Vegas, Nevada, 1972, p. 155.

[30] R.W. Cahn, Nature (London) 396 (1998) 523.

[31] C. Xu, T. Sritharan, S.G. Mhaisalkar, Thin Solid Films 515/13 (2007) 5454.

[32] C. Xu, T. Sritharan, S.G. Mhaisalkar, Scripta Mater 56/6 (2007) 549.

[33] C. Xu, T. Sritharan, S.G. Mhaisalkar, M. Srinivasan, S. Zhang, Appl. Surf. Sci. 253/14 (2007) 6217.

[34] U. Dehlinger, Ztschr. Elektrochem. 41/6 (1935) 344.

[35] M. Moser, P.H. Mayrhofer, I.M. Ross, W.M. Rainforth, J. Vac. Sci. Technol., A 25/5 (2007) 1402.

[36] M. Moser, P.H. Mayrhofer, R. Braun, Materials Research Society Symposium Proceedings, 2007, p. 431.

[37] L. Hultman, Vacuum 57/1 (2000) 1.

[38] W.D. Münz, J. Vac. Sci. Technol., A 4/6 (1986) 2717.

[39] O. Knotek, W.D. Münz, T. Leyendecker, J. Vac. Sci. Technol., A 5/4 (1987) 2173.

[40] T. Massalski (Ed.), Binary Alloy Phase Diagrams, ASM International, 1990.

[41] H. Holleck, Surf. Coat. Technol. 36/1-2 (1988) 151.

[42] M. Zhou, Y. Makino, M. Nose, K. Nogi, Thin Solid Films 339 (1999) 203.

[43] P.H. Mayrhofer, A. Horling, L. Karlsson, J. Sjolen, T. Larsson, C. Mitterer, L. Hultman, Appl. Phys. Lett. 83/10 (2003) 2049.

[44] P.H. Mayrhofer, D. Music, J.M. Schneider, J. Appl. Phys. 100/9 (2006) 094906.

[45] R. Cremer, M. Witthaut, D. Neuschütz, in: W.D. Cho, H.Y. Sohn (Eds.), Value-Edition-Metallurgy, The Minerals & Metals Society, Warrendale, PA, 1998, p. 249.

[46] A. Kimura, H. Hasegawa, K. Yamada, T. Suzuki, Surf. Coat. Technol. 120-121 (1999) 438.

[47] K. Kutschej, P.H. Mayrhofer, M. Kathrein, P. Polcik, R. Tessadri, C. Mitterer, Surf. Coat. Technol. 200/7 (2005) 2358.

[48] A. Hörling, L. Hultman, M. Oden, J. Sjolen, L. Karlsson, Surf. Coat. Technol. 191/2-3 (2005) 384.

[49] H.W. Hugosson, H. Högberg, M. Algren, M. Rodmar, T.I. Selinder, J. Appl. Phys. 93/8 (2003) 4505.

[50] H. Stolten, P. Spencer, D. Neuschutz, J. Chim. Phys. Phys.-Chim. Biol. 90/2 (1993) 209.

[51] P.H. Mayrhofer, D. Music, J.M. Schneider, Appl. Phys. Lett. 88/7 (2006) 071922.

[52] A. Hörling, L. Hultman, M. Oden, J. Sjolen, L. Karlsson, J. Vac. Sci. Technol., A 20/5 (2002) 1815.

[53] U. Wahlström, L. Hultman, J.E. Sundgren, F. Adibi, I. Petrov, J.E. Greene, Thin Solid Films 235/1-2 (1993) 62.

[54] H. Willmann, Doctoral Thesis, Department Physical Metallurgy and Materials Testing, Montanuniversität Leoben, Leoben, 2007.

[55] Q.G. Zhou, X.D. Bai, X.Y. Xue, X.W. Chen, J. Xu, D.R. Wang, Surf. Coat. Technol. 191/2-3 (2005) 212.

[56] S. Jiang, D. Peng, X. Zhao, L. Xie, Q. Li, Appl. Surf. Sci. 84/4 (1995) 373.

[57] C.W. Kim, K.H. Kim, Thin Solid Films 307/1-2 (1997) 113.

[58] K.H. Kim, S.H. Lee, Thin Solid Films 283/1-2 (1996) 165.

[59] A. Mitsuo, S. Uchida, N. Nihira, M. Iwaki, Surf. Coat. Technol. 103-104 (1998) 98.

[60] D. McIntyre, J.E. Greene, G. Hakansson, J.E. Sundgren, W.D. Munz, J. Appl. Phys. 67/3 (1990) 1542.

[61] C. Leyens, in: C. Leyens, M. Peters (Eds.), Titanium and Titanium Alloys, Wiley-VCH, Weinheim, 2003, p. 187.

[62] R. Braun, D. Müßener, M. Moser, F. Rovere, P.H. Mayerhofer, C. Leyens, Structural Aluminides for elevated Temperature Application, The Minerals, Metals & Materials Society, 137th annual meeting proceedings, New Orleans, 2008.

[63] F. Vaz, L. Rebouta, M. Andritschky, M.F. da Silva, J.C. Soares, J. Eur. Ceram. Soc. 17/15-16 (1997) 1971.

[64] B.Y. Man, L. Guzman, A. Miotello, M. Adami, Surf. Coat. Technol. 180-181 (2004) 9.

[65] G.W. Goward, Surf. Coat. Technol. 108-109/1-3 (1998) 73.

[66] F.H. Stott, Mater. Sci. Technol. 4/5 (1987) 431.

[67] R. Prescott, M.J. Graham, Oxidation of Metals 38/3-4 (1992) 233.

[68] V. Provenzano, K. Sadananda, N.P. Louat, J.R. Reed, Surf. Coat. Technol. 36/1-2 (1988) 61.

[69]   J. Stringer, Materials Science and Engineering A A120-1/1 -2 pt 1 (1989) 129.

[70]   H.M. Tawancy, N.M. Abbas, A. Bennett, Surf. Coat. Technol. 68-69 (1994) 10.

[71]   J. Zhujing, L. Changquig, Y. Li, W. Weitao, Surf. Coat. Technol. 46 (1991) 307.

[72]   D.B. Lewis, L.A. Donohue, M. Lembke, W.D. Munz, R. KuzelJr, V. Valvoda, C.J. Blomfield, Surf. Coat. Technol. 114/2-3 (1999) 187.

[73]   M. Moser, P.H. Mayrhofer, Scripta Mater 57/4 (2007) 357.

[74]   M. Moser, P.H. Mayrhofer, L. Szèkely, G. Sáfrán, P.B. Barna, Surf. Coat. Technol. submitted (2008).

[75]   P.C. Patnaik, Materials and Manufacturing Processes 4/1 (1989) 133.

[76]   G.W. Goward, NATO ASI Ser., Ser. E, 1984, p. 408.

[77]   P. Fauchais, A. Vardelle, B. Dussoubs, Journal of Thermal Spray Technology 10/1 (2001) 44.

[78]   S. Kuroda, Proceedings of the International Thermal Spray Conference, 1998, p. 539.

[79]   T.W. Gargeda, V. Lanza, A.H. Roebuck, Journal of Protective Coatings and Linings 3/1 (1986) 44.

[80]   B. Waldie, IEE Colloquium (Digest), 1986, p. 4. 1.

[81]   M.I. Boulos, Pure Appl. Chem. 68/5 (1996) 1007.

[82]   H. Herman, K. LaPierre, International SAMPE Electronics Conference 24 (1992) 43.

[83]   M. Ohring, The Materials Science of Thin Films, Academic Press, London, 1992.

[84]   A. Matthews, in: J.S. Brunell-Gray, P.K. Datta (Eds.), Surface Engineering Casebook, Woodhead Publishing Ltd., Cambridge, 1996, p. 23.

[85]   M.G. Hocking, V. Vasantasree, P.S. Sidky, Metallic and Ceramic Coatings, Longman Scientific & Technical, Essex, 1989.

[86]   G. Kienel, P. Sommerkamp, in: G. Kienel, K. Röll (Eds.), Vakuum-Beschichtung, vol. 2: Verfahren und Anlagen, VDI Verlag, Düsseldorf, 1995, p. 20.

[87]   E. Moll, W. Gissler, H.A. Jehn, (eds.), Advanced Techniques for Surface Engineering, Kluwer Academic Publisher, Dordrecht, 1992.

[88]   A. Grill, Cold Plasma in Materials Fabrication, IEEE Press, New York, 193.

[89]   B. Chapman, Glow Discharge Processes - Sputtering and Plasma Etching, John Wiley & Sons, New York, 1980.

[90]   M.A. Liebermann, A.J. Lichtenberg, Principles of Plasma Discharges and Materials Processing, John Wiley & Sons Inc., New York, 1994.

[91]   H. Frey, Vakuum-Beschichtung 1: Plasmaphysik-Plasmadiagnostik-Analytik, VDI Verlag, Düsseldorf, 1995.

[92]   N.G. Einspruch, D.M. Brown (Eds.), VLSI Electronics Microstructure Science, Academic Press, New York, 1984.

[93]   I. Langmuir, Physical Review 33/6 (1929) 954.

[94]   I. Petrov, V. Orlinov, I. Ivanov, J. Kourtev, Contrib. Plasma Phys. 28/2 (1988).

[95]   I.H. Hutchinson., Principles of Plasma Diagnostics, Cambridge University Press, Cambridge, 2002.

[96]   P.H. Mayrhofer, Doctoral Thesis, Department Physical Metallurgy and Materials Testing, Montanuniverstiät Leoben, Leoben, 2001.

[97]   A.A. Sonin, AIAA Journal 4/9 (1965) 1588.

[98]   A.A. Sonin, University of Toronto Institute for Aerospace Studies (UTIAS) report 109 (1965) 1.

[99]   I. Petrov, P.B. Barna, L. Hultman, J.E. Greene, J. Vac. Sci. Technol., A 21/5 (2003) S117.

[100]   I. Petrov, F. Adibi, J.E. Greene, W.D. Sproul, W.D. Münz, J. Vac. Sci. Technol., A 10/5 (1992) 3283.

[101]   F. Adibi, I. Petrov, J.E. Greene, L. Hultman, J.E. Sundgren, J. Appl. Phys. 73/12 (1993) 8520.

[102]   J.W. Lee, J.J. Cuomo, M. Bourham, J. Vac. Sci. Technol., A 22/2 (2004) 260.

[103]   J.W. Bradley, H. Bäcker, P.J. Kelly, R.D. Arnell, Surf. Coat. Technol. 142-144 (2001) 337.

[104]   J.W. Bradley, H. Bäcker, P.J. Kelly, R.D. Arnell, Surf. Coat. Technol. 135/2-3 (2001) 221.

[105]   D.A. Glocker, J. Vac. Sci. Technol., A 11 (1993) 2989.

[106]   D.L. Smith, Thin-Film Deposition: principle and practice, McGraw-Hill, New York, 1995.

[107]   R.A. Haefer, Oberflächen und Dünnschicht-Technologie, Springer, Berlin, 1987.

[108]   W.D. Sproul, D.J. Christie, D.C. Carter, Thin Solid Films 491/1-2 (2005) 1.

[109]   P.J. Kelly, C.F. Beevers, P.S. Henderson, R.D. Arnell, J.W. Bradley, H. Bäcker, Surf. Coat. Technol. 174-175 (2003) 795.

[110]   J. Sellers, Surf. Coat. Technol. 98/1-3 (1998) 1245.

[111]   R.D. Arnell, P.J. Kelly, J.W. Bradley, Surf. Coat. Technol. 188-189 (2004) 158.

[112]   J.W. Lee, S.K. Tien, Y.C. Kuo, Thin Solid Films 494/1-2 (2006) 161.

[113]   H.C. Barshilia, K.S. Rajam, Surf. Coat. Technol. 201/3-4 (2006) 1827.

[114]   M. Audronis, P.J. Kelly, A. Leyland, A. Matthews, Thin Solid Films 515/4 (2006) 1511.

[115]   J. Vlcek, A.D. Pajdarova, J. Musil, Contributions to Plasma Physics 44/5-6 (2004) 426.

[116]   H. Bäcker, P.S. Henderson, J.W. Bradley, P.J. Kelly, Surf. Coat. Technol. 174-175 (2003) 909.

[117]   T. Moiseev, D.C. Cameron, J. Vac. Sci. Technol., A 23/1 (2005) 66.

[118]   M. Audronis, P.J. Kelly, R.D. Arnell, A. Leyland, A. Matthews, Surf. Coat. Technol. 200/5-6 (2005) 1366.

[119] R. Allmann, Röntgen-Pulverdiffractometrie: Rechnergestützte Auswertung, Phasenanalyse und Strukturbestimmung, Springer, Berlin, 2003.

[120] B.D. Cullity, S.R. Stock, Elements of X-ray diffraction, Prentice Hall, New Jersey, 2001.

[121] M. Birkholz, Thin film analysis by X-ray scattering, Wiley-VCH, Weinheim, 2006.

[122] W.H. Bragg, W.L. Bragg, Proceedings of the Royal Society of London. Series A, Containing Papers of a Mathematical and Physical Character 88/605 (1913).

[123] P. Goodhew, A. Fretwell, www.matter.org.uk/diffraction/, The University of Liverpool, 2000.

[124] J.I. Langford, J. Appl. Cryst. 11 (1978) 10 11 (1978) 10.

[125] C.N.J. Wagner, in: J.B. Cohen, J.E. Hillard (Eds.), Local Atomic Arrangements Studied by X-ray Diffraction, Gordon and Breach, NY, 1966.

[126] W. Gissler, J.H.i.W. Gissler, in: W. Gissler, H.A. Jehn (Eds.), Kluwer Academic Publishers, Dortrecht, 1992, p. 313.

[127] M. Moser, P.H. Mayrhofer, H. Clemens, Intermetallics (2008) submitted.

[128] D.B. Williams, C.B. Carter, Transmission Electron Microscopy: Vol.1 Basics, Springer Science + Business Media Inc., New York, 1996.

[129] D.B. Williams, C.B. Carter, Transmission Electron Microscopy: Vol.2 Diffraction, Springer Science + Business Media Inc., New York, 1996.

[130] D.B. Williams, C.B. Carter, Transmission Electron Microscopy: Vol.3 Imaging, Springer Science + Business Media Inc., New York, 1996.

[131] D.B. Williams, C.B. Carter, Transmission Electron Microscopy: Vol.4 Spectrometry, Springer Science + Business Media Inc., New York, 1996.

[132] P. Goodhew, D. Brook, B. Tanovic, A. Green, I. Jones, http://www.matter.org.uk/tem/, The University of Liverpool, 2000.

[133] M. Zinke-Allmang, Thin Solid Films 346/1 (1999) 1.

[134] H.A. Jehn, in: H.A. Jehn, W. Gissler (Eds.), Advanced Techniques for Surface Engineering, Kluwer Academic Publisher, Dortrecht, 1992, p. 5.

[135] J.E. Greene, in: D.T.J. Hurle (Ed.), Handbook of crystal growth, vol. 1, Elsevier Science Publisher, Amsterdam, 1993, p. 640.

[136] C.A. Neugebauer, in: L.I. Maissel, R. Glang (Eds.), Handbook of Thin Film Technology, McGraw-Hill, New York, 1983.

[137] J.A. Thornton, J. Vac. Sci. Technol. 11/4 (1974) 666.

[138] R. Messier, A.P. Giri, R.A. Roy, J. Vac. Sci. Technol., A 2/2 (1984) 500.

[139] B.A. Movchan, A.V. Demchishin, Phys. Met. Metallogr. 28/4 (1969) 83.

[140] P.B. Barna, M. Adamik, Thin Solid Films 317/1-2 (1998) 27.

[141] C.V. Thompson, Annual Review of Materials Science 30 (2000) 159.

[142] P.J. Kelly, R.D. Arnell, J. Vac. Sci. Technol., A 16/5 (1998) 2858.

[143] E. Mirica, G. Kowach, H. Du, Crystal Growth and Design 4/1 (2004) pp. 157.

[144] J.A. Thornton, J. Vac. Sci. Technol. 12/4 (1975) pp. 830.

[145] J.A. Thornton, J. Vac. Sci. Technol., A 4 (1986) 3059.

[146] H.T.G. Hentzell, C.R.M. Grovenor, D.A. Smith, J. Vac. Sci. Technol., A 2/2 (1984) 218.

[147] C.R.M. Grovenor, H.T.G. Hentzell, D.A. Smith, Acta Metallurgica 32/5 (1984) 773.

[148] P.B. Barna, M. Adamik, in: Y. Pauleau, P.B. Barna (Eds.), Proceedings of the NATO Advanced Research Workshop on Protective Coatings and Thin Films: Synthesis, Characterization and Applications, Kluwer Academic Publishers, Dordrecht, 1996, p. 279.

[149] G. Majni, C. Nobili, G. Ottaviani, M. Costato, E. Galli, J. Appl. Phys. 52/6 (1981).

[150] A. Kovács, P.B. Barna, J.L. Lábár, Thin Solid Films 433/Issues 1-2 (2003) 78.

[151] G. Radnoczi, P.B. Barna, Thin Solid Films 116/1-3 (1984) 143.

[152] A. Barna, P.B. Barna, G. Radnoczi, G. Safran, Ultramicroscopy 15/1-2 (1984) 101.

[153] Z. Radi, P.B. Barna, J.L. Lábár, J. Appl. Phys. 79/8 (1996).

[154] P. Firbas, E. Schmidt, Scripta Fac. Sci. Natur. Ujep Brunenses, Physica 1 8 (1978) 29.

[155] I. Iordanova, P.J. Kelly, R. Mirchev, V. Antonov, Vacuum 81/7 (2007) 830.

[156] J. Pelleg, L.Z. Zevin, S. Lungo, N. Croitoru, Thin Solid Films 197/1-2 (1991) 117.

[157] U.C. Oh, J.H. Je, J.Y. Lee, J. Mater. Res. 10/3 (1995) 634.

[158] L. Hultman, J.E. Sundgren, J.E. Greene, J. Appl. Phys. 66/2 (1989) 536.

[159] L. Hultman, W.D. Munz, J. Musil, S. Kadlec, I. Petrov, J.E. Greene, J. Vac. Sci. Technol., A 9/3 (1991) 434.

[160] G. Knuyt, C. Quaeyhaegens, J. D'Haen, L.M. Stals, Surf. Coat. Technol. 76-77/Part 1 (1995) 311.

[161] D. Gall, S. Kodambaka, M.A. Wall, I. Petrov, J.E. Greene, J. Appl. Phys. 93/11 (2003) 9086.

[162] J.P. Zhao, X. Wang, Z.Y. Chen, S.Q. Yang, T.S. Shi, X.H. Liu, J. Phys. D: Appl. Phys. 30/1 (1997) 5.

[163] V. Valvoda, J. Musil, Thin Solid Films 149/1 (1987) 49.

[164] A. Karimi, G. Allidi, R. Sanjines, Surf. Coat. Technol. 201/7 (2006) 4062.

[165] F. Mei, N. Shao, L. Wei, Y. Dong, G. Li, Appl. Phys. Lett. 87/1 (2005) 011906.

[166] M. Beckers, N. Schell, R.M.S. Martins, A. Mücklich, W. Möller, J. Vac. Sci. Technol., A 23/5 (2005) 1384.

[167] E.K.U. Gross, R.M. Dreizler (Eds.), Proceedings of a NATO Advanced Study Institute on Density functional theory, Plenum Press, New York, 1995.

[168] J. Kohanoff, Electronic Structure Calculations for Solids and Molecules: Theory and Computational Methodes, Cambridge University Press, Cambridge, 2006.

[169]   VASP, http://cms.mpi.univie.ac.at/vasp/.

[170]   SRIM, http://www.srim.org/ version 2006.

[171]   J.P. Biersack, L. Haggmark, Nucl. Instr. and Meth. 174 (1980) 257.

[172]   J.F. Ziegler, J.P. Biersack, U. Littmark, The Stopping and Range of Ions in Matter, Pergamon Press, New York, 1996.

[173]   G. Franz, Oberflächentechnologie mit Niederdruckplasmen - Beschichten und Strukturieren in der Mikrotechnik, Springer, Berlin, 1998.

[174]   P. Sigmund, Appl. Phys. Lett. 14/3 (1969) 114.

[175]   W.D. Westwood, Sputter Deposition, AVS, New York, 2003.

[176]   P. Haasen, Physikalische Metallkunde, Springer, Berlin, 1994.

[177]   P.H. Mayrhofer, C. Mitterer, L. Hultman, H. Clemens, Prog. Mat. Sci. 51/8 (2006) 1032.

[178]   D.M. Mattox, J. Vac. Sci. Technol., A 7/3 (1989) 1105.

[179]   W. Ensinger, Nucl. Instrum. Methods Phys. Res., Sect. B 127-128 (1998) 775.

[180]   G. Gottstein, Physikalische Grundlagen der Materialkunde, Springer, Berlin, 2001.

[181]   L.A. Donohue, J. Cawley, J.S. Brooks, W.D. Munz, Surf. Coat. Technol. 74-5/1-3 (1995) 123.

[182]   J. Vetter, E. Lugscheider, S.S. Guerreiro, Surf. Coat. Technol. 98/1-3 (1998) 1233.

[183]   K. Bobzin, E. Lugscheider, R. Nickel, P. Immich, Materialwissenschaft und Werkstofftechnik 37/10 (2006) 833.

[184]   G.S. Kim, S.Y. Lee, Surf. Coat. Technol. 201/7 (2006) 4361.

[185]   P.H. Mayrhofer, Materials Science of Hard Coatings - Lecture Notes (2007).

[186]   E. Arzt, Acta Materialia 46/16 (1998) 5611.

[187]   L. Lü, M.O. Lai, Mechanical Alloying, Springer, Berlin, 1998.

[188]   A.C. Fischer-Cripps, Nanoindentation, Springer Science + Business Media, New York, 2004.

[189]   T. Chudoba, in: A. Cavaleiro, J.T.M. De Hosson (Eds.), Nanostructured Coatings, Springer, New York, 2006.

[190]   G.M.P.W.C. Oliver, J. Mater. Res. 7 (1992) 1564.

[191]   M. Moser, P.H. Mayrhofer, Thin Solid Films (paper in final preparation).

[192]   J.D. Sunderkötter, W. Knabl, H.-P. Martinz, H. Clemens, M.F. Stroosnijder, in: Y.-W. Kim, D.M. Dimiduk, M.H. Loretto (Eds.), Gamma Titanium Aluminides - The Minerals, Metals & Materials Society, Warrandale, Pa, 1999, p. 769.

[193]   W. Beitz, K.H. Grote (Eds.), Dubbel - Taschenbuch für den Maschinenbau, Springer, Berlin, 1997.

[194]   W.D. Nix, Metall. Trans. A 20 A (1989) 2217.

[195]   P.H. Mayrhofer, C. Mitterer, Surf. Coat. Technol. 133-134 (2000) 131.

[196] J.D. Wilcock, D.S. Campbell, Thin Solid Films 3/1 (1969) 3.

[197] H. Ebert, Mechanisch Thermische Zustandsgrößen, Springer, Berlin, 1972.

[198] P.H. Mayrhofer, G. Tischler, C. Mitterer, Surf. Coat. Technol. 142-144 (2001) 78.

[199] P.H. Mayrhofer, F. Kunc, J. Musil, C. Mitterer, Thin Solid Films 415/1-2 (2002) 151.

[200] J.W. Cahn, Acta Metallurgica 9 (1961) 795.

[201] P.H. Mayrhofer, F.D. Fischer, H.J. Bohm, C. Mitterer, J.M. Schneider, Acta Materialia 55/4 (2007) 1441.

[202] N. Birks, G.H. Meier, Introduction to High Temperature Oxidation of Metals, Edward Arnold Ltd., London, 1983.

[203] M.P. Brady, B.A. Pint, P.F. Tortorelli, I.G. Wright, R.J. Hanrahan, in: M. Schütze (Ed.), Corrosion and Environmental Degradation, Wiley-VCH., Weinheim, 2000, p. 229.

[204] A. Rahmel, Aufbau von Oxidschichten auf Hochtemperaturwerkstoffen und ihre technische Bedeutung, Deutsche Gesellschaft für Metallkunde, Oberursel, 1982.

[205] H.J. Grabke, M. Schütze (Eds.), Oxidation of Intermetallics, Wiley-VCH GmbH, Weinheim, 1997.

[206] B.A. Pint, J.R. DiStefano, I.G. Wright, Materials Science and Engineering: A 415/1-2 (2006) 255.

[207] F. Rovere, P.H. Mayrhofer, J.M. Schneider, A. Reinholdt, J. Mayer, Surf. Coat. Technol. submitted (2008).

[208] G.W. Ehrensteiner, G. Riedel, P. Trawiel, Praxis der Thermischen Analyse von Kunststoffen, Carl Hanser Verlag, München, 1998.

[209] W.F. Hemminger, H.K. Cammenga, Methoden der Thermischen Analyse, Springer, Berlin, 1989.

[210] P.H. Mayrhofer, F. Rovere, M. Moser, C. Strondl, R. Tietema, Scripta Mater 57/3 (2007) 249.

10 Publications

Papers included in this thesis

I. *Microstructure and mechanical properties of sputtered intermetallic Al-Au coatings*,
<u>Moser M.</u>, Mayrhofer P. H., Ross I. M., Rainforth W. M.,
Journal of Applied Physics 102, 023523; 2007.

II. *Thermal stability of sputtered intermetallic Al-Au coatings*,
<u>Moser M.</u>, Mayrhofer P. H., Ross I. M., Rainforth W. M.,
Journal of Vacuum Science Technology A 25(5); 2007: 1402.

III. *Magnetron sputtered intermetallic Al-Au and Al-Zr-Y coatings for the oxidation protection of γ-TiAl*,
<u>Moser M.</u>, Mayrhofer P. H., Braun R.,
Materials Research Society Symposium Proceedings, vol. 980, 2007. p. 431.

IV. *Yttrium-induced structural changes in sputtered $Ti_{1-x}Al_xN$ thin films*,
<u>Moser M.</u> and Mayrhofer P. H.,
Scripta Materialia 2007; 57/4: 357.

V. *Influence of bipolar pulsed DC magnetron sputtering on chemical composition and micro-structure of TiAlYN thin films*,
<u>Moser M.</u>, Mayrhofer P. H., Székely L., Sáfrán G., Barna P. B.,
submitted to Surface and Coatings Technology.

VI. *On the influence of coating and oxidation on the mechanical properties of a γ-TiAl based alloy*,
<u>Moser M.</u>, Mayrhofer P. H., Clemens H.,
submitted to Intermetallics.

Publications related to this thesis

VII. *Thermally induced transitions of CrN thin films,*
Mayrhofer P. H., Rovere F., <u>Moser M.</u>, Strondl C., Tietema R.,
Scripta Materialia 2007; 57/3: 249.

VIII. *Oxidation Resistance and Ductility of a coated γ-TiAl based alloy,*
<u>Moser M.</u>, Mayrhofer P. H., Clemens H.,
Berg- und Hüttenmännisches Monatsheft (BHM), in press.

IX. *Oxidation behaviour of TiAlYN and CrAlYN nanocomposite coatings deposited on γ-TiAl based alloy Ti-45Al-8Nb,*
Braun R., Müßener D., <u>Moser M.</u>, Rovere F., Mayrhofer P. H., Leyens C.,
Structural Aluminides for elevated Temperature Application, The Minerals, Metals & Materials Society, 137th annual meeting proceedings, in press.

X. *Influence of oxidation protective coatings on the ductility of γ-TiAl based alloys,*
<u>Moser M.</u>, Mayrhofer P. H., Clemens H.,
Structural Aluminides for elevated Temperature Application, The Minerals, Metals & Materials Society, 137th annual meeting proceedings, in press.

XI. *Stratified columnar structure in Ti-Al-Y-N thin films,*
Sáfrán G., <u>Moser M.</u>, Mayrhofer P. H., Székely L., Geszti O., Barna P. B.,
paper in final preparation.

XII. *Structural characterisation of Al_2Au thin films deposited on γ-TiAl-8Nb: effects of extended oxidation,*
Ross I. M., <u>Moser M.</u>, Mayrhofer P. H., Braun, R., Rainforth W. M.,
paper in final preparation.

XIII. *Thermal stability and thermo-mechanical properties of $(Ti_{1-x}Al_x)_{1-y}Y_yN$ thin films,*
<u>Moser M.</u> and Mayrhofer P. H.,
paper in final preparation.

Supervised diploma theses

XIV. R. Rachbauer, *Microstructure and stability of Ti-Al-(Y, Nb)-N coatings,*
Montanuniversität Leoben, 2008.

XV. L. Hädicke, *Microstructural investigations of quaternary oxi-nitride thin films*,
Montanuniversität Leoben, 2008.

XVI. N. Fateh, *Microstructure, mechanical properties and oxidation resistance of
intermetallic Al-Zr-Y and nano-structured Al-Zr-Y-(O,N) coatings*,
Montanuniversität Leoben, 2008.

Publication I

Microstructure and mechanical properties of sputtered intermetallic Al-Au coatings

M. Moser, P. H. Mayrhofer, I. M. Ross, W. M. Rainforth

MICROSTRUCTURE AND MECHANICAL PROPERTIES OF SPUTTERED INTERMETALLIC AL-AU COATINGS

M. Moser[1], P. H. Mayrhofer[1], I. M. Ross[2], W. M. Rainforth[2]

[1]Department of Physical Metallurgy and Materials Testing, Montanuniversität Leoben, Franz-Josef-Strasse 18, A-8700 Leoben, Austria

[2]Department of Engineering Materials, University of Sheffield, Mappin Street, Sheffield S1 3JD, United Kingdom

Abstract

Intermetallic Al-based coatings such as Al-Ni, Al-Cr, and Al-Pt are widely used as bond coats and/or as oxidation protection of turbine blades. Investigations during earlier work indicated promising thermal stability and oxidation resistance of intermetallic Al_2Au based coatings. Hence, here we study in detail the microstructure and mechanical properties of unbalanced magnetron sputtered Al-Au films with Al/Au at% ratios of 1.85, 2.00, and 4.32. The film with an Al/Au ratio of 2.00 has a single-phase Al_2Au dense columnar structure in the as-deposited state and a hardness of ~8 GPa. With increasing Al and Au content the morphology changes into a more equiaxed structure with additional Al, AlAu and Au phases, respectively. During growth, excess Al of the film with an Al/Au ratio of 4.32 forms lamellar nano-segregations (~3 nm thick) in the Al_2Au domains. The simultaneous nucleation and growth of Al_2Au, AlAu, and Au phases in the coatings with an Al/Au ratio of 1.85, with their different growth mechanisms leads to the formation of pores having an average size of ~150 nm. These Al- and Au-rich films, compared to Al_2Au, have reduced hardnesses of ~4 and ~2 GPa, respectively, due to the additional soft metallic phases and pores present. Our results show that within the Al-Au system the single-phase intermetallic Al_2Au films exhibit the best structural and mechanical properties for protecting oxidation sensitive materials.

Key words: Al_2Au, Ab initio, HRTEM, protective coating

Introduction

The Al-Au system was already investigated as early as in the year 1890 by Roberts-Austen [1] describing the purple colored intermetallic Al_2Au phase and its high melting point. Al_2Au has a homogeneity range between 32.9 and 33.9 at% Au at room temperature and crystallizes in an fcc, CaF_2-type structure. The melting point of Al_2Au is ~1600°C according to the binary phase diagram [2,3].

This intermetallic compound is known to the microelectronics community as the source of the so called "purple-plague" [4], as it forms when gold wires are bonded to aluminium surfaces or vice versa and often leads to mechanical failure due to its intrinsic brittleness and Kirkendall voids forming from uneven diffusion rates of Au and Al [5,6]. However, bulk Al_2Au is reported to be fairly resistant against oxidation [6,7].

In an earlier paper about the optical and tribological properties of Al_2Au-based films to serve as colored low-friction top-coats on coated cutting tools we demonstrated that coatings from the Al-Au system can be produced by unbalanced magnetron sputtering [8].

Here we investigate the structural and mechanical properties of single-phase Al_2Au coatings with respect to films having higher Al and Au contents to develop the structural evolution and to obtain the mechanical properties like hardness, elastic modulus, and qualitative fracture toughness.

Experimental Details

Coatings with different Al/Au at% ratios are deposited on Si(100), Sapphire, and low alloyed steel substrates in a magnetically unbalanced magnetron sputtering system using an Al target (99.999% purity, ∅150 mm x 6 mm) and varying amounts of Au inlets (∅10 mm, 2 mm thick) on the target race track in an Ar (99.999%) glow discharge. In all deposition runs substrates are placed parallel to the target at a distance of 8 cm, the substrate temperature was 300 °C, the bias voltage was -85 V, and the sputter power density was 2.7 W/cm^2. The base pressure in the system was 2 mPa and the working gas pressure was set to 0.6 Pa. The metallographically ground and polished substrates are ultrasonically cleaned with acetone and ethylene, and are ion-etched within the chamber prior to deposition using an Ar pressure of 0.8 Pa and applying -1250 V. Depending on the

individual investigations the deposition time was in the range of 30 to 120 minutes yielding coating thicknesses between 2.5 and 8 μm.

Ab initio calculations of Al_2Au are based on the density-functional theory, using the VASP code [9,10] in conjunction with the generalized-gradient approximations projector augmented wave potentials [11]. Relaxation convergence of 1.0 meV for ions and 0.1 meV for electrons, reciprocal-space integration with a Monkhorst-Pack scheme [12], energy cutoff of 500 eV, and tetrahedron method with Blöchl corrections [13] for the energy were used in the calculations. The volumes, total energies, and bulk moduli at equilibrium were obtained by a least-square fit of the calculated total energy over volume curves employing the Birch-Murnaghan's equation of state [14]. A k-points grid of 5x5x5 is used for all calculations of the supercell built by 12 atoms.

The microstructure of the different films was investigated using a Siemens D500 Bragg-Brentano X-ray diffractometer with Cu-Kα radiation in the 2θ range 20—70 deg. Coating morphology was examined using scanning electron microscopy (SEM; ZEISS EVO 50) and transmission electron microscopy (TEM; JEOL 2010F, equipped with Oxford Instruments energy dispersive spectrometry) and a scanning transmission electron microscopy (STEM) unit. The chemical composition of the films was determined by energy dispersive X-ray analysis (EDX; Oxford Instruments INCA) during SEM investigations. Quantification was performed relative to an internal standard single-phase intermetallic Al_2Au film which exhibited no additional phases after annealing in vacuum up to 700 °C during XRD.

Mechanical properties, such as hardness of indention (HIT) and modules of indentation (EIT) are determined from unloading segments of load-displacement curves during computer controlled indentation tests using a Fischerscope H100 and a maximum load of 35 mN. The presented values are averaged from a minimum of 20 indents. A load of 800 mN was used to investigate the crack formation of the films coated on Si substrates and thereby estimate qualitatively their fracture toughness.

Results and Discussion

The coatings prepared have Al/Au at% ratios of 1.85, 2.00, and 4.32 when 10.5%, 8.8%, and 5.9% of the total target surface area are covered by Au, respectively. Both the oxygen

and nitrogen content in the films are below the detection limit and error of ~1 at% of the used EDX equipment. The predominate phase in our films is intermetallic Al_2Au which crystallizes in the cubic CaF_2-structure in which Al is located in the tetrahedral sites of an fcc unit cell formed by Au-atoms (see Fig. 1a). In 1935 Dehlinger proposed that Al_2Au belongs to the group of intermetallic salt-like Zintl-Phases with the Al-atoms acting as anionic components by building a metallic sublattice which occupies the valence electrons from the Au-atoms acting as cations [15]. Thus, a continuous transition between a fully metallic and an entirely heteropolar electron density distribution is achieved in Al_2Au. *Ab initio* calculated electron-density distributions in Al_2Au lattice planes confirm these suggestions, see Fig. 1b. Between the Al atoms a typical metallic electron density distribution is present where valence electrons are delocalized in a nearly free uniform electron gas, as shown for the Al - (100) plane. The Au-atoms on the other hand show a mixture of an ionic and covalent binding character with semi-localized electrons gathering between the Au atoms, see the Au - (100) plane, where no free electrons are present. The Al, Au - (110) plane shows a mixture of metallic, covalent, and ionic bindings. The *ab initio* obtained bulk modulus, lattice parameter, and energy of formation for Al_2Au is 105 GPa, 6.067 Å, and -0.459 eV/at (corresponding to -132.9 kJ/mol).
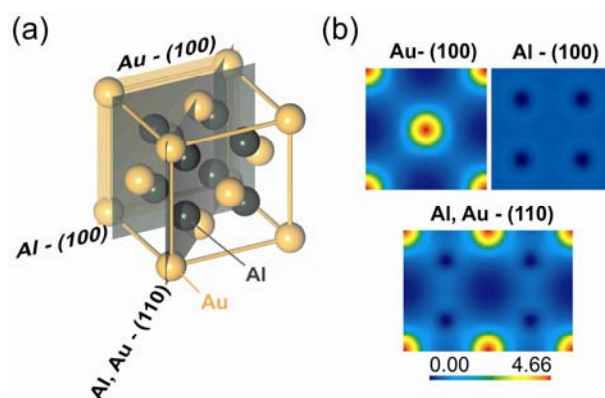
Fig.1 (a) Schematic of the CaF_2-structure of Al_2Au indicating the Au – (100), Al – (100) and Al + Au – (110) crystallographic planes for the (b) ab initio calculated electron-density distribution.

X-ray diffraction patterns at room temperature of our Al-Au films with the three different chemical compositions are presented in Fig. 2. The main three phases detectable in the coating with an Al/Au ratio of 1.85 are Al_2Au, AlAu, and Au. Average domain sizes and lattice parameters of the Al_2Au and Au phases are ~400 and 170 nm, and 5.986 and 4.062 Å, respectively, obtained by Rietveld refinement line profile analyses. The lattice

parameter and averaged domain sizes could not be determined for AlAu due to their low intensity reflexes. For the coating with an Al/Au ratio of 2.00 only the intermetallic Al_2Au phase can be detected revealing a preferred (311) orientation (Fig. 2), an average domain size of 230 nm and a lattice parameter of 5.978 Å. The reported lattice parameter for Al_2Au is 5.997 Å [16]. The Young's modulus, estimated from the *ab initio* calculated bulk modulus, using a Poisson ratio of 0.25±0.05, is 158±31.7 GPa.
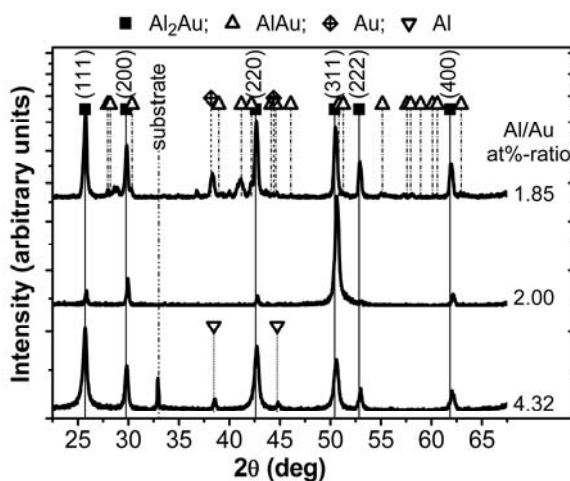
Fig.2 XRD patterns of our Al-Au coatings with Al/Au at% ratios of 1.85, 2.00, and 4.32 on Si(100).

For an Al/Au ratio of 4.32 the main crystalline phases are Al_2Au and Al, with an average feature size and lattice parameters of 1100 and 75 nm, and 5.972 and 4.033 Å, respectively. In both, the Al- and the Au-rich coatings compared to Al_2Au, the Al_2Au phase has no preferred orientation.

SEM fracture cross sections (Fig. 3) of our films show considerable differences in their morphology as a function of the Al/Au ratio. The coating with an Al/Au ratio of 1.85 has a rough, almost equiaxed, and porous structure with a thickness of ~4 µm after 30 min deposition (Fig. 3a). Using optical profilometer measurements the surface arithmetic mean roughness Ra is ~350 nm. The color of this film is violet in agreement to the color measurements presented in Ref. 8. The single-phased intermetallic Al_2Au coating (Al/Au=2.00, Fig. 3b) presents a dense columnar structure with a surface roughness Ra of ~20 nm, a shiny violet color and a thickness of ~3 µm after 30 min deposition. For the coating with an Al/Au at% ratio of 4.32 the structure exhibits an arrangement of platelets (see Fig. 3c). These films have a surface roughness Ra of ~200 nm, a pink colored appearance, and have a thickness of ~4 µm after 30 min deposition.
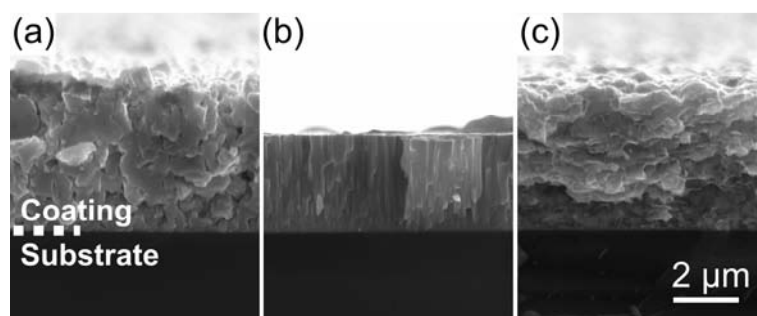
Fig.3 SEM fracture cross sections of our films with an Al/Au at% ratio of 1.85 (a), 2.00 (b), and 4.32 (c).

Annular dark-field (ADF) STEM cross section investigations of the film with an Al/Au ratio of 1.85 (Fig. 4a) in combination with the SAED analyses (Fig. 4b) allowed the identification of a porous ternary phase structure composed of Al_2Au, AlAu, and Au, as obtained by XRD analyses (Fig. 2). The globular pores with average diameters around 150 nm appear black in Fig. 4a and bright in the bright-field TEM image Fig. 4c. Our results suggest that differences in the nucleation and growth modes (e.g. layered vs. island growth) between intermetallic and metallic phases as well as their different growth rates lead to the formation of a porous structure [17,18].
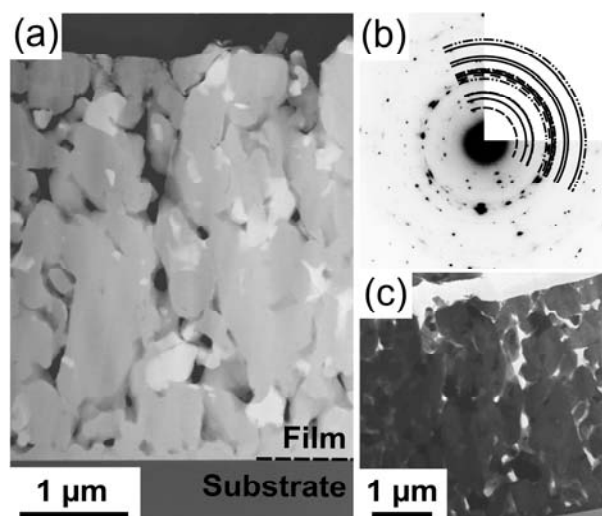
Fig.4 (a) Annular dark-field STEM cross section of a coating with an Al/Au ratio of 1.85. (b) SAED with JCPDS standard diffraction rings for Au (dash-dotted), AlAu (dashed), and Al2Au (solid) [16]. (c) Plan view TEM cross section.

The bright-field TEM cross section image of the intermetallic Al_2Au film (Fig. 5a) presents a dense columnar structure with column diameters of ~215 nm at the surface and ~15 nm close to the substrate interface. This structure evolves from competitive growth of random nucleation sites at the substrate to a preferred (311) directional growth at larger coating thicknesses. High resolution imaging of the columnar grain boundaries showed no

evidence of grain boundary phase or voiding and Fig. 5a suggests a relatively low density of dislocations and grain boundaries.
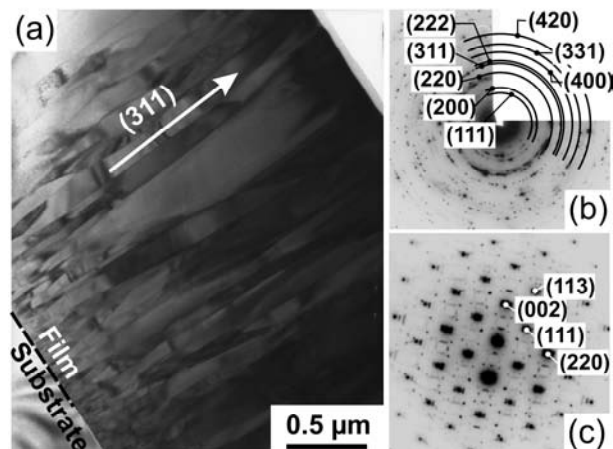
Fig.5 (a) Bright-field TEM cross sectional image of the film with an Al/Au ratio of 2.00. (b) SAED with indexed JCPDS standard diffraction rings for Al_2Au,[16] and (c) Distinct crystalline pattern from a single columnar grain aligned to an Al_2Au [110] zone axis illustrating the preferred (311) growth direction.

The (311) textured single-phased Al_2Au structure revealed by XRD was also confirmed by SAED analyses of the coating cross-section (Fig. 5b). Fig. 5c shows a distinct crystalline pattern from a single columnar grain aligned near to an Al_2Au [110] zone axis illustrating the preferred (311) growth direction. Additional minor diffraction spots were observed superimposed on the single crystal Al_2Au pattern shown in Fig. 5c. These spots are indicative of the presence of an ordered defect sublattice within an individual grain, not necessarily observable in the bulk XRD analysis, resulting from slight deviations from the Al_2Au structure shown in Fig. 1a. We obtained (311) preferred orientation of Al_2Au films on various substrates such as low-alloyed steel, Ni-base alloy, γ-TiAl alloy (Ti-45Al-8Nb), and silicon (100). Only when $(11\bar{2}0)$ Sapphire substrates are used the intensities of the (100) and the (311) reflexes were almost equal. The joint committee of powder diffraction standard (JCPDS) pattern of Al_2Au (No. 17-877) also gives the (311) orientation with the highest intensity [16]. There, the most dominant peaks are the (111), (220), and (311) with an intensity ratio of 0.90:0.95:1.00, respectively. This ratio is only 0.02:0.01:1.00 in our textured single-phase Al_2Au films.

The ADF STEM cross section image of the film with an Al/Au ratio of 4.32, Fig. 6a, indicates a binary phase structure (brighter contrast representing higher average atomic number) in a platelet-like dense arrangement (Fig. 6c). Using SAED analyses (Fig. 6b) the phases were identified to be Al (dark areas) and Al_2Au (bright areas) in agreement to the

above presented XRD results (Fig. 2). No pores were detected in the TEM analyses, as shown in the bright-field image. High magnification dark-field STEM images of this coating are presented in Fig. 7, revealing that Al forms layered segregations with a thickness of ~3 nm within the Al_2Au domains (Fig. 7b). Firbas and Schmidt found that the diffusion process in the intermetallic phase of Al-Au thin film couples is governed by an interstitial diffusion mechanism which could explain the Al segregation within Al_2Au [19]. Ref. 20 and 21 report that Al_2Au forms primarily when Au is evaporated on Al (111) surfaces and Ref. 22 states Al_2Au with a heat of formation of -10.1±0.5 kcal/(g at.) compared to -9.2±0.5 and -8.3±0.5 kcal/(g at.) for AlAu and $AlAu_2$, respectively.
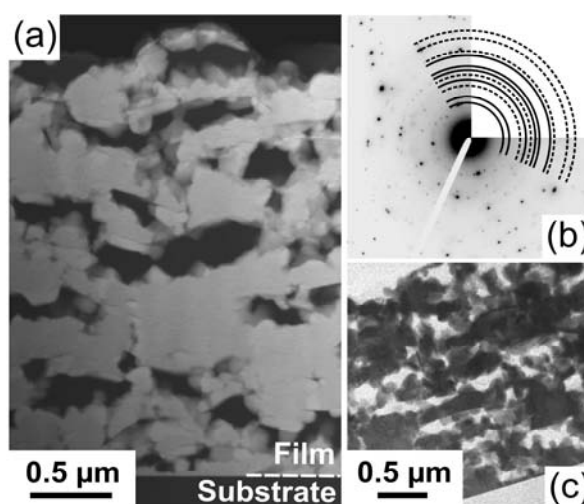
Fig.6 (a) Annular dark-field-STEM cross section of the coating with an Al/Au ratio of 4.32. (b) SAED with JCPDS standard diffraction rings for Al (dashed), and Al_2Au (solid) [16]. (c) Plan view TEM cross section.

As heat of formation of the various species and thermal activation strongly influence the coating microstructure [23, 24], the primary phase formed in our films is intermetallic Al_2Au with respect to the other phases. For the coatings with an Al/Au ratio above 2 excess Al forms metallic Al domains, the only phase possible according to the Al rich part of the phase diagram. In films with an Al/Au ratio below 2 on the other hand Al_2Au and AlAu form according to their heat of formation and peritectic reaction [2], and metastabel metallic Au forms due to the limited atomic assembly kinetics given in plasma-assisted vapour deposition processes [25,26].

The averaged indentation hardness HIT and indentation modulus EIT as a function of the Al/Au at% ratio are presented in Fig. 8. Single-phase intermetallic Al_2Au films (Al/Au=2.00) have values for HIT of 7.9±1.2 GPa and EIT of 144±9.03 GPa. This
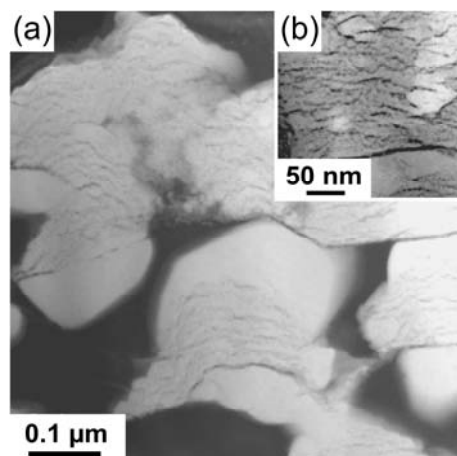
Fig.7 (a) Annular dark-field cross sectional STEM image of the Al_2Au areas (bright) with Al nanosegregations (dark) in the coating with an Al/Au ratio of 4.32 (Fig. 6). (b) The small insert is a higher magnification dark field-STEM of the segregations in Al_2Au.

experimentally obtained indentation modulus is in good agreement to the Young's modulus of 158±31.7 GPa, estimated from *ab initio* calculated bulk modulus. Both hardness and modulus decrease with increasing Al and Au content from the Al_2Au film. The films with Al/Au at% ratios of 4.32 and 1.85 reveal values for HIT of 3.2±0.7 and 1.7±0.4 GPa, and for EIT of 104±13.4 and 72±8.5 GPa, respectively. This reduction is a direct result of the contributions from soft metallic compounds present in the coatings and, additionally, the differences in microstructure as compared to the Al_2Au film –i.e. coarse grained versus columnar– as well as the pores present in the Au rich coating.
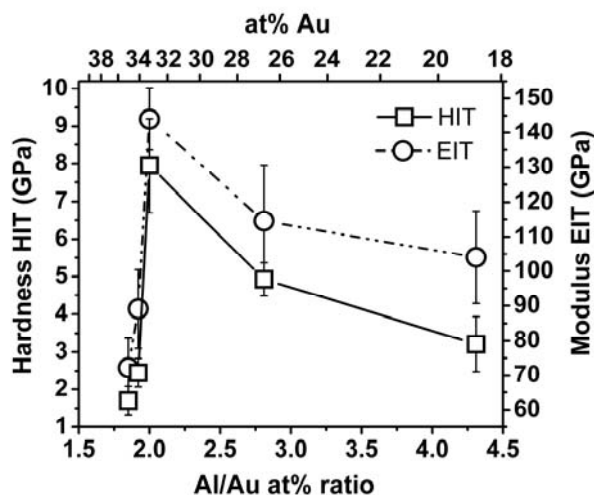
Fig.8 Hardness and indentation modulus of our Al-Au coatings as a function of the Al/Au at% ratio.

To qualitatively estimate the toughness of our films as a function of their Al/Au ratio, the average crack sizes on the coating surface obtained by Vickers indentation with 800 mN on Si(100) substrates, are determined (Fig. 9a). A micrograph presenting a typical crack

pattern for Al_2Au is shown in Fig. 9b. In all our coatings cracks were found to grow radially from the corners of the indent. This radial cracking pattern is generally found when brittle material is tested at hard substrates. Circular cracks, however, as they are well known from hard ceramic coatings, often appear due to the influence of a softer substrate [27-29].
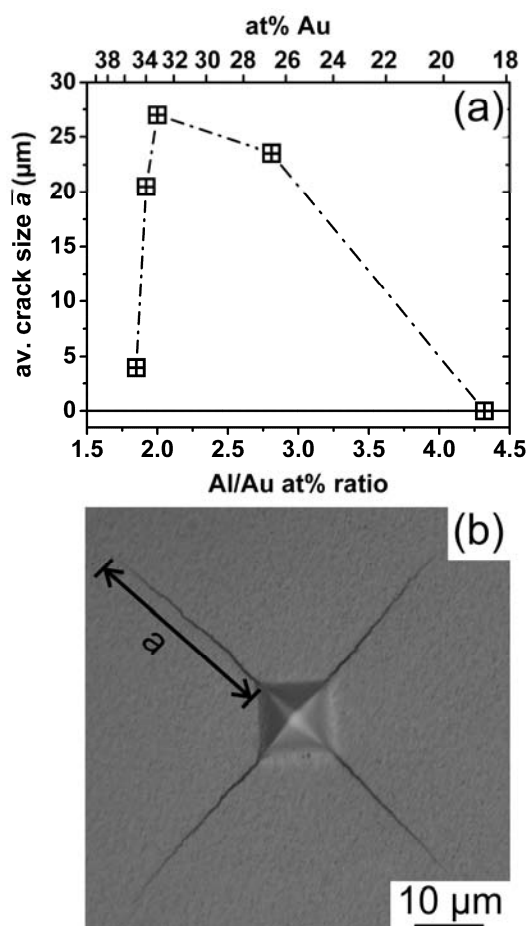
Fig.9 (a) Averaged crack size ā as a function of the Al/Au at% ratio after indentation with 800 mN. (b) Typical crack pattern of the Al_2Au film.

The average crack length ā rapidly increases from 4 to 27 µm by increasing the Al/Au ratio from 1.85 to 2.00, see Fig. 9a. Further increasing the Al/Au ratio i.e. decreasing at% Au in the coatings leads again to decreasing crack sizes and for the coating with an Al/Au ratio of 4.32 no cracks can be identified or they are smaller than the surface roughness of this film. These observations are in agreement with the hardness measurements as well as with structural and morphological investigations showing that the single-phase Al_2Au film, which has the longest crack lengths –hence lowest resistance against plastic deformation– has also the highest hardness and densest structure with neither voids nor soft metallic phases.

Conclusions

Al-Au films, grown by magnetically unbalanced magnetron sputtering from Al targets with Au inlets, with an Al/Au at% ratio between 1.85 and 4.32 exhibit strong differences in their microstructure and hence mechanical properties although their dominating phase is always Al_2Au. The latter is shown by *ab inito* calculation to have the characteristics of a Zintl phase. Single-phase intermetallic Al_2Au films grow with a dense, columnar microstructure and preferred (311) orientation. They have the highest hardness and Young's modulus but lowest resistance against plastic deformation compared to coatings with higher Al or Au contents. Films with an Al/Au at% ratio of 4.32 grow in a platelet-like dense binary microstructure with nanosegregations of Al found within the Al_2Au domains. On the other hand the simultaneous nucleation and growth of Al_2Au, AlAu, and Au phases in coatings with an Al/Au ratio of 1.85, with their different growth mechanisms leads to an open, coarse grained microstructure and the formation of ~150 nm pores.

Based on our results we can conclude that the single-phase intermetallic Al_2Au film exhibits superior structural and mechanical properties compared to coatings having higher Al and Au contents and consequently has the most promising properties within the investigated Al-Au films to protect sensitive materials.

Acknowledgements

References

[1]   W.C. Roberts-Austen, Proc. Roy. Soc. 41, 347 (1891).

[2]   H. Okamoto, J. Phase Equil., 12, 114 (1991).

[3]   M. Li, C. Li, F. Wang, D. Luo, and W. Zhang, J. Alloys. Com. 385, 199 (2004).

[4]   C. W. Horsting, 10th IEEE Annual Meeting, Proceeding, Reliability Physics 155 (1972).

[5]   R. W. Cahn, Nature 396, 523 (1998).

[6]   C. Xu, C. D. Breach, T. Sritharan, F. Wulff, and S. G Mhaisalkar, Thin Solid Films 462, 357 (2004).

[7]   H. C. Shih, Z. Metallkde, 71, 577 (1980).

[8]   C. Mitterer, H. Lenhart, P. H. Mayrhofer, and M. Kathrein, Intermetallics 12, 579 (2004).

[9]   G. Kresse and J. Hafner, Phys. Rev. B, 48, 13115 (1993).

[10]   G. Kresse and J. Hafner, Phys. Rev. B, 49, 14251 (1994).

[11]   G. Kresse and J. Joubert, Phys. Rev. B, 59, 1758 (1999).

[12]   H. J. Monkhorst and J. D. Pack, Phys. Rev. B, 13, 5188 (1976).

[13]   P. E. Blöchl, Phys. Rev. B 50, 17953 (1994).

[14]   F. Birch, J. Geophys. Res. 83, 1257 (1978).

[15]   U. Dehlinger, Ztschr. Elektochem. 41, 344 (1935).

[16]   Joint committee of powder diffraction standard (JCPDS) card N° 17-877 (Al2Au), 30-0019 (AlAu), 26-1006 (AlAu2), 4-784 (Au) and 4-787 (Al).

[17]   H. A. Jehn, in W. Gissler, H. A. Jehn (Eds.), Handbook of Thin Film (McGraw-Hill, New York, 1983).

[18]   D. L. Smith, Thin-Film Deposition – Principles & Practice (McGraw-Hill, New York, 1995).

[19]   P. Firbas and E. Schmidt, Scripta Fac. Sci. Natur. Ujep Brunensis, Physica 1, 8, 29 (1978).

[20]   G. Radnoczi and P. B. Barna, Thin Solid Fims, 116, 143(1984).

[21]   A. Barna, P. B. Barna, G. Radnoczi, and G. Safran, Ultramicroscopy 15, 101 (1984).

[22]   G. Majni, C. Nobili, G. Ottaviani, and M. Costato, J. Appl. Phys., 52, 4047 (1981).

[23]   J. A. Thornton, J. Vac. Sci. Technol. 11, 666 (1974).

[24]   R. W. Bené and R. M. Walser, J Vac Sci Technol 14, 925 (1977).

[25]   R. F. Bunshah, Handbook of Deposition Technologies for films and coatings (Noyes publications, 1994).

[26]   L. I. Maissel, in L. I. Maissel (Ed.), Handbook of thin film (McGraw-Hill, New York, 1983).

[27]   R. Wiedemann, T. Schultz-Kroenert, and H. Oettel, Prakt. Metallogr. 34, 497 (1997).

[28]   A. Roman, D. Chicot, J. Lesage, Surf. Coat. Tech. 155, 161 (2002).

[29]   M. M. Lima, C. Godoy, J. C. Avelar-Batista, P. J. Modenesi, Mat. Sci. Eng. A 357, 337 (2003).

Publication II

Thermal stability of sputtered intermetallic Al-Au coatings

M. Moser, P. H. Mayrhofer, I. M. Ross, W. M. Rainforth

Thermal stability of Sputtered Intermetallic Al-Au Coatings

M. Moser[1], P. H. Mayrhofer[1], I. M. Ross[2], W. M. Rainforth[2]

[1]*Department of Physical Metallurgy and Materials Testing, Montanuniversität Leoben, Franz-Josef-Strasse 18, A-8700 Leoben, Austria*

[2]*Department of Engineering Materials, University of Sheffield, Mappin Street, Sheffield S1 3JD, United Kingdom*

Abstract

Recently we have shown that single-phase Al_2Au coatings, prepared by unbalanced magnetron sputtering, exhibit a dense columnar structure and highest hardness and indentation modulus of 8 and 144 GPa, respectively, within the Al-Au films investigated.

This study focuses on the thermal stability of Al_2Au with respect to films containing more Al and Au having Al/Au at% ratios of 4.32 and 1.85, respectively. Single-phase Al_2Au has the highest onset temperature for recovery of 475 °C and recrystallization of 575 °C. Upon annealing Au- and Al-rich films, their stresses deviate from the linear thermo-elastic behavior at temperatures (T) above 200 and 450 °C, respectively, due to pores and metallic phases present. Metastable Au within the as-deposited Au-rich film is consumed by the growing intermetallic AlAu and $AlAu_2$ phases at $T \geq 450$ °C, which themselves melt at ~625 °C. Due to nm scale segregations of Al, encapsulated by Al_2Au in Al-rich coatings, their melting point is reduced by ~85 °C to 575 °C. Dynamic thermal analyses up to 1100 °C in synthetic air reveal the single-phase Al_2Au films with a superior thermal stability and only negligible oxidation. At 750 °C the mass gain is ~1.5mg/cm^2 after 50 h isothermal exposure.

Based on our investigations we can conclude that single-phase intermetallic Al_2Au films have a high potential for oxidation protection of sensitive materials.

Key words: thermal stability, DSC, TGA, high temperature XRD

Introduction

Intermetallic Al-based coatings such as Al-Ni, Al-Cr, and Al-Pt have proven to enhance the corrosion and oxidation resistance of Ni-base alloys and are thus widely used in turbine blade protection applications [1, 2].

Bulk Al_2Au is reported to be fairly resistant against oxidation [3, 4] and single-phases Al_2Au films have been proven to exhibit the densest and most uniform microstructure and highest hardness among Al_2Au base films containing higher amounts of Al and Au [5]. Details on the structural and mechanical evolution within the Al-Au system can be found in Ref. 5.

Thermo-gravimetric analyses of Al_2Au base coatings indicated increasing oxidation resistance with Al/Au ratios decreasing from 3.2 over 2.6 to 2.1 [6]. Based on these results it was suggested that best oxidation resistance can be obtained for single-phase intermetallic Al_2Au films.

Consequently, this study focuses on the thermal properties of single-phase Al_2Au coatings to assess their ability as oxidation and corrosion protective films for applications in energy-, automotive- or aerospace industry. We compare the different results with coatings having higher Al and Au contents than the single-phase Al_2Au films. This allows us to draw conclusions on the major influences on the thermal properties of Al_2Au base coatings.

Experimental Details

Coatings with different Al/Au at % ratios are deposited on Si(100), Sapphire, and low alloy steel substrates in a magnetically unbalanced magnetron sputtering system [7] using an Al target (99.999% purity, $\varnothing$150 mm x 6 mm) with varying amounts of Au inlets ($\varnothing$10 mm, 2 mm thick) on the target race track in an Ar (99.999%) glow discharge. In all deposition runs the substrates are placed parallel to the target at a distance of 8 cm, the substrate temperature was 300 °C, the bias voltage was -85 V, and the sputter power density was 2.7 W/cm^2. The base pressure in the system was $2x10^{-3}$ Pa and the working gas pressure was set to 0.6 Pa. The metallographically ground and polished substrates are ultrasonically cleaned with acetone and ethylene and are prior to deposition ion-etched within the deposition chamber using a voltage of 1250 V in an Ar pressure of 0.8 Pa. Depending on

the investigations foreseen the deposition time was set between 30 and 120 minutes yielding coating thicknesses between 2.5 and 8 µm for the different coatings.

Biaxial stresses σ of the films during in-situ vacuum annealing up to 700 °C (BSTM, biaxial stress temperature measurement) with a heating and cooling rate of 5 K/min are calculated as described in Refs. [8] and [9] from the measured curvature of coated Si(100) substrates (20x7x0.350 mm) using the modified Stony equation in accordance to the conditions summarized in Ref. [10].

The microstructural changes of the films on silicon substrates during exposure to synthetic air (mixture of 80% N_2 and 20% O_2) were investigated with high-temperature X-ray diffraction (HT-XRD; Bruker AXS D8 Advance with XRK900 heating chamber) with CuKα-radiation measurements up to a temperature of 900 °C. Patterns in the 2θ range of 35 to 55 deg were recorded during isothermal segments at 30, 200, 300, 400, and every 50 °C further to 900 °C. During cooling, patterns were recorded at 700, 500, and 30 °C. The heating and cooling rate was 3 K/min.

Differential scanning calorimetry (DSC) with simultaneous thermo-gravimetric analyses (TGA) was performed in a Netsch-STA 409C to characterize the oxidation behavior of the coatings by thermal ramping from 450 to 1150 °C at 20 K/min in synthetic air. These analyses were conducted on film material after chemical removal with 14M HNO_3 from their low alloy steel substrates to avoid interference with substrate material. The weight gain of single-phase intermetallic Al_2Au on Sapphire was additionally investigated by an isothermal test at 750 °C for 50 hours in synthetic air. Prior to and after DSC as well as BSTM measurements the coatings were investigated by X-ray diffraction (XRD; Siemens D 500, CuKα-radiation). Transmission electron microscopy (TEM; JEOL 2010F) was performed on the as-deposited films and film compositions were determined by energy dispersive X-ray analysis (Oxford Instruments INCA) in a scanning electron microscope (SEM; ZEISS EVO 50).

Results and Discussion

The Al/Au at% ratios of our films are 1.85, 2.00, and 4.32 obtained from energy dispersive X-ray analysis. X-ray diffraction patterns in the as-deposited state at room temperature (Fig. 1) reveal a ternary phase structure composed of metastable Au, AlAu, and Al_2Au, a

single-phase Al_2Au structure, and a binary structure composed of Al and Al_2Au for the coatings having Al/Au ratios of 1.85, 2.00, and 4.32, respectively. As we describe in detail in Ref. 5 limited atomic assembly kinetics as well as heat of formation and thermal activation of the various phase species strongly influence these coatings' microstructure. Thus, the ternary coating (Al/Au = 1.85) is shown in Fig. 2a with a coarse grained, porous (bright areas) structure of Al_2Au, with Au (darkest areas) and AlAu phases. The single-phase Al_2Au coating presents a dense, columnar microstructure (Fig. 2b), whereas the binary coating (Al/Au = 4.32) exhibits again a coarse grained but layered structure of Al_2Au with nanosegregation of Al –described in further detail in Ref. 5– and metallic Al phases (bright areas - Fig. 2c).
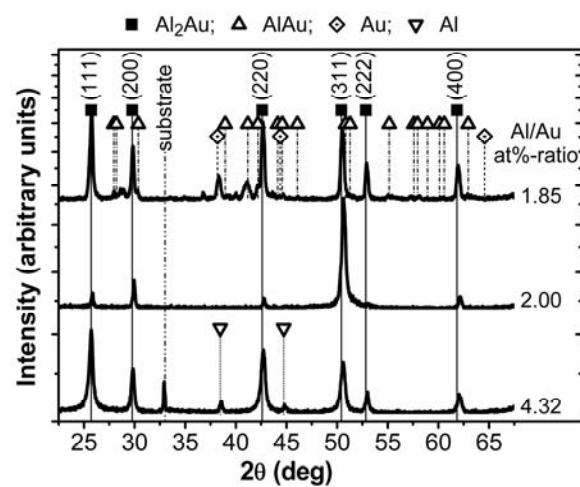
Fig.1 XRD pattern of the as-deposited Al-Au coatings with Al/Au at% ratios of 1.85, 2.00, and 4.32 on Si(100) [5].

Biaxial stresses of our films in-situ measured during vacuum annealing up to 700 °C are presented in Fig. 3. In the as-deposited state the coatings have tensile stresses of 0.18, 0.30, and 0.43 GPa for Al/Au = 1.85, 2.00, and 4.32, respectively. Heating the film-substrate composites leads to a reduction of tensile stresses of all Al_2Au base coatings indicating that their coefficient of thermal expansion α is larger than that of the silicon substrate ($\alpha_{Si}=3.55 \times 10^{-6}$ K^{-1}) [11]. During heating and cooling, the film – substrate composites follow the linear thermo-elastic behavior for temperatures where no recovery, recrystallization or plastic deformation takes place [12, 13]. The coating with an Al/Au ratio of 1.85, which is shown in Figs. 1 and 2a to be porous and composed of Al_2Au, AlAu, and Au phases as well as the single-phase intermetallic Al_2Au with its dense columnar structure (Fig. 2b) show almost no stresses at the deposition temperature of 300 °C (Fig. 3). These results suggest that our films grow relatively stress free. On the other hand the

film with an Al/Au ratio of 4.32, which is composed of Al_2Au and Al phases (Fig. 1), grows with tensile stresses of ~0.15 GPa.
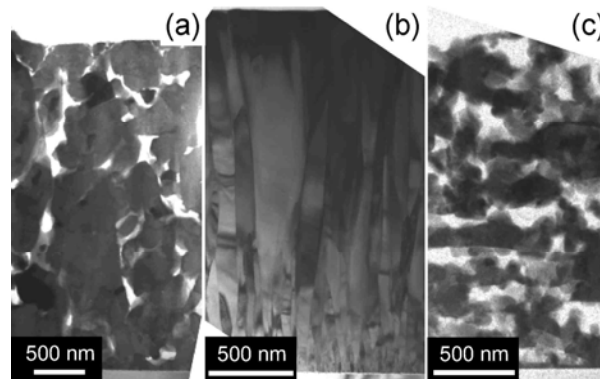
Fig.2 Bright-field TEM cross sections of the as-deposited coatings with Al/Au at% ratios of 1.85 (a), 2.00 (b), and 4.32 (c).

In the film with an Al/Au ratio of 1.85 no compressive stresses can build up during annealing up to 700 °C due to the porous structure and the soft metallic Au phase present (cf. Fig. 1 and 2a). The formation of tensile stresses during cooling down indicates that the structure of the film is denser after the temperature excursion to 700 °C and hence can build up tensile stresses during cooling. The linear thermo-elastic behavior of the single-phase Al_2Au film ranges from 25 to 475 °C, well beyond the deposition temperature. The almost same slopes of heating and cooling indicate that this coating had a low density of defects in the as deposited state, as it was suggested by SEM and TEM analyses [5]. Above 575 °C –i.e. 0.65 of the homologues temperature for Al_2Au (T_m = 1060 °C) – recrystallization processes set in and lead to a reduction of thermally induced compressive stresses.

The film with an Al/Au ratio of 4.32 follows the linear thermo-elastic line during heating to temperatures close to the deposition temperature (300 °C). Our measurements indicate that also above 300 °C there is a linear behavior up to 460 °C, where stresses become zero, but in this temperature range also recovery of structural defects [8] and microplasticity of the soft metallic phases are likely to contribute to the reduction of tensile stresses [14, 15]. At T > 460 °C the soft Al phase with its low melting point of 660 °C is plastically deformed resulting in the stagnation of the stress/temperature trace at zero.

Upon cooling, the coatings with Al/Au at% ratios of 2.00 and 4.32 show a deviation from the linear thermo-elastic behavior for temperatures below ~200 °C where their tensile

stresses increase to ~0.50 and 0.55 GPa, respectively. This deviation is due to the formation of tensile cracks.
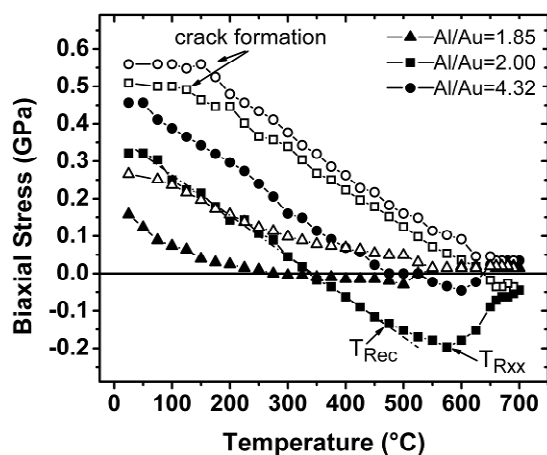
Fig.3 BSTM cycles of three Al-Au coatings with Al/Au at% ratios of 1.85, 2.00, and 4.32 coated on Si(100) (onset temperature of recovery, T_{Rec}, and recrystallization, T_{Rxx}). The heating step is indicated by solid symbols, cooling by the open symbols.

From the linear part of the cooling segments it is possible to obtain the thermal expansion coefficients α of the annealed films. Thus, α values determined for the films with and Al/Au at% ratio of 2.00 and 4.32 are 11.7×10^{-6} and 11.0×10^{-6} K^{-1}, respectively. No α value could be estimated for the film with an Al/Au ratio of 1.85 due to the early deviation from the thermo-elastic behavior.

Structural investigations by XRD of the film with an Al/Au ratio of 1.85 after the stress-temperature measurement in vacuum to 700 °C –i.e., 0.75 of the homologues temperature of Al$_2$Au– reveals that the metastabile Au phase present in the as-deposited state can no longer be detected, whereas the intensities for the AlAu and AlAu$_2$ reflexes increase, see Fig. 4. These results suggest that the AlAu and AlAu$_2$ phases grow at the expense of Au according to the equilibrium phase diagram [16]. Thus, the coating approaches a more stable configuration during annealing.

The films with an Al/Au ratio of 2.00 and 4.32 show no detectable changes in their XRD patterns between as-deposited state and after the vacuum annealing to 700 °C due to the BSTM investigations.

The structural evolution of our films with temperature is further and more detailed investigated by HT-XRD in synthetic air. Fig. 5 presents HT-XRD maps, where the scattering angle 2θ and the temperature are plotted on the x and y axis, respectively, and

the peak intensities are given by a color code. All samples are heated up to 900 °C and XRD patterns are recorded isothermally at the temperatures given in the graph.
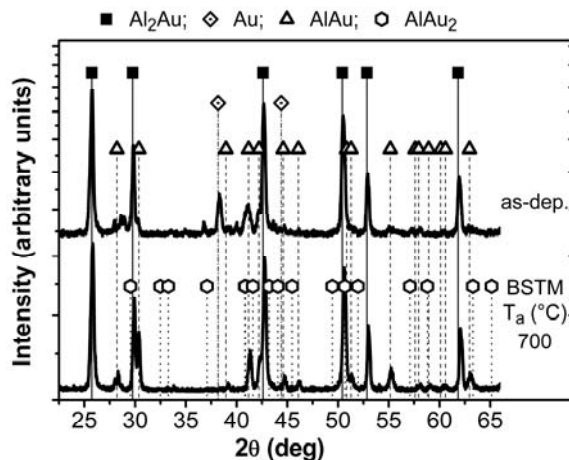
Fig.4 XRD scans of the as-deposited film with an Al/Au at% ratio of 1.85 compared to a pattern taken after BSTM vacuum annealing to 700 °C.

Strong structural changes are detectable for the ternary and porous coating with an Al/Au ratio of 1.85 (Fig. 5a). For temperatures above 450 – 500 °C no Au reflexes can be detected, corresponding to the above mentioned results after BSTM. The AlAu and $AlAu_2$ phases melt at ~625 °C in agreement with their reported melting point [16], indicated by the increased background intensity. The decreasing intensities of the Al_2Au reflexes for T $\geq$ 850 °C suggest melting of this phase according to the solidus-liquidus transition indicated in the Al-Au binary phase diagram for coating compositions between 34 and 55 at % Au [16]. At 900 °C no Al_2Au reflex can be detected anymore. Upon cooling from 900 °C back to room temperature intermetallic AlAu, $AlAu_2$ (as found after BSTM vacuum heat treatment to 700 °C), and Al_2O_3 are formed. Due to the formation of aluminium oxides the parent chemical composition changes to a more Au rich film configuration where no Al_2Au phase is formed in accordance with the binary phase diagram [16].

HT-XRD investigations in synthetic air of the single-phase intermetallic Al_2Au coating reveal no structural changes up to a temperature of ~850 °C, with the (311) peak being constant in intensity (see Fig. 5b). At 900 °C the (220) and (222) Al_2Au reflexes increase in intensity on the expanse of the (311), indicating recrystallization processes and the formation of new defect-free grains, as the relative intensities approach those reported in the JCPDS [17]. For T $\geq$ 850 °C Al_2O_3 reflexes can be detected, which increase in intensity upon cooling to ~500 °C. Due to the formation of Al_2O_3 and the concomitant Al reduction of our Al_2Au film, the typical film composition shifts –especially adjacent the Al_2O_3

regions– from the single-phase Al_2Au field to the binary phase field Al_2Au–AlAu explaining the formation of AlAu.
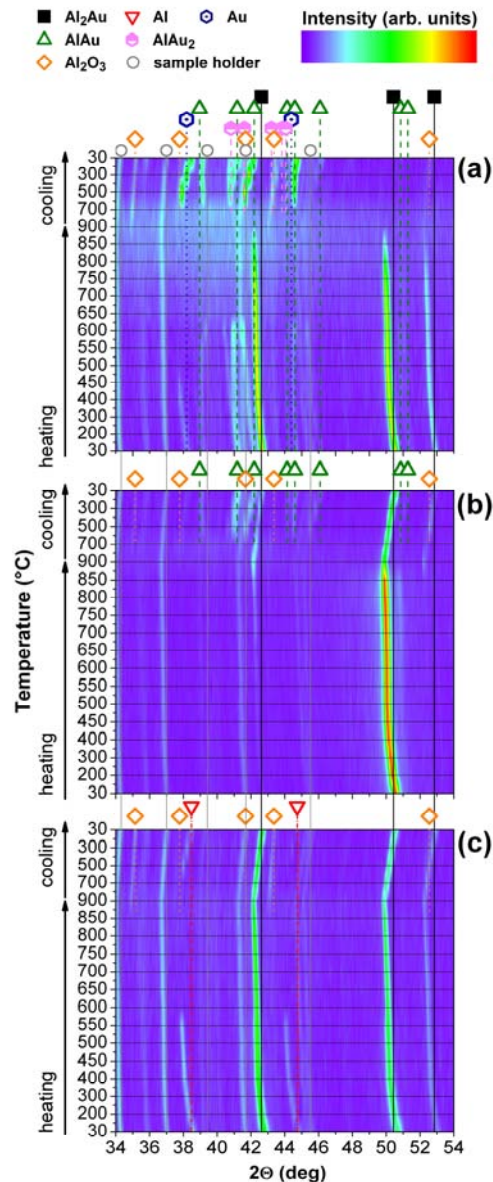

Fig.5 High-temperature XRD maps of the coatings with Al/Au at% ratios of 1.85 (a), 2.00 (b), and 4.32 (c) on Si(100) derived from isothermal measurements between room temperature and 900 °C in synthetic air.

The binary film with an Al/Au ratio of 4.32 shows no structural changes during HT-XRD up to 575 °C (Fig. 5c). For T ≥ 600 °C no reflexes for Al can be detected anymore suggesting its melting. The reduced melting point may result from the nm size Al tissue phase encapsulated in the Al_2Au matrix and its small grain size found during TEM investigations.[5] Literature reports that the melting point of Al clusters with a diameter of

~20 Å is reduced by more than 150 °C from that of bulk Al of ~660 °C [18]. The Al$_2$Au reflexes are almost unaffected by the heat-treatment up to 900 °C.

DSC and TGA curves from a dynamic measurement in oxidizing atmosphere at a heating rate of 20 K/min are presented in Fig. 6 for our films with an Al/Au ratio of 1.85, 2.00, and 4.32.
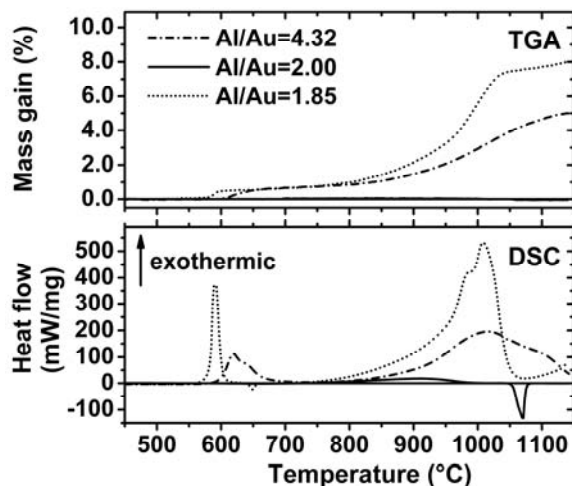
Fig.6 Dynamical DSC and TGA scans of three coatings with Al/Au at% ratios of 1.85, 2.00, and 4.32 recorded at a heating rate of 20 K/min in synthetic air.

A mass gain of 8% is observed in the TGA measurement of the coating with an Al/Au at% ratio of 1.85 at the maximum temperature of 1150 °C, which is beyond the melting point of Al$_2$Au [16, 19]. Several exothermic and one endothermic feature are found in the DSC scan. Based on the XRD and HT-XRD investigations the exothermic reaction between 550 and 620 °C can be attributed to the formation of intermetallic AlAu and AlAu$_2$ and concomitant consumption of the metastable Au. Furthermore, the increased mass gain in this temperature region suggest onset of oxidation although no distinct oxides could be detected by XRD. The endothermic reaction with an onset temperature of ~630 °C is due to the melting of intermetallic AlAu and AlAu$_2$, see Fig. 5. Comparing the TGA and DSC scan shows that the strong exothermic feature between 700 – 1050 °C with a peak temperature of ~1000 °C is due to oxidation. The shoulder at ~970 °C of this peak indicates melting of the remaining Al$_2$Au phase as obtained by XRD. Even though the superposition with the oxidation reaction hinders the determination of an exact melting point of Al$_2$Au the thermal analyses yield a higher onset of melting as compared to HT-XRD investigations. This can be related to different heating rates –i.e. isothermal steps in HT-XRD versus 20 K/min in thermal analyses– used in the two techniques.

The single-phase intermetallic Al_2Au coating displays excellent oxidation resistance. Neither mass gains were found in the TGA nor can strong exothermic oxidation reactions be detected by the DSC. The small and broad exothermic peak between 700 and 950 °C can be attributed to recovery and recrystallization processes taking place, as found by XRD and HT-XRD investigations (cf. Fig. 3 and 5). The higher onset temperature as compared to the BSTM analyses results from the faster heating rate of 20 K/min in DSC compared to 5 K/min in BSTM. The endothermic melting reaction of Al_2Au can be measured with an onset temperature of ~1050 °C, according to the equilibrium phase diagram [16].

The coating with an Al/Au at% ratio of 4.32 shows two distinct exothermic features in the temperature ranges 500 – 700 °C and 750 – 1150 °C, where several reactions superimpose. Connected with these features is an increase in sample mass indicating oxidation of the film. The contributions from exothermic oxidation reactions between 580 and 700 °C are superposed by the endothermic melting peak of Al, giving rise for the shoulder on the right side of this peak. A similar effect occurs at higher temperatures where the exothermic oxidation reaction is superposed by the endothermic melting reaction of the Al_2Au phase.

DSC and TGA traces of the single-phase Al_2Au coating on Sapphire substrate during isothermal exposure for 50 hours at 750 °C in oxidizing atmosphere are given in Fig. 7. Both, the TGA and DSC scan reveal detectable oxidation of the material starting after ~10 hours. The mass gain of ~1.3 mg/cm^2 is relatively small and the decrease in exothermic heat flow after 40 hours indicates that a dense oxide protects the film from further oxidation. The peaks after ~23 and 40 hours of exposure indicate a multistep oxidation process.
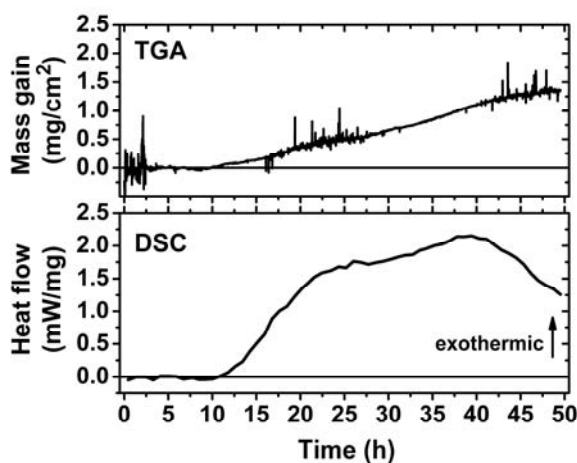
Fig.7 Isothermal TGA and DSC scans at 750°C in synthetic air of our Al_2Au film on Sapphire.

A mass gain of 2 mg/cm^2 is reported for bulk Al$_2$Au after isothermal oxidation tests at 400 °C for 10 hours [20]. This material was revealed with a multistage oxidation process which is also reported for β-NiAl. There, this process is explained by a first step where several forms of Al$_2$O$_3$ (δ, γ, θ) develop by bulk diffusion of Al from the intermetallic bulk to the surface. These oxides are suggested to be non-protective and non-uniform [21]. In a second step the Al$_2$O$_3$ structure changes to α-Al$_2$O$_3$, forming a dense protective layer which is thus slowing down the mass gain rate [21], as can be seen in the TGA curve of our investigations, see Fig. 7.

The XRD patterns taken from the sample after the isothermal test reveal no differences compared to the as-deposited films, suggesting that the formed oxide layer was too thin to display reflexes.

Conclusions

The thermal stability of Al$_2$Au base coatings within the Al-Au system strongly depends on their chemical composition and hence microstructure.

Vacuum annealing of the film-substrate composites show that soft metallic phases embedded in the films with Al/Au at% ratios of 1.85 and 4.32 and their porous structure govern the stress-temperature behavior. These films reveal signs of recovery of structural defects, microplasticiy, and plastic deformation at relatively low temperatures. The single-phase Al$_2$Au coating grows almost stress-free on Si(100) and exhibits a relatively high onset temperature for recovery and recrystallization of 475 and 575 °C (~0.65 of T$_m$), respectively.

Structural investigations with XRD reveal that metastable Au present in the as-deposited Au-rich films is consumed by the growing intermetallic AlAu and AlAu$_2$ phases at T ≥ 450 °C, which themselves melt at ~625 °C. For films with an Al/Au at% ratio of 4.32, nm scale segregation of Al encapsulated in Al$_2$Au domains results in a reduction of the melting point of Al by ~85 °C to 575 °C, as presented by HT-XRD in air. There, single-phase Al$_2$Au was shown to remain its textured structure up to a temperature of ~850 °C where Al$_2$O$_3$ formation and subsequent Al depletion of Al$_2$Au is observed.

In dynamic thermal analyses the Al- and Au- rich films show strong oxidation with mass gains up to 8% whereas the single-phase intermetallic Al$_2$Au coating exhibits no detectable

mass gain up to its melting point of ~1060 °C. In isothermal analyses at 750 °C detectable oxidation of this film starts after ~12 hours. The decreasing exothermic heat flow after ~40 hours of exposure indicates slowing down of the oxidation process and the formation of a dense protective oxide scale.

Thus, we can conclude that the single-phase intermetallic Al_2Au film exhibits good thermal properties. It is superior to the dual- and multi-phase films investigated in the Al-Au system.

Acknowledgements

References

[1]   M. B. Cortie, A. Maaroof, G. B. Smith, and P. Ngoepe, Current Applied Physics, 6, 440 (2006).

[2]   G.H. Meier, in: H. J. Grabke, M. Schütze (Eds.) Oxidation of Intermetallics, (Wiley, Weinheim, 1998).

[3]   R. W. Cahn, Nature, 396, 523 (1998).

[4]   H. C. Shih, Z. Metallkde, 71, 577 (1980).

[5]   M. Moser, P. H. Mayrhofer, I. M. Ross, and W. M. Rainforth, Microstructure and Mechanical Properties of Sputtered Intermetallic Al-Au coatings, submitted Journal of Applied Physics (2007).

[6]   C. Mitterer, H. Lenhart, P. H. Mayrhofer, and M. Kathrein, Intermetallics, 12, 579 (2004).

[7]   P. H. Mayrhofer, G. Tischler and C. Mitterer, Galvanotechnik, 3, 92, (2001).

[8]   P. H. Mayrhofer and C. Mitterer, Surf. Coat. Technol., 133-134, 131 (2000).

[9]   W. D. Nix, Metallurgical Transactions A, 20, 2217 (1989).

[10]   J. D. Wilcock and D. S. Campbell, Thin Solid Films, 3 (1969).

[11]   H. Ebert, in: K. Schäfer, G. Beggerow (Eds.) Landolt-Börnstein, Eigenschaften der Materie in ihren Aggregatzuständen, 1. Teil, Mechanisch Thermische Zustandgrößen, (Springer, Berlin, 1971)

[12]   P. H. Mayrhofer, G. Tischler, and C. Mitterer, Surf. Coat. Technol., 142, 78 (2001).

[13]   P. H. Mayrhofer, F. Kunc, J. Musil, and C. Mitterer, Thin Solid Films, 415, 151 (2002).

[14]   G. Dehm, T. J. Balk, H. Edongué, and E. Arzt, Microelectr. Eng., 70, 412 (2003).

[15]   A. K. Bhattacharya, and W. D. Nix, Int. J. Sol. Struct., 24, 12, 1287 (1988).

[16]   H. Okamoto, J. Phase Equil., 12, 114 (1991).

[17]   Joint committee of powder diffraction standard (JCPDS) card N° 17-877 (Al2Au), 30-0019 (AlAu), 26-1006 (AlAu2), 4-784 (Au) and 4-787 (Al).

[18]   S. L. Lai, J. R. A. Carlsson, and L. H. Allen, Appl. Phys. Let., 72, 1098 (1998).

[19]   M. Moser, P. H. Mayrhofer, and R. Braun, in Advanced Intermetallic-Based Alloys, edited by C.L. Fu, H. Clemens, J. Wiezorek, M. Takeyama, D. Morris (Mater. Res. Soc. Symp. Proc. 980, Warrendale, PA, 2007), 0980-II05-08.

[20]   C. Xu, C. D. Breach, T. Sritharan, F. Wulff, and S. G. Mhaisalkar, Thin Solid Films 462, 357 (2004).

[21]   P. Lamesle, M. Vilaso, and J. M. Claude, Mater. Sci. Forum 251-254, 171 (1997).

Publication III

Magnetron Sputtered Intermetallic Al$_2$Au and Al-Zr-Y coatings for the oxidation protection of γ-TiAl

M. Moser, P. H. Mayrhofer, R. Braun

MAGNETRON SPUTTERED INTERMETALLIC Al₂Au AND Al-Zr-Y COATINGS FOR THE OXIDATION PROTECTION OF γ-TiAl

M. Moser[1], P. H. Mayrhofer[1], R. Braun[2]

[1]Department of Physical Metallurgy and Materials Testing, Montanuniversität Leoben, Franz-Josef-Strasse 18, A-8700 Leoben, Austria

[2]Institute of Materials Research, DLR- German Aerospace Centre, D-51170 Cologne, Germany

Abstract

Al-based intermetallic coatings are widely used as bond coats and for oxidation protection of turbine blades and engine components. Here we present and discuss the structural and thermal properties of novel unbalanced-magnetron sputtered Al-based coatings (single-phase intermetallic Al₂Au, binary Al-Zr, and nano-structured Al-Zr-Y) developed to protect γ-TiAl from environmental attack at elevated temperatures. Al-Zr films exhibit a coarse-grained dual-phase Al_3Zr_2-Al_2Zr structure and are nano-structured by alloying with ~5, 10, and 14 at% Y.

Combined dynamic differential-scanning calorimetry and thermogravimetric analyses up to a temperature of 1150 °C reveal that the Al₂Au film is very stable with only marginal mass gain from oxidation found between 800 and 1000 °C. High temperature X-ray diffraction shows that this coating retains its (311) texture up to 900 °C where Al_2O_3 formation leads to the depletion of Al in Al₂Au and subsequently the precipitation of intermetallic AlAu. When γ-TiAl is coated with Al₂Au and exposed to cyclic oxidation tests at 750 and 850 °C good oxidation resistance is obtained as a protective oxide layer is formed.

Dual-phase Al_3Zr_2-Al_2Zr coatings form ZrO_2 and Al_2O_3 in oxidizing atmosphere. However, the phase transition from monoclinic (m-)ZrO_2 to tetragonal (t-)ZrO_2 with the accompanying volume change causes flaking of the oxide. Yttrium addition to the Al-Zr films stabilizes the cubic (c-) and t-ZrO_2 and hence avoids the fatal tetragonal-monocline transformation. The thermally grown c-ZrO_2 based oxides allow good adhesion to thermal barrier coatings which are themselves based on c-ZrO_2.

Introduction

γ-TiAl offers attractive properties such as low density, high specific stiffness, high yield strength and good creep resistance up to ~800 °C and has thus the potential to replace heavy materials such as steels or nickel-based alloys at high temperature applications in automotive, aerospace and power generation industries [1-4]. Nevertheless, its poor oxidation resistance at temperatures above 750 °C limits a wider utilization, due to the formation of non protective layers of alumina and fast growing titania [5]. Therefore, coating systems have to be developed to effectively and sustainably protect γ-TiAl from environmental attack over the entire anticipated component lifetime [6-9].

We thus present novel Al based intermetallic coatings (single-phase intermetallic Al_2Au and Al-Zr-Y films) designed to protect γ-TiAl. Al_2Au is a Zintl-phase which crystallizes in an fcc CaF_2-type structure. Single-phase Al_2Au films have excellent mechanical and thermal properties compared with coatings containing higher amounts of Al or Au [10, 11, 15].

Our Al-Zr coatings are based on the intermetallic phases Al_3Zr_2 and Al_2Zr which have melting points above 1400 °C [12]. By adding Y to Al-Zr the formation of cubic (c-) ZrO_2 can be triggered during film oxidation and hence the fatal monoclinic (m-) to tetragonal (t-) phase transition in zirconia [13] with its ~7.5 % volume change can be avoided [14]. The thermally grown c-ZrO_2 based oxides will have good adhesion to thermal barrier coatings which are themselves composed of yttria stabilized zirconia.

Here, further results on the thermal stability of single-phase intermetallic Al_2Au coatings are presented which demonstrate their ability to protect γ-TiAl. Furthermore, we show first results on the influence of Y on the structure, thermal stability, and oxide formation of Al-Zr coatings.

Experimental

Al_2Au and Al-Zr-(Y) coatings are deposited on Si(100), Sapphire, low alloyed steel and γ-TiAl (Ti-45Al-8Nb) substrates in a magnetically unbalanced magnetron sputtering system. For Al-Zr-Y films the different coating compositions are obtained by placing varying amounts of 1x1cm Y plates on the race track of an $Al_{0.63}Zr_{0.37}$ target. Details on the sputtering system and the deposition conditions are given in Refs. [10] and [15], and are similar to those reported in our previous paper on Al-Au coatings [11]. The microstructure

of the different films was investigated using a Siemens D500 Bragg-Brentano X-ray diffractometer with Cu-Kα radiation in the 2θ range between 20 and 70 deg. Coating morphology and film compositions were examined using scanning electron microscopy (SEM; ZEISS EVO 50) equipped with Oxford Instruments INCA energy dispersive spectrometer. Mechanical properties, such as hardness of indention (H) and modules of indentation (E) are determined from unloading segments of load-displacement curves during computer controlled indentation tests using a Fischerscope H100 and a maximum load of 35 mN. The presented values are averaged from a minimum of 20 indents.Differential scanning calorimetry (DSC) with simultaneous thermo-gravimetric analyses (TGA) was performed in a Netsch-STA 409C to characterize the oxidation behaviour of the coatings by thermal ramping from 450 to 1150 °C for Al$_2$Au and from 300 to 1100 °C for Al-Zr-Y at 20 K/min in synthetic air. These analyses were conducted on film material after chemical removal with 3.5M HNO$_3$ from their low alloy steel substrates, or on coatings on Sapphire to avoid interference with substrate material. Thermal cycling tests were performed at DLR Cologne in automated rigs in laboratory air at 750 and 850 °C. One cycle consists of an isothermal segment of 1 h at temperature and 10 min for cooling down to ~60 °C. Samples were periodically weighed and visually inspected during testing up to an exposure time period of 1000 cycles.

Results and Discussion

Intermetallic single-phase Al$_2$Au films

Sputter deposited Al$_2$Au films exhibit a dense columnar (311) texture with domain sizes of ~230 nm. The coating has a hardness of 7.9±1.2 GPa and an indentation modulus of 144±9.0 GPa [10].

Dynamic DSC and TGA scans conducted in inert and oxidizing atmosphere on powdered Al$_2$Au coatings at a heating rate of 20 K/min are presented in Fig. 1. The scan in argon reveals only small reactions up to a temperature of ~1060 °C where a strong endothermic peak indicates melting of the intermetallic Al$_2$Au phase. The melting point is in good agreement to that of the binary phase diagram of 1060 °C [16]. The DSC/TGA scan in synthetic air reveals no major differences compared to the evaluation in argon. The small mass gain of less than 0.5 % in combination with the exothermic reaction found in DSC in the temperature range 700—1000 °C indicate oxidation of the material. The onset

temperature of the melting reaction of Al_2Au in synthetic air is identical to the measurement in argon atmosphere at ~1060 °C. The mass loss observed in TGA simultaneously with melting of Al_2Au can be attributed to evaporation of Al.
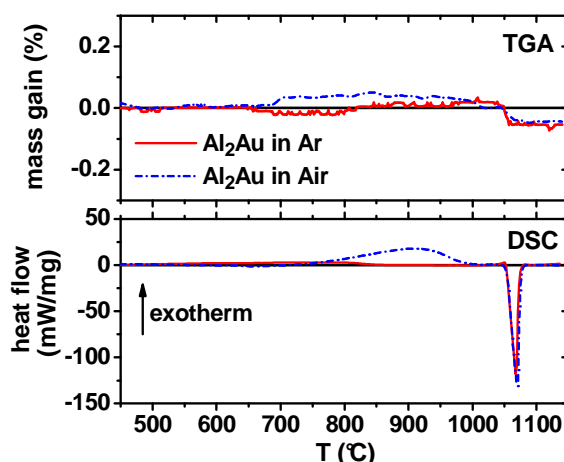

Fig.1 Dynamic DSC and TGA scans of powders of the Al2Au film recorded in argon (solid line) and synthetic air (dash-dotted line).

Structural evolution of Al_2Au on Si(001) during high-temperature exposure shows that the film retains a single-phased (311) texture up to a temperature of 850 °C. Above 850 °C the intensity of the (311) peak decreases and the (220) and (222) Al_2Au reflexes increase together with the Al_2O_3 reflex. The formation of this oxide causes Al depletion of Al_2Au and consequently intermetallic AlAu is formed as Al_2Au has only a narrow composition stability range of less than 1 at% at that temperature. Thus, Al_2Au, AlAu, and Al_2O_3 are detected at room temperature after the high temperature experiment [15].

The high potential of Al_2Au to protect γ-TiAl from environmental attack is shown in the mass-change vs. number of 1-h cycles plot (Fig. 2). The measurements of Al_2Au coated γ-TiAl samples at 750 and 850 °C exhibit a logarithmic mass gain versus time profile following the equations (1) and (2), respectively [17], although transmission electron microscopy results indicate a massive restructuring of the film [18].

$$750\,°C: \qquad y = 0.10 \cdot \ln(2.62 \cdot x + 0.99) \qquad\qquad (1)$$

$$850\,°C: \qquad y = 0.07 \cdot \ln(121.46 \cdot x + 1.00) \qquad\qquad (2)$$

Thermal cycling of the uncoated substrate material at 750 °C leads to a smaller mass gain within the investigated cycling range as compared to the coated material but shows a parabolic mass gain profile which can be described by equation (3).

$$y^2 = 2 \cdot 10^{-4} \cdot x \tag{3}$$

Consequently, higher mass gains are expected for the uncoated material after longer exposure durations and equations (1) and (3) suggest that after ~4400 thermal cycles at 750 °C the mass gain of the substrate intersect with that of coated γ-TiAl. Increasing the cycling temperature to 850 °C leads to the onset of rapid oxidation of the substrate material resulting in a mass gain of ~2 mg/cm^2 after 1000 cycles, which is ~three times the increase observed for the coated material.
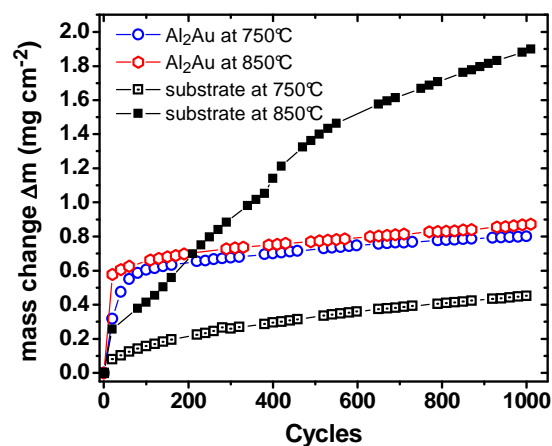
Fig.2 Mass change vs. number of 1-h cycles to 750 and 850 °C of uncoated Ti-45Al-8Nb (substrate) compared to specimens coated with Al$_2$Au.

Zr-Al-Y coatings

Yttrium-free Al-Zr coatings grow with a dense columnar structure having a composition of 60 at% Al and 40 at% Zr (i.e. Al-40Zr) and H and E values of 11.5±0.6 GPa and 166±6 GPa, respectively. Adding 5, 10, and 14 at% Y to the coating leads to an increase of coating thicknesses from ~3 to ~5µm, a change from columnar to a featureless nanostructure (Fig 3) and to chemical compositions of Al-37Zr-5Y, Al-34Zr-10Y, and Al-31Zr-14Y, respectively. The hardness and indentation modulus are 8.7±0.6 GPa and 138.7±8 GPa, 8.5±0.3 GPa and 122±4 GPa, and 8.2±0.2 GPa and 140±3 GPa, for the 5, 10, and 14 at% Y containing films, respectively. Hence by adding Y to Al-Zr both, H and E, decrease.
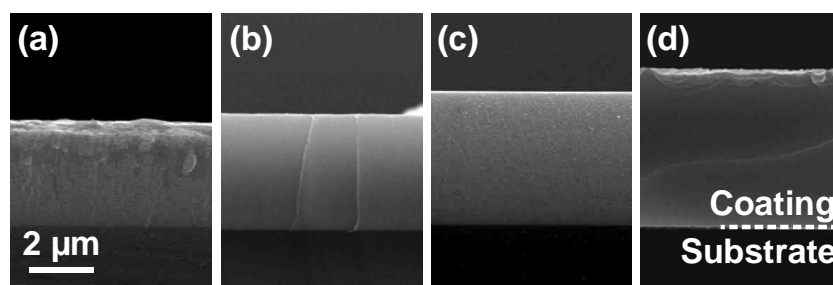
Fig.3 SEM fracture cross-sections of our Al-Zr-Y coatings with (a) 0 at% Y, Al-40Zr, (b) 5 at% Y, Al-37Zr-5Y, (c) 10 at% Y, Al-34Zr-10Y, and (d) 14 at% Y, Al-31Zr-14Y deposited on Si(100).

Fig. 4 presents XRD patterns taken from as-deposited films. The Y-free Al-Zr film exhibits a binary phase structure composed of Al_2Zr_3 and Al_3Zr_2. With increasing Y content the intensities of these intermetallic phase reflexes decrease and broad reflexes can be detected which indicate the formation of a nanostructure with grain sizes below ~5 nm. Consequently, their fracture cross-section appears featureless (compare Fig. 3).
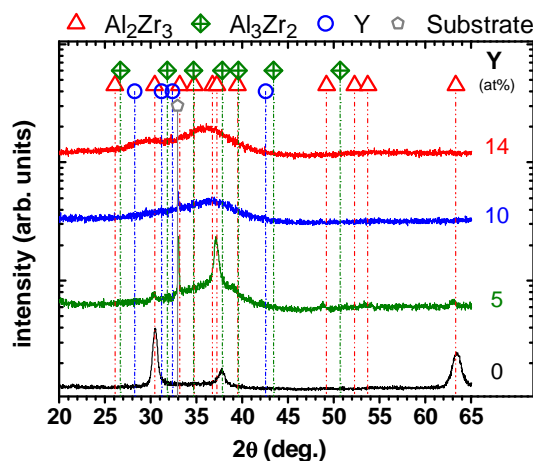
Fig.4 XRD patterns taken of the as-deposited Al-Zr-Y coatings with different Y contents.

Dynamic DSC and TGA scans of a powder of our Al-Zr coating (Fig. 5a) is compared to measurements on Al-Zr-Y films coated on Sapphire (Fig. 5b). Due to the volume increase of ~7.5% by the transformation from tetragonal to monoclinic-ZrO_2 [13, 14], and the thereby resulting flaking, measurements on Al-Zr coated Sapphire failed. Consequently, Fig. 5a cannot directly be compared with Fig. 5b. Nevertheless, both graphs reveal multiple exothermic features which can be attributed to oxidation obtained from the corresponding mass increases. Our TGA analyses indicate that the onset temperature for these reactions increases with increasing Y content from ~450 °C with 0 at% Y to 550, 630, and 670 °C with 5, 10, and 14 at% Y, respectively.
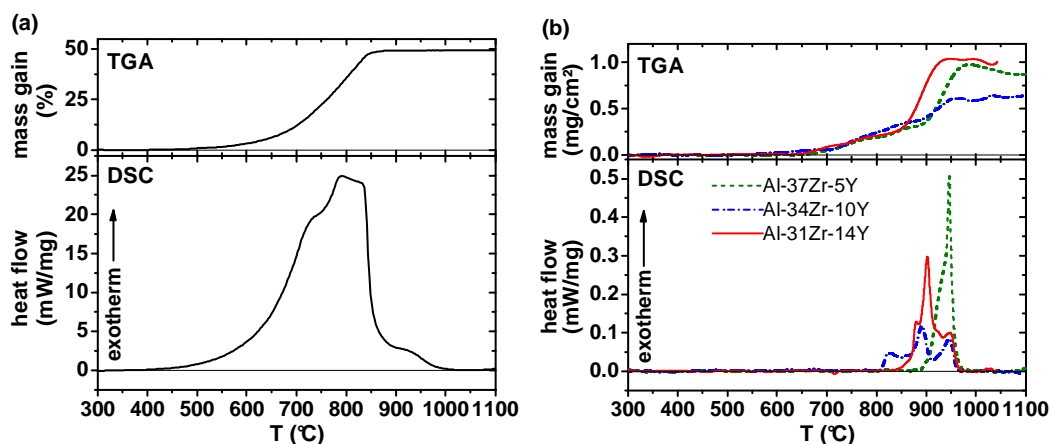
Fig.5 Dynamic DSC and TGA scans of our Al-Zr-Y films with (a) 0 and (b) 5, 10, and 14 at% Y recorded at a heating rate of 20 K/min in synthetic air.

XRD patterns of our oxidized samples after the DSC/TGA measurements up to 1100 °C are given in Fig. 6. The Y-free binary Al-Zr film primarily oxidizes to form α-Al_2O_3 and m-ZrO_2 (stable at T <~1100 °C). At T ~ 1100 °C undoped m-ZrO_2 transforms to t-ZrO_2 with a volume increase of ~ 7.5% [13]. The observed flaking of the oxides in our experiments to 1100 °C indicate that the m- to t-ZrO_2 transformation (partially) occurs at T $\leq$ 1100 °C due to the addition of Al in the coating, in agreement to Ref. [19]. Consequently, no dense oxide layer is formed which could protect γ-TiAl. The addition of only 5 at% Y to our Al-Zr films leads to the predominant formation of c- and t-ZrO_2, with small fractions of m-ZrO_2. By further increasing the Y content to 10 and 14 at% the formation of m-ZrO_2 can completely be suppressed. The formed oxides are transparent, and our results indicate that they solely consist of c-ZrO_2 and α-Al_2O_3. The latter is found in all coatings investigated.
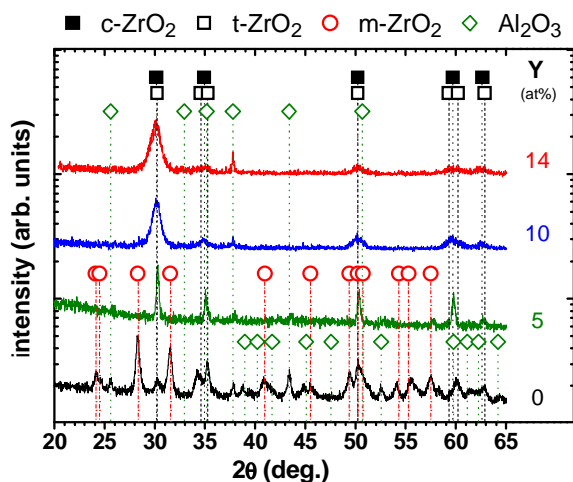
Fig.6 XRD patterns of our Al-Zr-Y coatings with different Y contents after oxidation during thermal analyses up to 1100 °C.

Conclusions

Based on our results we can conclude that the newly developed Al based intermetallic coatings, single-phase Al_2Au and multi-phase Al-Zr-Y, can effectively protect oxidation sensitive materials like γ-TiAl at elevated temperatures. Thermal cycling tests in air revealed a logarithmic mass gain rate of Al_2Au coated γ-TiAl samples due the formation of a dense oxide layer.

The transformation of t-ZrO_2 to m-ZrO_2 with its destructive volume increase of ~7.5 % occurring during oxidation of Al-Zr coatings can be suppressed by alloying the films with Y. Al-Zr films containing 10 and 14 at% Y form m-ZrO_2 free transparent oxides consisting of c-ZrO_2 and Al_2O_3 upon heating to temperatures above 630 and 670 °C, respectively. Consequently, these coatings, with their thermally grown yttria stabilized zirconia, have high potential to act as protective coatings used in automotive, aerospace and power generation industries.

Acknowledgements

References

[1]   H. Clemens, A. Lorich, N. Eberhardt, W. Glatz, W. Knabl, and H. Kestle, Z Metallkd 90 (8), 569-580 (1999).

[2]   H. Clemens and H. Kestler, Adv. Eng. Mater. 2, 551 (2000).

[3]   H. Kestler and H. Clemens, in Titanium and Titanium Alloys, edited by C. Leyens and M. Peters (Wiley-VCH, 2003) pp. 351-392.

[4]   F. Appel and R. Wagner, Materials Science and Engineering: R: Reports 22, 187 (1998).

[5]   C. Leyens, M. Peter, P. Eh. Hovsepian, D. B. Lewis, Q. Luo, and W-D. Münz, Surf. Coat. Technol. 155, 103-111 (2002).

[6]   M. Schütze ed., Corrosion and Environmental Degradation Vol. II, (Wiley-VCH, London)

[7]   R. Pichoir, Aluminide coatings on nickel or cobalt-base superalloys, in High Temperature Alloys for Gas Turbines, edited by D. Coutsouradis et al., (Appl. Sci. Pub., London, 1978), p. 191.

[8]   Y. Zhang, Aluminide coatings for power-generation applications, Technical Report, ORNL/Sub/01-47035/01

[9]   R. Sivakumar et al., Surf. Sci. Techn., 37, 139 (1989)

[10]   M. Moser, P. H. Mayrhofer, I. M. Ross, and W. M. Rainforth: Thermal Stability of Sputtered Intermetallic Al-Au Coatings, submitted, 2006.

[11]   C. Mitterer, H. Lenhart, P. H. Mayrhofer, and M. Kathrein, Intermetallics 12, 579 (2004)

[12]   J. Murray, A. Peruzzi, and J. P. Abriata, J. Phase Equilibria, 13, 277-291 (1992)

[13]   M. Yashima, M. Kakihana, and M. Yoshimura, Solid State Ionics, 86-88, 1131 (1996),

[14]   S. Stecura, NASA Tech. Memo. (1985), 86905

Publication IV

Yttrium induced structural changes in sputtered Ti$_{1-x}$Al$_x$N thin films

M. Moser and P. H. Mayrhofer

YTTRIUM INDUCED STRUCTURAL CHANGES IN SPUTTERED $Ti_{1-x}Al_xN$

THIN FILMS

M. Moser and P. H. Mayrhofer

Department of Physical Metallurgy and Materials Testing, Montanuniversität Leoben,

Franz-Josef-Strasse 18, A-8700 Leoben, Austria

Abstract

Metastable $Ti_{1-x}Al_xN$ thin films synthesised by plasma-assisted vapour deposition crystallize in the industrially preferred cubic NaCl (*c*) structure with AlN mole fractions (*x*)≤0.7. Employing X-ray diffraction and transmission electron microscopy we reveal that the addition of Yttrium to c-$Ti_{1-x}Al_xN$ shifts the solubility limit to lower AlN contents, resulting in mixed *c*- and hexagonal ZnS-wurtzite (*w*) phased $(Ti_{1-x}Al_x)_{1-y}Y_yN$ coatings. *Ab-initio* calculations yield a by ~23% decreased solubility limit in c-$Ti_{1-x}Al_xN$, from *x*~0.69 to 0.56 with the addition of *y*=12.5 at% Y.

Key words: ab-initio electron theory, metastable phases, thin films, physical vapor deposition (PVD), Yttrium

Introduction

Known for their good physical, mechanical, and chemical properties $Ti_{1-x}Al_xN$ films and/or their alloys are used in a variety of applications ranging from wear protection of tools, dies, and molds to components in aerospace and automotive industry [1, 2]. The extremely high cooling rates ($\sim10^{13}$ K/s) as well as the limited atomic assembly kinetics during low-temperature plasma-assisted vapour deposition (0.2-0.3 of the homologues temperature) allow the preparation of supersaturated solid-solutions like $Ti_{1-x}Al_xN$ [3, 4]. Literature shows that $Ti_{1-x}Al_xN$ crystallizes in the cubic NaCl (*c*) modification (space group $Fm\bar{3}m$) for AlN mole fractions (x)≤0.7 [5-10]. Exceeding the metastable solubility limit results in a mixed (NaCl + ZnS – wurtzite) structure, or the films crystallize completely hexagonal ZnS – wurtzite (*w*) (space group $P6_3mc$) [5-9]. Both, thermodynamic and *ab-inito* calculations indicate a critical maximum AlN fraction of ~0.7 for c-$Ti_{1-x}Al_xN$ [11-13], and Ref. [14] reports that this metastable phase stability limit can be varied between 0.64 and 0.74 by influencing the Al distribution on the metal sub-lattice. Hence, mechanisms which influence the Al distribution during growth will influence the metastable solubility limit. We suggest that similar effects are responsible for the exceptionally high solubility of 81 mole% AlN in c-$Ti_{1-x}Al_xN$ observed during plasma assisted chemical vapour deposition [15]. Generally, with deposition techniques involving high ionization rates like arc-evaporation [5, 8, 10], arc-ion-plating [7], or the mentioned plasma assisted chemical vapour deposition [15], c-$Ti_{1-x}Al_xN$ with higher AlN mole fractions can be synthesized as compared to conventional magnetron sputtering [6, 16]. Due to the better mechanical and tribological properties the cubic modification is preferred over the hexagonal one in industrial applications [7, 9, 17].

Alloying Yttrium to TiN and $Ti_{1-x-y}Al_xCr_yN$ is reported to improve mechanical properties and oxidation resistance due to Y segregation-caused grain refinement during film growth and the strong affinity of Y to oxygen [18-2]. Nevertheless, a critical literature research revealed that the effect of varying amounts of Y on the structure of monolithically grown $Ti_{1-x}Al_xN$ has not been studied.

Experimental

Therefore, coatings are investigated which are produced by unbalanced magnetron sputtering from 99.9% purity $(Ti_{0.5}Al_{0.5})_{1-y}Y_y$ targets (PLANSEE SE) containing y=0, 2, 4,

and 8 at% Y. With a deposition temperature of 550 °C, a target power density of 9 W/cm^2, a bias potential of -50 V, and a N$_2$/Ar partial pressure ratio of 0.4 (both gases with 99.999% purity), slightly over-stoichiometric nitride coatings (~51 at% N) are produced at a working gas pressure of 0.5 Pa (base pressure below 0.3 mPa). With the individually used targets, coatings are synthesized containing 0 (Ti$_{0.45}$Al$_{0.55}$N), 3 (Ti$_{0.42}$Al$_{0.56}$Y$_{0.03}$N), 5 (Ti$_{0.43}$Al$_{0.52}$Y$_{0.05}$N), and 9 at% Y (Ti$_{0.38}$Al$_{0.53}$Y$_{0.09}$N) in the metallic sub-lattice (we will keep this notation for the Y content throughout the manuscript). The chemical compositions of our films are determined by energy dispersive X-ray analyses (EDX) during scanning electron microscopy studies using a Zeiss EVO 50 microscope equipped with an Oxford Instruments INCA EDX unit. The observed increase in Al/Ti ratio from 1 to 1.2-1.4 when comparing the composition of the used targets with the respective coatings is in good agreement with literature where generally higher Al and lower Ti contents as in the targets are reported for magnetron sputtered films [9, 21].

Results and Discussion

Figure 1 presents X-ray diffraction (XRD) patterns of powdered as-deposited coatings after chemical removal with 10 mol% nitric acid from their low-alloyed steel substrates recorded with a Siemens D500 diffractometer in Bragg-Brentano geometry using Cu Kα radiation. The diffraction pattern of the Y-free Ti$_{0.45}$Al$_{0.55}$N film indicates a single-phased cubic structure with a lattice parameter a_c of 4.178 Å, determined according to the Cohen-Wagner method [22]. This value suggests a specific volume V$_c$ of 9.12 Å^3/at and is in good agreement with experimental and computed parameters [14]. XRD single line profile analyses employing the Pseudo-Voigt method yields a mean crystallite feature size of 25 nm for the Y-free coating [23].

The film with 3 at% Y (in the metallic sub-lattice) exhibits small fractions of hexagonal ZnS-wurtzite reflexes in addition to the cubic XRD peaks (Fig. 1). With increasing Y content the intensities of the hexagonal reflexes increase with concomitant decreasing cubic reflex intensities. For the highest Y containing film (Ti$_{0.38}$Al$_{0.53}$Y$_{0.09}$N) only a small reflex can be detected for the cubic phase at 2θ ~43 deg. These results suggest an increasing fraction of the hexagonal phase with increasing Y content on the expanse of the cubic modification. Diffraction angle positions of the hexagonal phase are used to calculate the lattice parameters a$_w$ and c$_w$ for w-(Ti$_{1-x}$Al$_x$)$_{1-y}$Y$_y$N yielding a$_w$=3.075 and c$_w$=5.295 Å for *y*=2 at%, a$_w$=3.185 and c$_w$=5.215 Å for *y*=5 at%, and a$_w$=3.205 and c$_w$=5.220 Å for *y*=9

at%. Consequently, the specific volumes V_w increase from 10.84 to 11.45 to 11.61 Å^3/at with increasing Y content from 3 to 5 to 9 at%, respectively. The lattice parameters of the cubic phases in our films vary only within the error of measurement between a_c=4.178 and 4.181 Å. Hence, their specific volume changes just between 9.12 and 9.14 Å^3/at.
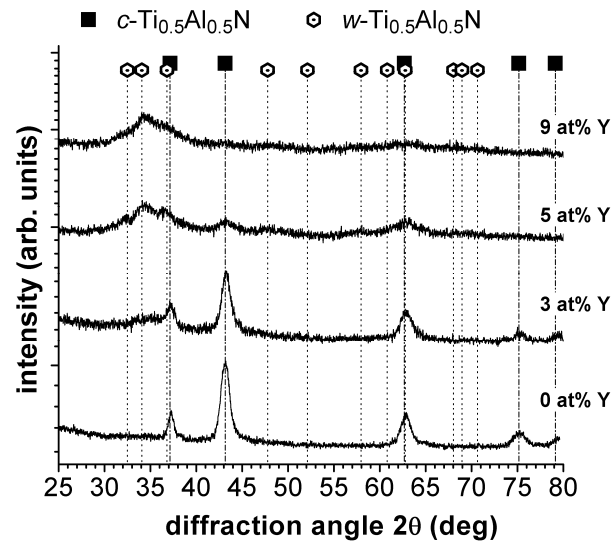

Fig.1 XRD patterns of as deposited $(Ti_{1-x}Al_x)_{1-y}Y_yN$ films containing y=0 ($Ti_{0.45}Al_{0.55}N$), 3 ($Ti_{0.42}Al_{0.56}Y_{0.03}N$), 5 ($Ti_{0.43}Al_{0.52}Y_{0.05}N$), and 9 at% Y ($Ti_{0.38}Al_{0.53}Y_{0.09}N$) in the metallic sub-lattice.

Hardness (H) and modulus of indentation (E) measured with a Fischerscope H100C gradually decrease with increasing Y content from 25.7±1.5 and 437.9±1.8 GPa for $Ti_{0.45}Al_{0.55}N$ to 15.9±1.4 and 196.3±0.8 GPa for $Ti_{0.38}Al_{0.53}Y_{0.09}N$, respectively. The decreasing H and E values with increasing Y-content are related to the increasing fraction of the hexagonal phase with its typically lower hardness and elastic modulus (Ref. [14]). Corresponding results are obtained by exceeding the metastable solubility limit of AlN in c-$Ti_{1-x}Al_xN$ coatings [7, 9].

Cross-sectional transmission electronic microscopy (TEM) studies using a Phillips CM12 microscope operated with 120 keV exhibit a dense columnar microstructure for Y-free $Ti_{0.45}Al_{0.55}N$ (Fig. 2a) and a fine texture of featherlike, small-diameter grains elongated in growth direction for the 9 at% Y containing w-$Ti_{0.38}Al_{0.53}Y_{0.09}N$ film with cubic traces (Fig. 2b). The image contrast of Fig. 2a suggests a column width of ~22 nm, a high defect density, and strain fields for $Ti_{0.45}Al_{0.55}N$. Residual stress measurements employing the substrate curvature method yield compressive stresses of -1.9±0.19 GPa. The micrograph of the film with 9 at% Y (Fig. 2b) reveals a lower contrast and hence a lower defect density

and strains, corresponding to their lower residual compressive stresses of -0.81±0.04 GPa. Similar microstructures are reported in literature for mixed *c*- and *w*-phased $Ti_{0.31}Al_{0.69}N$ and $Ti_{0.26}Al_{0.74}N$ films [8, 9]. Selected-area electron diffraction (SAED) pattern presented in Figs. 3a and b confirm the XRD analyses of a single-phased cubic structure for the Y-free film and a hexagonal dominated structure with cubic traces for the coating containing 9 at% Y.
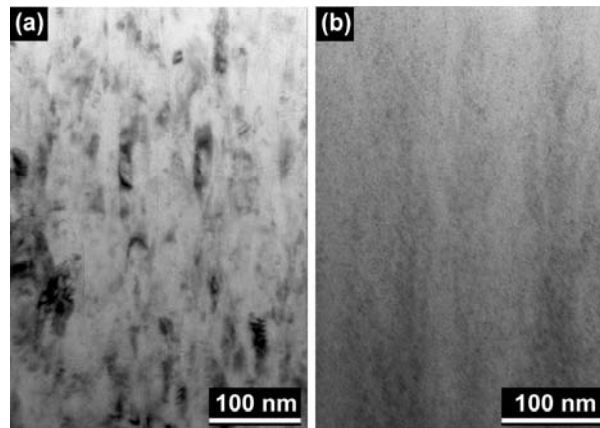

Fig.2 TEM cross-sectional images of (a) $Ti_{0.45}Al_{0.55}N$ and (b) $Ti_{0.38}Al_{0.53}Y_{0.09}N$.

Ab-initio calculations using the VASP code [24, 25], based on the density-functional theory in conjunction with the generalized-gradient approximations projector augmented wave potentials [26], are conducted to calculate lattice parameters and energy of formation E_f of $(Ti_{1-x}Al_x)_{1-y}Y_yN$ with 12.5 at% Y in their cubic and hexagonal modification. Therefore, a super-cell approach based on 32 ions is used where Y equally substitutes for Ti and Al. These calculations are based on earlier investigations of *c*-$Ti_{1-x}Al_xN$ and *w*-$Ti_{1-x}Al_xN$ [14].
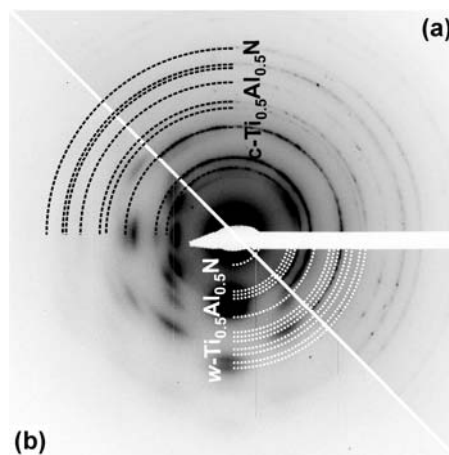
Fig.3 SAED of (a) $Ti_{0.45}Al_{0.55}N$ and (b) $Ti_{0.38}Al_{0.53}Y_{0.09}N$ with diffraction patterns of *c*-$Ti_{1-x}Al_xN$ (dashed line) and *w*-$Ti_{1-x}Al_xN$ (dotted line).

Figure 4 shows E_f for c-$Ti_{1-x}Al_xN$ and w-$Ti_{1-x}Al_xN$ as a function of AlN mole fraction x. The larger negative values for x below ~0.69 indicate a preferred crystallization in the cubic modification [14]. Adding 12.5 at% Y to the metallic sub-lattice equally substituting for Al and Ti results in $\geq$0.07 eV/at smaller negative E_f values for c-$(Ti_{1-x}Al_x)_{1-y}Y_yN$ over the entire x range. For the hexagonal modification w-$(Ti_{1-x}Al_x)_{1-y}Y_yN$ the E_f data for x in the AlN range 0.25-0.75 differ only by $\leq$0.01 eV/at from those of the Y-free w-$Ti_{1-x}Al_xN$. The substitution of 12.5 at% Ti or Al by Y in w-TiN (x=0) or w-AlN (x=1) results in 0.05 or 0.11 eV/at larger or smaller negative E_f values, respectively (see Fig. 4). Comparing the E_f data for cubic and hexagonal $(Ti_{1-x}Al_x)_{1-y}Y_yN$ with y=12.5 at% suggests a preferred cubic modification for AlN mole fractions x below ~0.56. Consequently, the metastable solubility limit for AlN in c-$(Ti_{1-x}Al_x)_{1-y}Y_yN$ decreases by 23% from ~0.69 to 0.56 with increasing Y content from y=0 to 12.5 at%, respectively. These results are in excellent agreement to our experimental observations of a structural change from single-phased cubic to mixed cubic-hexagonal further to hexagonal-dominated (with cubic traces) by increasing the Y content from 0 to 3 or 5, and to 9 at%, respectively.
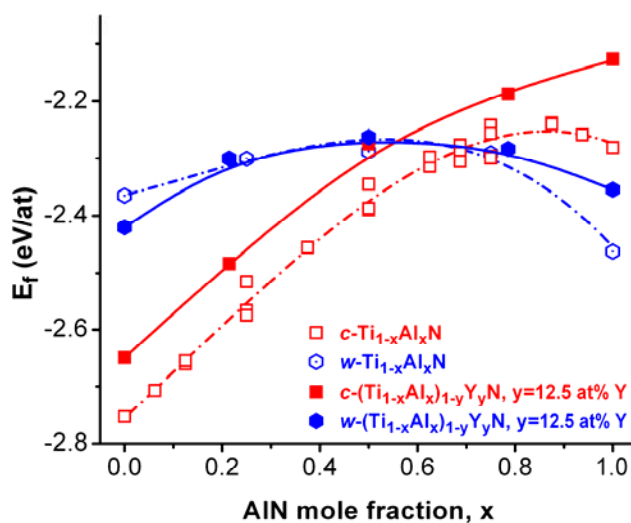

Fig.4 The energy of formation E_f as a function of x for c-$Ti_{1-x}Al_xN$ and w-$Ti_{1-x}Al_xN$ (dash dotted line and open symbols) compared to E_f of c- and w-$(Ti_{1-x}Al_x)_{1-y}Y_yN$ with y=12.5 at% Y at the metallic sub-lattice (solid line and full symbols) [14].

Ab-initio calculations of the lattice parameter of c-$(Ti_{0.5}Al_{0.5})_{1-y}Y_yN$ indicate an increase from a_c=4.184 to 4.315 Å if Y increases from y=0 to 12.5 at%, respectively. Corresponding calculations for the hexagonal modification yield lattice parameters a_w=3.184 and c_w=5.261 Å for y=0 at% Y and a_w=3.281 and c_w=5.251 Å for y=12.5 at% Y. Hence the specific

volume of the cubic modification increases by ~10% from 9.15 to 10.04 Å^3/at whereas V_w for the hexagonal phase changes only by ~6% from 11.55 to 12.26 Å^3/at with increasing Y content from $y=0$ to 12.5 at%, respectively. The experimentally obtained thickness increase of ~38% from 2.2 µm for c-$Ti_{0.45}Al_{0.55}N$ to 3.0 µm for w-$Ti_{0.38}Al_{0.53}Y_{0.09}N$ with cubic traces, found during scanning electron microscope investigations of film cross-sections, can be related to the computed increase in specific volume of 34% from c-$Ti_{0.5}Al_{0.5}N$ to w-$(Ti_{0.5}Al_{0.5})_{0.875}Y_{0.125}N$. Nevertheless, the *ab-initio* obtained increase of the cubic lattice parameter from $a_c=4.184$ to 4.315 Å with increasing Y content from $y=0$ to 12.5 at% is not observed during XRD investigations. The XRD data indicate only minor changes from $a_c=4.178$ to 4.181 Å of c-$(Ti_{1-x}Al_x)_{1-y}Y_yN$ with increasing Y-content from 0 to 5 at%, respectively. These results in addition to the minor change of E_f for the hexagonal modification in the AlN mole fraction range 0.25–0.75 with increasing Y content suggest that Y preferably occupies lattice positions in the hexagonal phase.

Conclusions

Based on our investigations we can conclude that the addition of 12.5 at% Yttrium to $Ti_{1-x}Al_xN$ decreases the metastable solubility limit of the cubic (NaCl) structure by 23% from ~0.69 to 0.56 AlN mole fractions. Therefore, magnetron-sputtered single phased c-$Ti_{0.45}Al_{0.55}N$ coatings develop a mixed NaCl/ZnS-wurtzite microstructure with 3 to 5 at% Y and a predominantly ZnS-wurtzite structure with 9 at% Y in the metallic sub-lattice. With increasing ZnS-wurtzite phase fraction mechanical properties deteriorate. The *ab-initio* calculated energy of formation of c-$(Ti_{1-x}Al_x)_{1-y}Y_yN$ with $y=12.5$ at% Y is shifted by ≥ 0.07 eV/at to smaller negative values compared with c-$Ti_{1-x}Al_xN$ whereas E_f of w-$(Ti_{1-x}Al_x)_{1-y}Y_yN$ is hardly influenced by the Y addition within the AlN mole fraction range 0.25–0.75. Calculations predict increasing lattice parameters a_c and a_w for the cubic and hexagonal modification with increasing Y content, respectively. Nevertheless, in our Y-containing films which have a mixed cubic-hexagonal microstructure solely the hexagonal lattice parameter a_w increases with Y, whereas the cubic lattice parameter a_c changes within the error of measurement. These results in addition with the E_f data, suggest that Y preferably occupies lattice sites of the hexagonal phase.

Acknowledgement

References

[1]   W.D. Münz, J. Vac. Sci. Technol., A 4/6 (1986) 2717.

[2]   P.E. Hovsepian*, et al.*, Surf. Coat. Technol. 201/1-2 (2006) 265.

[3]   T.W. Barbee, W.H. Holmes, D.L. Keith, M.K. Pyzyna, G. Ilonca, Thin Solid Films 45/3 (1977) 591.

[4]   I. Petrov, P.B. Barna, L. Hultman, J.E. Greene, J. Vac. Sci. Technol., A 21/5 (2003) S117.

[5]   A. Hörling, L. Hultman, M. Oden, J. Sjolen, L. Karlsson, J. Vac. Sci. Technol., A 20/5 (2002) 1815.

[6]   R. Cremer, M. Witthaut, D. Neuschütz, in: W.D. Cho, H.Y. Sohn (Eds.), Value-Edition-Metallurgy, The Minerals & Metals Society, Warrendale, PA, 1998, p. 249.

[7]   A. Kimura, H. Hasegawa, K. Yamada, T. Suzuki, Surf. Coat. Technol. 120-121 (1999) 438.

[8]   A. Hörling, L. Hultman, M. Oden, J. Sjolen, L. Karlsson, Surf. Coat. Technol. 191/2-3 (2005) 384.

[9]   K. Kutschej, P.H. Mayrhofer, M. Kathrein, P. Polcik, R. Tessadri, C. Mitterer, Surf. Coat. Technol. 200/7 (2005) 2358.

[10]   P.H. Mayrhofer*, et al.*, Appl. Phys. Lett. 83/10 (2003) 2049.

[11]   H. Stolten, P. Spencer, D. Neuschutz, J. Chim. Phys. Phys.-Chim. Biol. 90/2 (1993) 209.

[12]   H.W. Hugosson, H. Högberg, M. Algren, M. Rodmar, T.I. Selinder, J. Appl. Phys. 93/8 (2003) 4505.

[13]   P.H. Mayrhofer, D. Music, J.M. Schneider, Appl. Phys. Lett. 88/7 (2006) 071922.

[14]   P.H. Mayrhofer, D. Music, J.M. Schneider, J. Appl. Phys. 100/9 (2006) 094906.

[15]   R. Prange, R. Cremer, D. Neuschutz, Surf. Coat. Technol. 133-134 (2000) 208.

[16]   U. Wahlström, L. Hultman, J.E. Sundgren, F. Adibi, I. Petrov, J.E. Greene, Thin Solid Films 235/1-2 (1993) 62.

[17]   H. Ohnuma, N. Nihira, A. Mitsuo, K. Toyoda, K. Kubota, T. Aizawa, Surf. Coat. Technol. 177-178 (2004) 623.

[18]   W.S. Choi, S.K. Hwang, C.M. Lee, J. Vac. Sci. Technol., A 18/6 (2000) 2914.

[19]   L.A. Donohue, I.J. Smith, W.D. Munz, I. Petrov, J.E. Greene, Surf. Coat. Technol. 94-95 (1997) 226.

[20]   B.A. Pint, Oxidation of Metals 45/1-2 (1996) 1.

[21]   J.Y. Rauch, C. Rousselot, N. Martin, Surf. Coat. Technol. 157/2-3 (2002) 138.

[22]   C.N.J. Wagner, in: J.B. Cohen, J.E. Hillard (Eds.), Local Atomic Arrangements Studied by X-ray Diffraction, Gordon and Breach, NY, 1966.

[23]   T.H. DeKeijser, J.I. Langford, E.J. Mittemeijer, A.B.P. Vogels, J. Appl. Crystallogr. 15 (1982) 308.

[24] G. Kresse, J. Hafner, Phys. Rev. B: Condens. Matter 48/17 (1993) 13115.

[25] G. Kresse, J. Hafner, Phys. Rev. B: Condens. Matter 49/20 (1994) 14251.

[26] G. Kresse, D. Joubert, Phys. Rev. B: Condens. Matter 59/3 (1999) 1758.

Publication V

Influence of bipolar pulsed DC magnetron sputtering on chemical composition and micro-structure of Ti-Al-Y-N thin films

M. Moser, P. H. Mayrhofer, L. Székely, G. Sáfrán, P. B. Barna

INFLUENCE OF BIPOLAR PULSED DC MAGNETRON SPUTTERING ON CHEMICAL COMPOSITION AND MICRO-STRUCTURE OF TI-AL-Y-N THIN FILMS

M. Moser[1], P. H. Mayrhofer[1], L. Székely[2], G. Sáfrán[2], P. B. Barna[2]

[1]*Department of Physical Metallurgy and Materials Testing, Montanuniversität Leoben, Franz-Josef Straße 18, A-8700 Leoben, Austria*

[2]*Research Institute for Technical Physics and Materials Science, Hungarian Academy of Sciences, Budapest H-1121, Hungary*

Abstract

Single-phase cubic $Ti_{1-x}Al_xN$ thin films with high Al content are preferred in industrial applications as they combine superior mechanical properties with good oxidation protection. Recently we showed that yttrium, which can further increase the oxidation resistance by the reactive element effect, shifts the cubic stability range of $Ti_{1-x}Al_xN$ to lower AlN mole fractions. Already the addition of 1 at% Y to single-phase cubic $Ti_{0.45}Al_{0.55}N$ promotes the hexagonal phase formation. Based on x-ray diffraction and transmission electron microscopy studies we reveal that DC magnetron sputtering (DC-MS) from $Ti_{0.49}Al_{0.49}Y_{0.02}$ compound targets in Ar-N_2 atmosphere results in the formation of mixed cubic-hexagonal structured $(Ti_{1-x}Al_x)_{1-y}Y_yN$ films, whereas the cubic structure can be stabilized by employing bipolar pulsed magnetron sputtering. This can be correlated to an increase in the Ti/Al ratio of the film and increased ion bombardment with increasing pulse duration, triggered by increases in the plasma electron temperature and ion fluxes. For pulsed DC-MS with 80 kHz and increasing pulse duration from 0 (DC-MS) to 4976 ns the composition of the coatings changes from $Ti_{0.41}Al_{0.57}Y_{0.02}N$ to $Ti_{0.46}Al_{0.52}Y_{0.02}N$ and the structure from a mixed cubic-hexagonal to a single-phase cubic, resulting in hardness increases from 23.5 to 34.6 GPa, respectively.

Keywords: pulsed magnetron sputtering, TiAlYN, structure, chemical composition, hardness

1. Introduction

Plasma-assisted vapour deposition (PVD) techniques allow the formation of supersaturated solid-solution $Ti_{1-x}Al_xN$ with cubic (c) NaCl structure up to AlN mole fractions x ~ 0.7. Exceeding the metastable AlN solubility results in a mixed (NaCl + ZnS-wurtzite) structure, or the films crystallize completely in the hexagonal ZnS-wurtzite (w) modification [1-7]. Cubic - $Ti_{1-x}Al_xN$ films with high Al contents have superior physical, mechanical and chemical properties and show better oxidation resistance than their two-phased, or single-phased hexagonal counterparts and are thus used in a large variety of applications ranging from wear protection of tools and dies to components in aerospace and automotive industries [8-10]. Alloying $Ti_{1-x}Al_xN$ films allows further adjustment of properties and tailoring to their respective needs [11, 12]. Reactive elements such as yttrium are commonly used in materials design to increase oxidation protection of structural and coating materials [13-15], e.g. alloying Y to TiN and $Ti_{1-x-y}Al_xCr_yN$ also improves their mechanical properties [16, 17].

We have recently shown that the addition of yttrium to c-$Ti_{1-x}Al_xN$ shifts the solubility limit to lower Al contents, resulting in mixed cubic-hexagonal or single-phase hexagonal films for Al contents above 52% with decreased mechanical properties [18]. Furthermore, as the hexagonal phase due to its lower packing density has also a lower oxidation resistance than the cubic [19], careful attention needs to be pointed on the structure and phase-development during alloying of c-$Ti_{1-x}Al_xN$ with Al contents close to the metastable solubility limit.

As pulsed DC magnetron sputtering (DC-MS) in the mid-frequency range (20-350 kHz) is a common tool to modify the microstructure of hard nitride coatings and their physical properties [20-24] we studied the effect of asymmetric-bipolar pulsed DC-MS from a compound target on structural and mechanical properties of the deposited $(Ti_{1-x}Al_x)_{1-y}Y_yN$ films. We applied electron probe microanalyses, x-ray diffraction (XRD), and cross-sectional transmission electron microscopy (XTEM) for chemical and structural investigations, and determine the effect of the power supply characteristics on the discharge conditions using Langmuir probe measurements. This allows to investigate the correlation of chemical composition, structure and mechanical properties of the coatings with the modified discharge, plasma and target conditions during pulsed DC-MS compared to DC-MS.

2. Experimental Details

$(Ti_{1-x}Al_x)_{1-y}Y_yN$ thin films were grown on Si(100) in a modified Leybold Z-400 facility by reactive unbalanced magnetron sputtering from a Ø76 mm $Ti_{0.49}Al_{0.49}Y_{0.02}$ compound target (powder metallurgical prepared by PLANSEE GmbH, Lechbruck, Germany, 99.9% purity) in a mixed Ar - N_2 (both with 99.999% purity) glow discharge using a N_2/Ar partial pressure ratio of 0.4 and a working gas pressure of 0.5 Pa. The substrate temperature of 550 °C and DC bias potential of -50 V were kept constant for all deposition runs. The substrates were positioned 5 cm above the target race track. An ENI RPG-50 asymmetric bipolar pulsed power supply, set to provide 400 W in power regulation mode, was used for DC and for pulsed DC magnetron sputtering. Pulsing frequencies f of a +37 V reverse voltage pulse can be varied between 50 and 250 kHz with a positive pulse length t_{rev} variation from 496 ns to a maximum of 8016 ns. The latter is defined as 60% of the duty cycle which itself is the ratio between sputter on-time t_{on} and the overall period ($t_{on}+t_{rev}$).

Coatings with different Ti/Al ratios were produced in DC-mode with the above described deposition settings by adding Ti platelets (4x3x1 mm^3) on the $Ti_{0.49}Al_{0.49}Y_{0.02}$ target race track covering 0.74, 1.48, and 2.15 % of the total target surface.

The microstructure of films was investigated using a Siemens D500 x-ray diffractometer with Cu-Kα radiation in the 2θ range 30—50 deg. in Bragg-Brentano geometry. The coatings microstructure was examined in a Philips CM20 transmission electron microscope interfaced with a NORAN energy dispersive analyzer (EDX) at 200 kV.

The specimens for cross sectional transmission electron microscopy (XTEM) were prepared by mechanical cutting, grinding and ion beam thinning techniques. The specimens embedded into a Ti sheet with a Si single crystal counterpart were thinned mechanically to a thickness of 40 µm. The ion beam thinning was carried out in a Technoorg Linda IV. thinning unit equipped with TELETWIN ion guns working in the 2 – 10 keV ion energy range [25, 26]. The thinning was carried out at glancing incidence ion beam (~3-5°) on both sides of the specimens both under rotation and oscillation mode. The thinning was completed in an other thinning unit equipped with an ion gun working at 300 eV ion energy. By this way the thickness of the damaged surface layer could be decreased.

During scanning electron microscopy (SEM) investigations with a Zeiss EVO 50 microscope the chemical composition of the films was determined by energy dispersive x-

ray analysis (EDX) with an Oxford Instruments INCA EDX unit using metallic Al and Y and a TiN film standard. Quantification of the latter was obtained by Rutherford backscattering spectroscopy as described in Ref. [27].

The hardness (H) was measured by nano-indentation with a CSIRO ultra micro indentation system (UMIS) equipped with a Berkovich-indenter while the modulus (E) was determined from the loading and unloading traces after the Oliver-Pharr method [28]. With respect to a proper statistic at least 50 indents were carried out for each sample with maximum loads ranging from 10 to 45 mN to keep the indentation depth below 10% of the coating thickness.

The voltage characteristics applied to the target by the ENI RPG-50 in DC and pulsed DC mode were recorded with a Tektronix HCTEK321 oscilloscope equipped with a PMK PMV10000-3 high voltage probe. Plasma analyses are carried out with a standard Hiden ESP Langmuir wire probe. The pulsing induced changes in sputter yield Y_s and emission angle α_s of sputtered Ti and Al species are estimated with SRIM, a program package available online which calculates the stopping and range of ions with a given energy in matter [29-31]. Ar^+ and N_2^+ were chosen as projectile ions. To exclude ion transmission the sputtering of 1 µm $Ti_{0.5}Al_{0.5}$ component layers was simulated using $5 \cdot 10^5$ ions at normal incidence (90°) and 400, 900, and 1500 eV ion energies.

3. Results and Discussion

3.1 Process Characterization

Deposition parameter dependent factors like ion energy (E_i), ion flux (J_i), and metal flux (J_{Me}) of species arriving on the substrate have a strong influence on the microstructure of nitride films [32-34]. The parameters varied here (which have an effect on E_i, J_i, and J_{Me}) are the reverse voltage pulse length t_{rev} and frequencies during pulsed DC-MS. Typical target voltage waveforms for DC- and 80 kHz pulse DC-MS with t_{rev} = 496, 1616, 3056, and 4979 ns are given in Fig 1. When the polarity of the target voltage changes, strong overshoots occur in the onset of t_{on} and t_{rev}. Comparable target voltage waveforms are reported in literature for bipolar pulsing and can be related to the nature of the power supply [35-40]. The observed fast fluctuation (MHz frequency) of target voltage above +200 V at the onset of t_{rev} is reported to be accompanied by strong increases in the target current [35-37, 39]. After this MHz ringing the reverse voltage flattens to +37 V during

t_{rev}. On polarity changes the target voltage overshoots -350 V observed during DC mode for the 400 power regulation and the used $Ti_{0.49}Al_{0.49}Y_{0.02}$ compound target, see Fig 1. Thereby the target peak voltage reaches -700 V for t_{rev} = 496 ns and increases to -1450 V for increasing t_{rev} to 4976 ns at the onset of t_{on} and levels off to about -350 V.
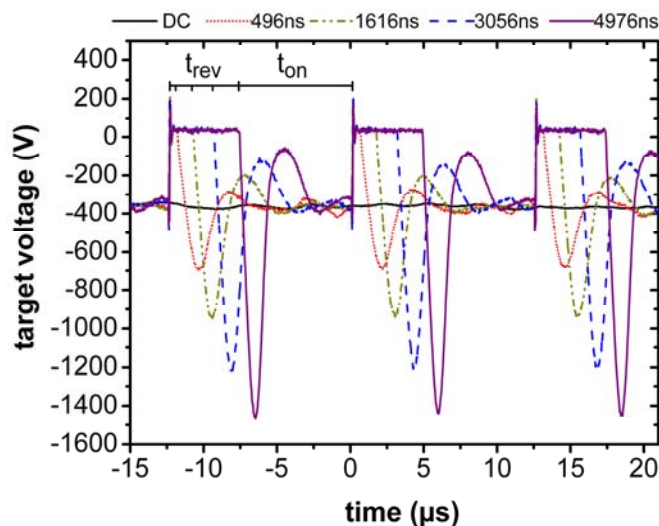

Fig.1 Target voltage wave forms for DC-MS and pulsed DC-MS with 80 kHz pulse and t_{rev} = 496 ns (dotted), 1616 ns (dash dotted), 3056 ns (dashed), and 4976 ns (solid).

Langmuir wire probe measurements yield an increase in electron temperature T_e from 3.6 eV for DC discharge to 4.9 eV for 80 kHz pulsed DC discharge with t_{rev} = 4976 ns. Increases are found to be linear with increasing reverse voltage time t_{rev} and reach a maximum T_e of ~5 eV for the smallest duty cycle of 60%, independent of the used frequencies. The plasma potential V_P decreases with increasing positive pulse length from -7.2 V for DC-MS to -1.4 V for pulsed DC-MS at 80 kHz and t_{rev} = 4976 ns. Consequently, the energy of the impinging ions E_i on the substrate or growing film by applying a bias potential V_B of -50 V increases according to $E_i = e|V_B - V_P|$ from 42.8 to 48.6 eV when changing from DC-MS to pulsed DC-MS with 80 kHz and t_{rev} = 4976 ns [32, 34, 41].

Although our Langmuir data are not time resolved and thus give time averaged values, the general trends observed are fully in-line with literature. Electron heating through discharge pulsing is shown in Refs. [35, 36, 38, 42] to occur through stochastic heating caused by MHz ringing of the target voltage, as observed during our studies at the onset of t_{rev}, see Fig. 1. These increases in T_e and electron density lead to increases in ion fluxes. J_i increases with increasing reverse voltage time t_{rev} for all investigated frequencies.

Furthermore, from the pulsing induced reduction of sputter-on duty time with increasing t_{rev} (or decreasing duty cycle) the sputter rate decreases from 44 nm/min for the DC-MS coating to 38, 37, 33, and 28 nm/min for 80 kHz pulsed DC-MS films deposited with t_{rev} = 496, 1616, 3056, and 4979 ns. Hence, we found that the metal flux J_{Me} arriving on the substrate during pulsed DC-MS decreases linearly with increasing t_{rev} and thus these reductions can be accounted for by the shorter magnetron power on time (i.e., lower duty cycle). Consequently, as J_i increases and J_{Me} decreases with increasing t_{rev}, the ion-to-metal flux ratio J_i/J_{Me} increases with t_{rev}. In the case of a pulsing frequency of 80 kHz, J_i/J_{Me} increases from ~0.44 to 1.02 for increases in t_{rev} from 0 (DC-MS) to 4976 ns, respectively.

3.2 Coating Characterisation

3.2.1 Structure

Figures 2a, b, and c present XRD patterns of our films deposited by DC-MS and pulsed DC-MS from the $Ti_{0.49}Al_{0.49}Y_{0.02}$ target. The coating prepared by DC-MS has a binary composition of cubic and hexagonal phases as described in detail in Ref. [18]. The intensities and integrated peak areas of the cubic (200) reflex increase whereas those of the hexagonal (100) and (002) reflexes (2Θ = 32.48 and 34.06) decrease with increasing frequency from 80 to 250 kHz at a constant reverse voltage pulse length t_{rev}=1616 ns and consequently duty cycles of 87 – 60%, indicating increasing cubic and decreasing hexagonal phase fractions, respectively (see Fig. 2a). These changes are even more pronounced for decreasing frequencies from 250 to 80 kHz with increasing t_{rev} from 1616 to 4976 ns at a constant smallest possible duty cycle of 60% (Fig. 2b). The coating prepared at 80 kHz and t_{rev} = 4976 ns shows no hexagonal reflexes and is cubic <200> textured. The results presented in Figs. 2a and b suggest that small frequencies and short duty cycles –i.e. long reverse voltage durations t_{rev} – promote the growth of a <200> textured single-phase cubic $(Ti_{1-x}Al_x)_{1-y}Y_yN$ film. This is shown in Fig. 2c presenting XRD patterns of coatings prepared at a constant frequency of 80 kHz and pulse lengths between 496 to 4976 ns coupled with duty cycles from 96 to 60%, respectively. The XRD patterns of the coatings prepared by pulsed DC-MS with short duty cycles of 75 and 60% and long pulse length of 3056 and 4976 ns reveal only the (200) cubic reflex, indicating a single phased cubic $(Ti_{1-x}Al_x)_{1-y}Y_yN$ film. With shorter t_{rev} hexagonal reflexes can be detected revealing a two-phased microstructure.

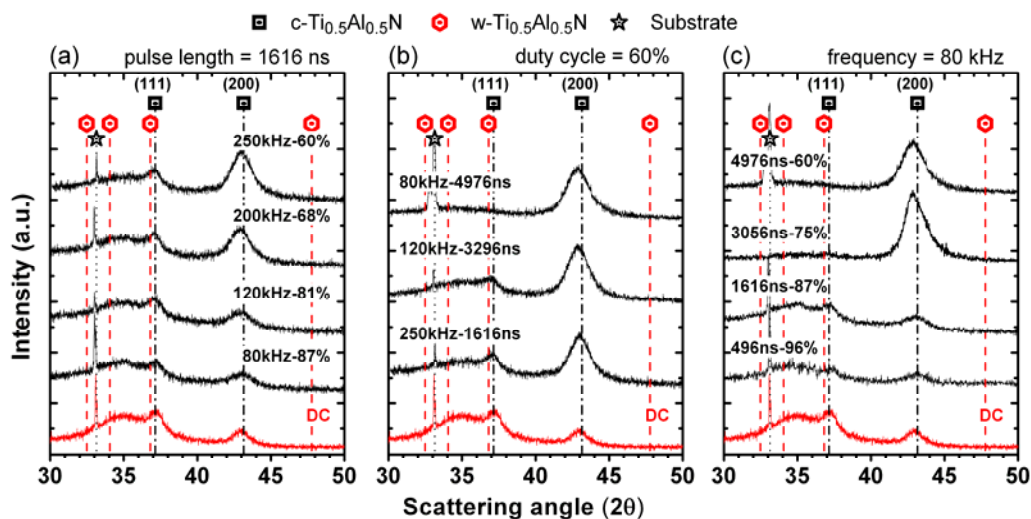Fig.2 XRD patterns of $(Ti_{1-x}Al_x)_{1-y}Y_yN$ films prepared by DC-MS and pulsed DC-MS with a constant pulse length t_{rev}=1616 ns and various frequencies (a) constant duty cycle of 60% and various frequencies (b), and a constant frequency of 80 kHz (c) with various duty cycle.

3.2.2 Morphology

To corroborate the above presented XRD results, films produced by pulsed DC-MS with 80 kHz and various pulse lengths t_{rev} were investigated by XTEM analyses and compared to the DC-MS coating.

The cross-sectional bright-field (BF) and dark-field (DF) images of the DC-MS coating is presented in Figs. 3a and b, respectively. Close to the substrate the coating exhibits a dense V-shaped columnar structure with a growth direction perpendicular to the substrate surface, according to zone T [43, 44]. At a distance of ~300 nm from the interface the growth direction is tilted by ~32° to the substrate normal. Close to the coating surface the column width is ~40 nm. Figure 3c is a typical selected area electron diffraction pattern (SAED) featuring strong wurtzite-type hexagonal and NaCl-type cubic reflexes. The hexagonal phase has a <002> texture while the coexisting cubic phase is <111> textured, corresponding to the XRD investigations of the DC-MS film, compare Fig. 2.

XTEM BF images with respective SAED patterns of coatings prepared by pulsed DC-MS with 80 kHz and t_{rev} = 496, 1616, 3056, and 4976 ns are presented in Figs. 4 a–d, respectively. Coatings prepared at t_{rev} = 496, 1616, and 3056 ns exhibit a morphology of perpendicular growth direction in the interface near region and a tilted growth direction in the surface near region corresponding to the film prepared by DC-MS, while at t_{rev} = 4976 ns no region of tilted columns can be observed.
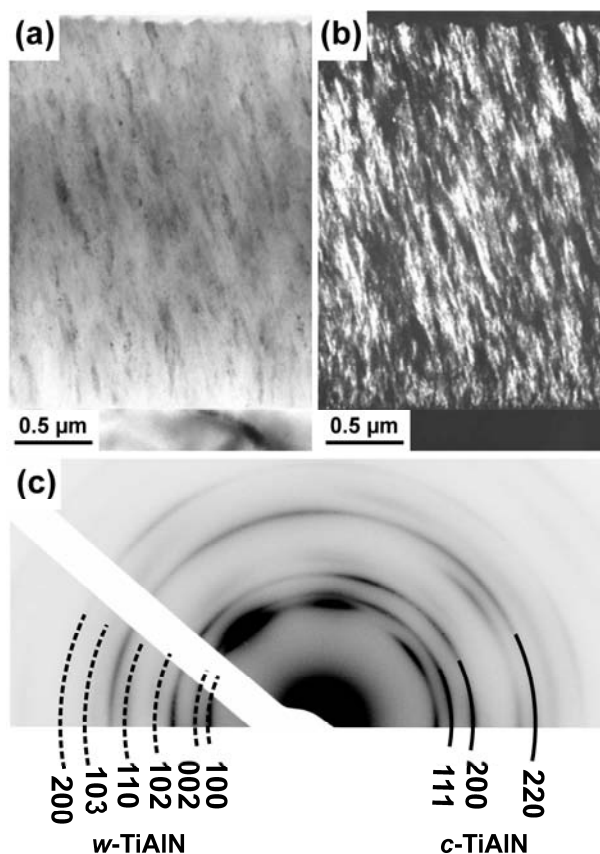
Fig.3 (a) Bright-field and (b) annular dark-field XTEM image of $(Ti_{1-x}Al_x)_{1-y}Y_yN$ prepared by DC-MS (Ti/Al = 0.72). (c) SAED with standard diffraction rings as calculated in Ref. [18] for cubic- (solid) and wurtzite type $Ti_{0.5}Al_{0.5}N$ (dashed).

With increasing pulse length t_{rev} from 496 to 1616 to 3056 ns the distance from the interface to the onset of tilted growth increases from ~600 to ~650 to ~1000 nm, respectively. For these coatings the interface near region with a perpendicular growth direction is dominated by NaCl cubic <200> textured phases and a zone T microstructure. The surface near regions with a tilted growth direction are composed of <111> textured cubic and <002> textured hexagonal phases. The SAED investigations suggest linked orientation dependence of the cubic and hexagonal phases as indicated in Fig. 5. In the SAED of the upper part of the DF XTEM (Fig. 5b) a clear orientation relation between hexagonal <002> and cubic <111> is present and indicated by the arrow. Further the SAED of the lower part show no cubic <200> texture but the (200) reflections are related to the <111> texture.

The results obtained by XTEM and SAED are in excellent agreement to the XRD findings (Fig. 2c) indicating decreasing hexagonal phase fraction with increasing t_{rev} for 80 kHz pulsed DC-MS. Figure 4 furthermore suggests that the angle of the tilted growth decreases with decreasing hexagonal phase fraction.

Generally, the growth of tilted columnar structures in vapour deposition is reported in obliquely deposited films when columnar grains composing the films incline towards the vapour flux [45]. There, the empirical tangent rule can be applied to estimate the tilting angle α of grown columns from a sputtering source positioned at the angle θ [46]:

$$\tan \alpha = \tfrac{1}{2} \tan \theta .$$ (1)

Hence, for 35° tilted columns the sputtering source has to be at an angel of ~50°, which clearly is not possible in a parallel arrangement between substrate and target when the substrates face the target race track, see experimental section.
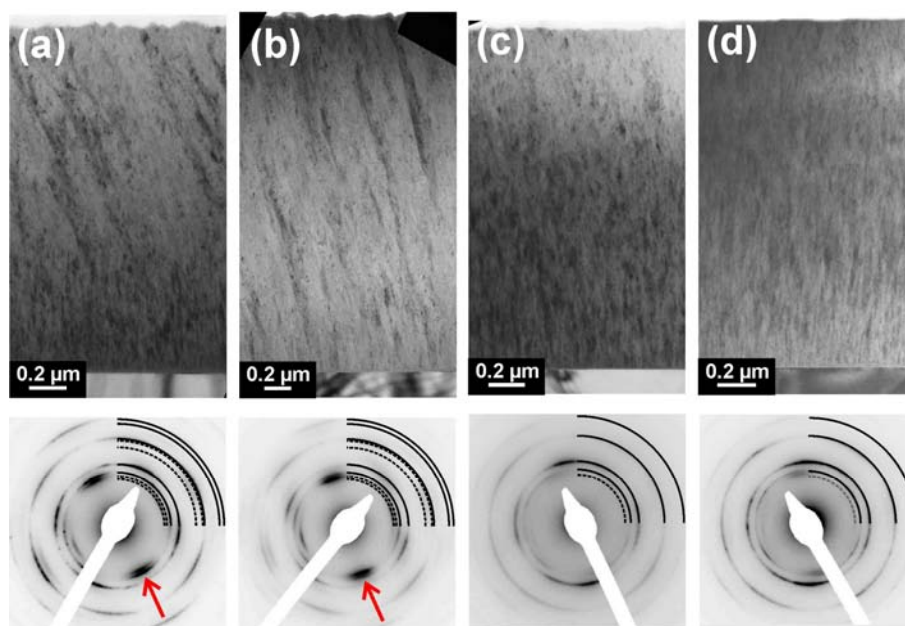
Fig.4 Bright-field XTEM images of $(Ti_{1-x}Al_x)_{1-y}Y_yN$ coatings prepared with pulsed DC-MS using a frequency of 80 kHz and t_{rev} of 496 ns (a), 1616 ns (b), 3056 ns (c) and 4976 ns (d). At the bottom the respective SAED patterns are given with standard diffraction rings for cubic- (solid) and wurtzite type $Ti_{0.5}Al_{0.5}N$ (dashed) as calculated in Ref. [18].

For texture formation in magnetron sputtered TiN films basic thermodynamic models are based on the fact that the formation of a particular crystallographic orientation is determined by the need for a minimization of the surface energy and the accumulated strain energy [47]. According to these models, the texture formation at small thicknesses is governed by the surface energy minimization, whereas at increasing film thicknesses the main factor influencing the texture is the accumulated strain-energy, which increases linearly with thickness [48, 49]. Thus, for TiN a <200> texture can be expected at small thicknesses, as the {200} planes have the lowest surface energies [50-53]. Refs. [54, 55]

report for TiN an anisotropy of the elastic moduli E with $E_{200}<E_{220}<E_{111}$ and hence the accumulated strain energy U decreases from <200> to <220> to <111> textured films. Therefore, starting from some critical thickness during film growth a transition from <200> to <111> texture occurs. This transition was found at thicknesses ranging between ~200 and 1500 nm depending on sputter parameters and substrate material [48, 54, 56].
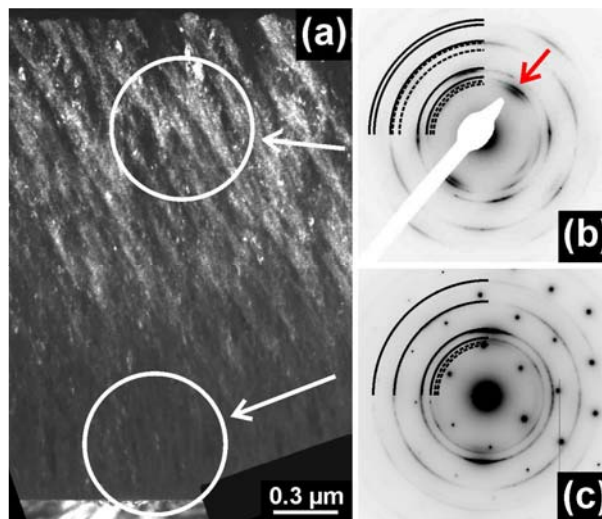

Fig.5 (a) Dark-field XTEM image of a $(Ti_{1-x}Al_x)_{1-y}Y_yN$ coating prepared by prepared by pulsed DC-MS using a frequency of 80 kHz and t_{rev} of 496 ns. SAED with standard diffraction rings as calculated in Ref. [18] for cubic- (solid) and wurtzite type $Ti_{0.5}Al_{0.5}N$ (dashed) for the surface zone (b) and the interface near area (c).

A comparable trend is observed in our films where the interface-near regions are dominated by <200> textured cubic phases. At a certain thickness we also observe <111> textured cubic phases. However, this is accompanied with the hexagonal <002> phases and tilting of growth direction, see Figs 4 and 5. Kutschej et. al. [5] also observed a tilted columnar growth for $Ti_{1-x}Al_xN$ coatings for the mixed cubic and hexagonal phase composition.

Furthermore, it is reported that within an epitaxial multilayer arrangement between cubic TiN and hexagonal AlN the cubic (111) TiN planes are tilted by ~20° from hexagonal [001] AlN direction [57]. The crystallographic relation for an epitaxial matching between cubic TiN and hexagonal AlN lattices can be described as [57, 58]:

$$-\{111\}_{TiN}\langle 110\rangle_{TiN}\left\|\{002\}_{AlN}\langle 110\rangle_{AlN}\right..$$

This is the orientation dependence in our films between cubic and hexagonal phases. Therefore, we propose that the tilted columnar growth, which is only observed in the

cubic-hexagonal binary phase region with <111> textured cubic phases, is the result of the hexagonal phase formation.

Additionally, the hexagonal phase formation benefits from the higher mean diffusion length of Al on cubic (100) surfaces compared to (111), as it is shown for Ti on TiN and the lower absorption energy of Al compared to that of Ti on TiN [53, 59, 60]. Consequently, as soon as cubic (200) and (111) grains coexist, surface diffusion leads to a preferential cubic (111) growth and, combined with the above orientation dependence, to the nucleation and growth of (002) hexagonal crystals due to the faster Al diffusion compared to Ti.

As shown in Refs. [32, 34] for $Ti_{0.5}Al_{0.5}N$ already small increases in J_i/J_{Me} from 1.0 to 1.8 at a constantly low ion energy E_i of 20 eV lead to a change from <111> to <200> textured columns. This is also in agreement with our observation of increasing thickness of the <200> orientated single-phase cubic interface-near region with increasing reverse voltage time t_{rev} and accompanied by increasing J_i/J_{Me}, see Fig. 4.

In addition, small changes in the chemical composition of these coatings can influence microstructure and phase composition sensitively, especially at compositions close to a metastable solubility limit [2, 5, 18]. In Ref. 16 we showed that a small addition of only y=2.5 at% Y to the metastable sub-lattice of DC-MS $(Ti_{1-x}Al_x)_{1-y}Y_yN$ reduces the metastable solubility limit of the cubic structure from >55% to <52% Al leading to binary cubic-hexagonal phased or even single-phased hexagonal $(Ti_{1-x}Al_x)_{1-y}Y_yN$ films.

3.2.3 Chemical Composition

DC-MS of a $Ti_{0.49}Al_{0.49}Y_{0.02}$ target in an Ar/N_2 discharge with our deposition conditions results in the formation of stoichiometric nitride films with a chemical composition of the metal sublattice of Ti = 41 at%, Al = 56.6 at%, and Y = 2.4 at%. Consequently, the Ti/Al ratio of the films with ~0.72 is smaller than of the used target with 1. For magnetron sputtered films higher Al and lower Ti contents, as in the respective target are generally reported, see Refs. [5, 61]. By applying pulsed DC-MS the Ti/Al ratio of the films increases from 0.72 to 0.89 – Ti = 45.9 at%, Al = 51.7 at% – almost linearly with increasing pulse length t_{rev} from 0 (DC-MS) to 4979 ns, independent –within the error of the measurement- of the used frequencies of 50, 80, 120, and 250 kHz, as shown in Fig. 6. Almost no changes are observed for Y which is ~2.5 at%. Consequently, the coating

composition approaches the target composition with increasing t_{rev} and hence increasing J_i/J_{Me}.
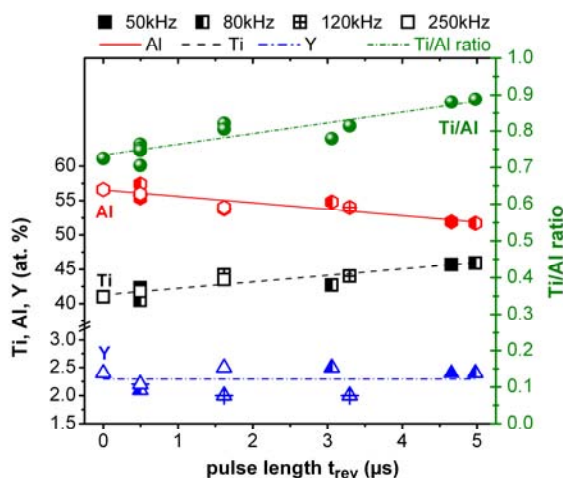

Fig.6 Chemical composition of the metal sublattice and Ti/Al ratio versus reverse voltage time t_{rev}.

The influences of pulse parameters on sputter yield Y_S and angle of sputtered species α_S are estimated by SRIM. The energies of the working gas ions, Ar^+ and N_2^+, are derived from the peak voltages measured during bi-polar pulsing (Figure 1). Thus, the ion energies were set to 400 eV for DC-MS, and 900 and 1500 eV for pulsed DC-MS at t_{rev} = 1616 and 4979 ns, respectively. For DC-MS the sputter yields with Ar^+ and N_2^+ ($Y_{S, Ar}$ and $Y_{S, N2}$) are 3.9 and 3.3 for Al, and 3.6 and 3.1 for Ti, respectively. These values are comparable to those reported for single component targets [62-64]. Hence, the obtained sputter-yields for Ar^+ and N_2^+ suggest Ti/Al ratios of 0.85 and 0.86, respectively, and a metal sublattice composition of 54 at% Al and 46 at% Ti. With increasing ion energy the sputter yield for Ti increases stronger than that for Al. The Ti/Al ratios are 0.86 and 0.88 for sputtering with 900 eV and 1500 eV Ar ions and 0.89 and 0.90 for sputtering with 900 eV and 1500 eV N_2 ions.

Generally, atoms are sputtered from the target in a range of directions proportional to a cosine distribution including the angel of incidence [65, 66]. Thus, a number of sputtered species does not reach the substrate. For our deposition arrangement the threshold angle from the target normal for atoms to impinge on the substrate is 25°. Hence, ~15% and ~21% of the Al and Ti atoms sputtered from a $Ti_{0.5}Al_{0.5}$ compound target are lost with 400 eV Ar^+. Using 400 eV N_2^+ as sputtering species ~17% Al and ~22% Ti would be lost. Consequently, the different losses for Ti and Al atoms suggest a Ti/Al ratio of ~0.93 at the substrate. Together, the different sputter yields and losses for Ti and Al atoms suggest a

Ti/Al ratio of ~0.79 for sputtering a $Ti_{0.5}Al_{0.5}$ compound target with Ar^+ ions having 400 eV. This value is in perfect agreement to the observed Ti/Al film ratio of 0.79 ± 0.02 obtained during DC sputtering of a $Ti_{0.5}Al_{0.5}$ target, as reported in Refs. [5, 18].

Increasing the ion energy to 1500 eV results in a loss of 17 and 22% of Al and Ti and 18 and 23 % of Al and Ti using Ar^+ and N_2^+ for sputtering, respectively. Consequently, the Ti/Al ratios of film forming species would increase from 0.93 to 0.94 with increasing ion energies from 400 to 1500 eV.

Both SRIM results, the sputter yield and the angular distribution of sputtered species, give increasing Ti/Al ratios of the film forming metal atoms with increasing working gas ion energies, i.e. increasing reverse voltage pulse lengths t_{rev} during bipolar-pulsed sputtering. Therefore, these results are in good agreement to the changes in chemical composition observed during pulsed DC-MS.
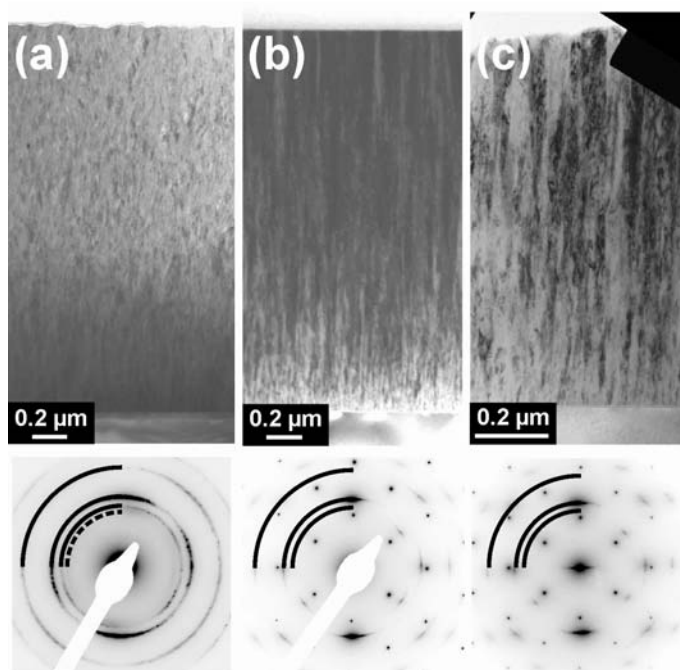

Fig.7 Bright-field XTEM images of films with Ti/Al ratios of (a) 0.88, (b) 1.0, and (c) 1.18 DC-MS from $Ti_{0.49}Al_{0.49}Y_{0.02}$ targets with added Ti platelets covering 0.74, 1.48, and 2.15% of the target surface. At the bottom the respective SAED patterns are given with standard diffraction rings for cubic- (solid) and wurtzite type $Ti_{0.5}Al_{0.5}N$ (dashed), as calculated in Ref. [18].

To separate the effects of pulsing induced plasma variation on microstructure and phase composition from the influence of a modified chemical composition, $(Ti_{1-x}Al_x)_{1-y}Y_yN$ films were prepared by DC-MS at 0.72, 0.88, 1.0, and 1.18 Ti/Al ratio. This is obtained by covering 0, 0.74, 1.48, and 2.15% of the $Ti_{0.49}Al_{0.49}Y_{0.02}$ target surface with small Ti platelets, placed on the race track. XTEM BF images with respective SAED patterns of the

coatings are presented in Figs. 3a and c for Ti/Al = 0.72 and Figs. 7a, b, and c, for Ti/Al = 0.88, 1.0, and 1.18, respectively. The coatings with Ti/Al ≥ 1.0 (Figs. 7a, b, and c) have a columnar zone T microstructure with a growth direction perpendicular to the substrate surface, and the SAED investigation reveals only single phase cubic NaCl structures. Traces of wurtzite type hexagonal phase can be detected in the surface zone of the coating with Ti/Al = 0.88. This film grows columnar and single-phase cubic with <200> orientation in the substrate near region up to a thickness of ~1.5 µm. Corresponding to the coatings produced by pulsed DC-MS hexagonal phases are present in the surface near region.

The main data of the $(Ti_{1-x}Al_x)_{1-y}Y_yN$ films prepared by the two deposition methods and investigated by XTEM (see Figs. 3, 4, 5, and 7) are summarized in Table 1.

	Composition	Ti/Al	Sputtering power	Pulse frequency	Pulse length	Target	TEM images
DC-MS	$Ti_{0.41}Al_{0.57}Y_{0.02}N$	0.72	400 W	–	–	$Ti_{0.49}Al_{0.49}Y_{0.02}$	Fig. 3
	$Ti_{0.46}Al_{0.52}Y_{0.02}N$	0.88	400 W	–	–	$Ti_{0.49}Al_{0.49}Y_{0.02}$ + 0.74%Ti	Fig. 7a
	$Ti_{0.49}Al_{0.49}Y_{0.02}N$	1.0	400 W	–	–	$Ti_{0.49}Al_{0.49}Y_{0.02}$ + 1.5%Ti	Fig. 7b
	$Ti_{0.53}Al_{0.45}Y_{0.02}N$	1.18	400 W	–	–	$Ti_{0.49}Al_{0.49}Y_{0.02}$ + 2.15%Ti	Fig. 7c
pulsed DC-MS	$Ti_{0.41}Al_{0.57}Y_{0.02}N$	0.72	400 W	80kHz	496 ns	$Ti_{0.49}Al_{0.49}Y_{0.02}$	Fig. 4a, Fig. 5
	$Ti_{0.44}Al_{0.54}Y_{0.02}N$	0.81	400 W	80kHz	1616 ns	$Ti_{0.49}Al_{0.49}Y_{0.02}$	Fig. 4b
	$Ti_{0.43}Al_{0.55}Y_{0.02}N$	0.78	400 W	80kHz	3056 ns	$Ti_{0.49}Al_{0.49}Y_{0.02}$	Fig. 4c
	$Ti_{0.46}Al_{0.52}Y_{0.02}N$	0.88	400 W	80kHz	4976 ns	$Ti_{0.49}Al_{0.49}Y_{0.02}$	Fig. 4d

Table 1 Summarized composition and deposition data of $(Ti_{1-x}Al_x)_{1-y}Y_yN$ films prepared by DC-MS and pulsed DC-MC which are investigated in-detail by TEM. Note: the percentage of Ti increase at the target is related to the total target surface area not the chemical composition.

3.2.4 Hardness and Modulus of Indentation

Figures 8a and b show the hardness (H) and modulus (E) of indentation of our films prepared by DC-MS and pulsed DC-MS as a function of pulse length t_{rev} and the Ti/Al ratio, respectively. Starting from H = 23.5±1.4 GPa for the $Ti_{0.41}Al_{0.57}Y_{0.02}N$ film (Ti/Al = 0.72), prepared by DC-MS, with a binary cubic-hexagonal microstructure, the hardness increases with increasing Ti/Al ratio and hence decreasing frequencies and increasing reverse voltage pulse lengths t_{rev} during pulsed DC-MS. The highest hardness values of 31.8±2.1 GPa and 34.3±4.3 GPa are obtained for the coatings prepared with the longest

pulse length at frequencies of 80 kHz and 50 kHz, respectively. These films have Ti/Al ratios of 0.89 and 0.88 and are single-phase cubic. The DC-MS deposited $(Ti_{1-x}Al_x)_{1-y}Y_yN$ coating with almost identical chemical composition has a similar hardness of 31.5±1.0 GPa. The modulus of indentation shows a comparable dependence on the reverse voltage pulse lengths t_{rev} and hence Ti/Al ratio and increases from ~304 GPa with Ti/Al = 0.7 to ~398 GPa with Ti/Al = 0.89.
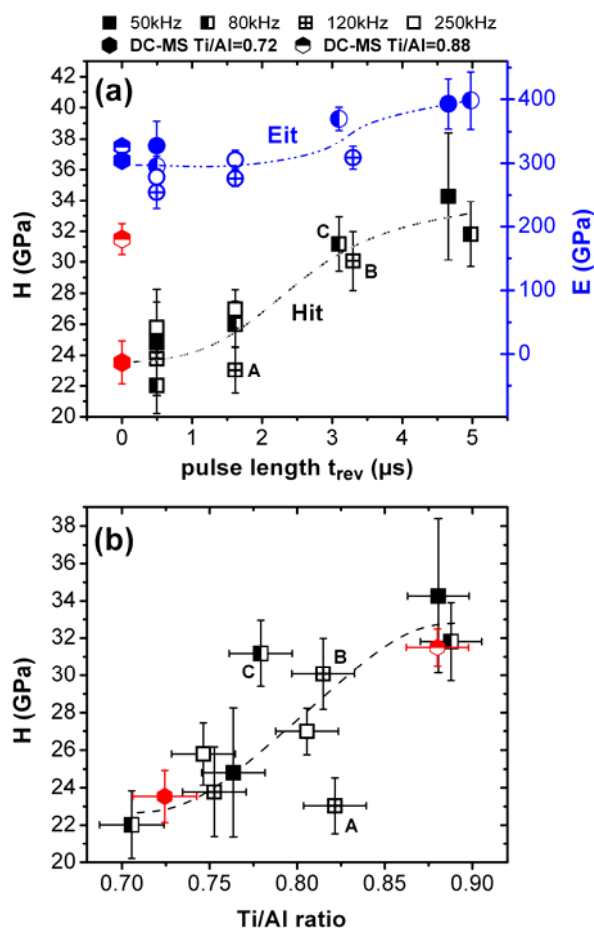

Fig. 8 Hardness and modulus of $(Ti_{1-x}Al_x)_{1-y}Y_yN$ films prepared by pulsed DC-MS with f = 50, 80, 120, and 250 kHz as a function of reverse voltage time t_{rev} (a) and Ti/Al ratio (b). Two films prepared by DC-MS are added for comparison.

The variations in H and E with pulse length are due to the linked changes in microstructure and hexagonal phase content. With decreasing hexagonal phase fraction (hence increasing Ti/Al ratio) H and E increase and are maximum for the single-phase cubic film at Ti/Al = 0.88. This is in agreement to the commonly observed trend that hexagonal $Ti_{1-x}Al_xN$ exhibits lower bulk, elastic, and shear moduli compared to the respective cubic phase [5, 6, 11, 67].

Comparing Figs. 8a and b reveals that not only the chemical composition but also the pulsing induced variation of deposition parameters have a strong influence on microstructural and thus mechanical properties. Coatings produced at a frequency of 120 kHz and t_{rev} of 1616 and 3296 ns, labelled with A and B in Fig. 8, have hardnesses of 23.0±1.5 and 30.1±1.9 GPa, although having similar Ti/Al ratios of 0.82±0.02 and 0.81±0.02, respectively. The film prepared by pulsed DC-MS with f = 80 kHz and t_{rev} = 3096 ns, labelled with C in Fig. 8, with an even higher Al content with Ti/Al = 0.77±0.02 still has a predominantly (200) cubic microstructure, as shown in Figs. 2c and 4c. Therefore this film has a hardness value of 31.2±1.8 GPa, which is higher than the general trend in the H vs. Ti/Al graph (Fig. 8b). These results clearly demonstrate that both, the variation in chemical composition and the changed plasma conditions, like plasma electron-temperature and ion-fluxes, influence the microstructure of our $(Ti_{1-x}Al_x)_{1-y}Y_yN$ films and hence their hardness and modulus.

4. Conclusions

$(Ti_{1-x}Al_x)_{1-y}Y_yN$ films prepared by reactive DC-MS of a $Ti_{0.49}Al_{0.49}Y_{0.02}$ target, grow in a mixed cubic-hexagonal phase composition. Applying bi-polar pulsed DC-MS with low frequencies and long positive pulse durations results in single-phase cubic $(Ti_{1-x}Al_x)_{1-y}Y_yN$ films having excellent mechanical properties. This modification in phase-composition can be accounted for by modified plasma conditions with increases found in the electron temperature T_e and ion-to-metal ratio J_i/J_{Me} with increasing t_{rev}. These changes are accompanied by an increase in Ti/Al ratio.

In addition to the modified phase-composition of the coatings also their morphology is influenced by applying bi-polar pulsed DC magnetron sputtering. The film prepared by DC-MS, having a Ti/Al ratio of 0.72, shows a <200> textured cubic structure at the interface near region with a growth direction perpendicular to the substrate surface. With increasing coating thickness the texture changes into a mixed <200>-<111> with a concomitant formation of the hexagonal phase fraction and tilting of the growth direction. Increasing t_{rev} results in a stabilization of the cubic <200> texture to larger thicknesses and an associated decrease in hexagonal phase content.

Based on our results we can conclude that by using bi-polar pulsed magnetron sputtering of a $Ti_{0.49}Al_{0.49}Y_{0.02}$ target with 80 kHz and 3096 ns a single-phase <200> textured film with

Ti/Al = 0.78 can be prepared with hardness and modulus of indentation of 31.18 and 369.71 GPa, respectively. Using the same deposition conditions during DC-MS would result in mixed cubic-hexagonal coating with Ti/Al = 0.72 and a hardness and modulus of 23.54 and 304.41 GPa, respectively.

Acknowledgments

References

[1]   R. Cremer, M. Witthaut, D. Neuschütz, in: W.D. Cho, H.Y. Sohn (Eds.), Value-Edition-Metallurgy, The Minerals & Metals Society, Warrendale, PA, 1998, p. 249.

[2]   A. Hörling, L. Hultman, M. Oden, J. Sjolen, L. Karlsson, J. Vac. Sci. Technol., A 20/5 (2002) 1815.

[3]   A. Kimura, M. Kawate, H. Hasegawa, T. Suzuki, Surf. Coat. Technol. 169-170 (2003) 367.

[4]   P.H. Mayrhofer, et al., Appl. Phys. Lett. 83/10 (2003) 2049.

[5]   K. Kutschej, P.H. Mayrhofer, M. Kathrein, P. Polcik, R. Tessadri, C. Mitterer, Surf. Coat. Technol. 200/7 (2005) 2358.

[6]   P.H. Mayrhofer, D. Music, J.M. Schneider, J. Appl. Phys. 100/9 (2006) 094906.

[7]   P.H. Mayrhofer, D. Music, J.M. Schneider, Appl. Phys. Lett. 88/7 (2006) 071922.

[8]   W.D. Münz, J. Vac. Sci. Technol., A 4/6 (1986) 2717.

[9]   A. Hörling, L. Hultman, M. Oden, J. Sjolen, L. Karlsson, Surf. Coat. Technol. 191/2-3 (2005) 384.

[10]   V.H. Derflinger, A. Schutze, M. Ante, Surf. Coat. Technol. 200/16-17 (2006) 4693.

[11]   S. PalDey, S.C. Deevi, Materials Science and Engineering A 342/1-2 (2003) 58.

[12]   K. Kutschej, P.H. Mayrhofer, M. Kathrein, P. Polcik, C. Mitterer, Surf. Coat. Technol. 188-89 (2004) 358.

[13]   A. Gil, B. Rajchel, N. Zheng, W.J. Quadakkers, H. Nickel, J. Mater. Sci. 30/22 (1995) 5793.

[14]   B.A. Pint, Oxidation of Metals 45/1-2 (1996) 1.

[15]   H.J. Grabke, M. Schütze (Eds.), Oxidation of Intermetallics, Wiley-VCH GmbH, Weinheim, 1998.

[16]   L.A. Donohue, et al., Vacuum 55/2 (1999) 109.

[17]   W.S. Choi, S.K. Hwang, C.M. Lee, J. Vac. Sci. Technol., A 18/6 (2000) 2914.

[18]   M. Moser, P.H. Mayrhofer, Scripta Mater 57/4 (2007) 357.

[19]   B.Y. Man, L. Guzman, A. Miotello, M. Adami, Surf. Coat. Technol. 180-181 (2004) 9.

[20]   P.J. Kelly, C.F. Beevers, P.S. Henderson, R.D. Arnell, J.W. Bradley, H. Bäcker, Surf. Coat. Technol. 174-175 (2003) 795.

[21]   J.W. Lee, S.K. Tien, Y.C. Kuo, Thin Solid Films 494/1-2 (2006) 161.

[22]   H.C. Barshilia, K.S. Rajam, Surf. Coat. Technol. 201/3-4 (2006) 1827.

[23]   M. Audronis, P.J. Kelly, A. Leyland, A. Matthews, Thin Solid Films 515/4 (2006) 1511.

[24]   J. Vlcek, A.D. Pajdarova, J. Musil, Contributions to Plasma Physics 44/5-6 (2004) 426.

[25] A. Barna, B. Pécz, M. Menyhárd, Micron 30/3 (1999) 267.

[26] A. Barna, MRS Conf. Ser. Vol. 254 (1991) 3.

[27] P.H. Mayrhofer, F. Kunc, J. Musil, C. Mitterer, Thin Solid Films 415/1-2 (2002) 151.

[28] G.M.P.W.C. Oliver, J. Mater. Res. 7 (1992) 1564.

[29] http://www.srim.org/, Vers. 2006.

[30] J.P. Biersack, L. Haggmark, Nucl. Instr. and Meth. 174 (1980) 257.

[31] J.F. Ziegler, J.P. Biersack, U. Littmark, The Stopping and Range of Ions in Matter, Pergamon Press, New York, 1996.

[32] F. Adibi, I. Petrov, J.E. Greene, L. Hultman, J.E. Sundgren, J. Appl. Phys. 73/12 (1993) 8520.

[33] L. Hultman, J.E. Sundgren, J.E. Greene, D.B. Bergstrom, I. Petrov, J. Appl. Phys. 78/9 (1995) 5395.

[34] I. Petrov, P.B. Barna, L. Hultman, J.E. Greene, J. Vac. Sci. Technol., A 21/5 (2003) S117.

[35] J.W. Bradley, H. Bäcker, P.J. Kelly, R.D. Arnell, Surf. Coat. Technol. 142-144 (2001) 337.

[36] J.W. Bradley, H. Bäcker, P.J. Kelly, R.D. Arnell, Surf. Coat. Technol. 135/2-3 (2001) 221.

[37] H. Bäcker, P.S. Henderson, J.W. Bradley, P.J. Kelly, Surf. Coat. Technol. 174-175 (2003) 909.

[38] J.W. Lee, J.J. Cuomo, M. Bourham, J. Vac. Sci. Technol., A 22/2 (2004) 260.

[39] T. Moiseev, D.C. Cameron, J. Vac. Sci. Technol., A 23/1 (2005) 66.

[40] M. Audronis, P.J. Kelly, R.D. Arnell, A. Leyland, A. Matthews, Surf. Coat. Technol. 200/5-6 (2005) 1366.

[41] I. Petrov, F. Adibi, J.E. Greene, W.D. Sproul, W.D. Münz, J. Vac. Sci. Technol., A 10/5 (1992) 3283.

[42] D.A. Glocker, J. Vac. Sci. Technol., A 11 (1993) 2989.

[43] J.A. Thornton, J. Vac. Sci. Technol. 11/4 (1974) 666.

[44] P.B. Barna, M. Adamik, Thin Solid Films 317/1-2 (1998) 27.

[45] D.L. Smith, Thin-Film Deposition: principle and practice, McGraw-Hill, New York, 1995.

[46] J.M. Nieuwenhuizen, H.B. Haanstra, Philips Tech. Rev. 27 (1966) 87.

[47] I. Iordanova, P.J. Kelly, R. Mirchev, V. Antonov, Vacuum 81/7 (2007) 830.

[48] J. Pelleg, L.Z. Zevin, S. Lungo, N. Croitoru, Thin Solid Films 197/1-2 (1991) 117.

[49] U.C. Oh, J.H. Je, J.Y. Lee, J. Mater. Res. 10/3 (1995) 634.

[50] L. Hultman, J.E. Sundgren, J.E. Greene, J. Appl. Phys. 66/2 (1989) 536.

[51] L. Hultman, W.D. Munz, J. Musil, S. Kadlec, I. Petrov, J.E. Greene, J. Vac. Sci. Technol., A 9/3 (1991) 434.

[52] G. Knuyt, C. Quaeyhaegens, J. D'Haen, L.M. Stals, Surf. Coat. Technol. 76-77/Part 1 (1995) 311.

[53] D. Gall, S. Kodambaka, M.A. Wall, I. Petrov, J.E. Greene, J. Appl. Phys. 93/11 (2003) 9086.

[54] J.P. Zhao, X. Wang, Z.Y. Chen, S.Q. Yang, T.S. Shi, X.H. Liu, J. Phys. D: Appl. Phys. 30/1 (1997) 5.

[55] V. Valvoda, J. Musil, Thin Solid Films 149/1 (1987) 49.

[56] S. Mahieu, P. Ghekiere, G. De Winter, R. De Gryse, D. Depla, O.I. Lebedev, Diffusion and Defect Data Pt.B: Solid State Phenomena, 2005, p. 447.

[57] A. Karimi, G. Allidi, R. Sanjines, Surf. Coat. Technol. 201/7 (2006) 4062.

[58] F. Mei, N. Shao, L. Wei, Y. Dong, G. Li, Appl. Phys. Lett. 87/1 (2005) 011906.

[59] L. Hultman, Vacuum 57/1 (2000) 1.

[60] M. Beckers, N. Schell, R.M.S. Martins, A. Mücklich, W. Möller, J. Vac. Sci. Technol., A 23/5 (2005) 1384.

[61] J.Y. Rauch, C. Rousselot, N. Martin, Surf. Coat. Technol. 157/2-3 (2002) 138.

[62] B. Chapman, Glow Discharge Processes - Sputtering and Plasma Etching, John Wiley & Sons, New York, 1980.

[63] M. Ohring, The Materials Science of Thin Films, Academic Press, London, 1992.

[64] G. Franz, Oberflächentechnologie mit Niederdruckplasmen - Beschichten und Strukturieren in der Mikrotechnik, Springer, Berlin, 1998.

[65] P. Sigmund, Appl. Phys. Lett. 14/3 (1969) 114.

[66] W.D. Westwood, Sputter Deposition, AVS, New York, 2003.

[67] A. Kimura, H. Hasegawa, K. Yamada, T. Suzuki, Surf. Coat. Technol. 120-121 (1999) 438.

Publication VI

On the influence of coating and oxidation on the mechanical properties of a γ-TiAl based alloy

M. Moser, P. H. Mayrhofer, H. Clemens

submitted to Intermetallics

On the influence of coating and oxidation on the mechanical properties of a γ-TiAl based alloy

M. Moser, P. H. Mayrhofer, H. Clemens

Department of Physical Metallurgy and Materials Testing, Montanuniversität Leoben,

Franz-Josef Straße 18, A-8700 Leoben, Austria

Abstract

The use of γ-TiAl based alloys in high temperature applications requires an effective protection against oxidation and concomitant loss of ductility. Two coatings, Al_2Au and $Cr_{0.45}Al_{0.53}Y_{0.02}N$ (CrAlYN), are tested for their oxidation protection in air and their influence on the mechanical properties of a Ti-47Al-2Cr-0.2Si alloy. Both coatings significantly improve the oxidation resistance of the investigated γ-TiAl. The plastic strain in the γ-TiAl outer fiber during four-point-bending tests at room temperature is reduced by the deposition with Al_2Au and CrAlYN. After 168 h oxidation at 800 °C uncoated and Al_2Au coated γ-TiAl samples crack without plastic deformation due to the oxide layers and interdiffusion zones formed. Contrary, a CrAlYN protected γ-TiAl four-point bending specimen still exhibits a plastic strain of 0.12 % after oxidation at 800 °C for 672 h, as a thin and dense oxide layer forms. We conclude that CrAlYN is effectively retards oxidation and interdiffusion of γ-TiAl and hence the commonly observed deterioration of mechanical properties by oxidation and interdiffusion is significantly reduced.

Keywords: titanium aluminides, based on TiAl / oxidation /

coatings, CrAlYN, Al-Au / brittleness and ductility

Introduction

Within the Ti-Al system, the 40-50 at.% Al containing alloys – so called γ-TiAl based alloys – exhibit the most attractive properties such as low density, high specific stiffness, high yield strength, and good creep resistance up to high temperatures. Consequently, γ-TiAl alloys have the potential to partly replace heavy steels and Ni-base alloys presently used in high-temperature automotive, aerospace and power-generation applications [1-4]. However, the long-term use of γ-TiAl based alloys in oxidative environments is limited to temperatures below 800 °C because of their poor oxidation resistance [2-7]. Consequently, the latter has to be improved to utilize the full potential of γ -TiAl. Alloying the material with e.g., Nb was shown to be an effective method in terms of oxidation resistance, but also influences the mechanical properties [3, 5, 7, 8].

Improving the oxidation resistance by surface techniques allows the development of γ-TiAl based alloys with application-optimized mechanical properties. Hence, in recent years the effect of halogen ion implantation [9, 10] or magnetron sputter deposited intermetallic coatings on the oxidation of various γ-TiAl based alloys has been studied [11-14]. Also, coating systems known for their good performance on Ni-base superalloys [15, 16] or for protection of tool steels [17, 18] have been tested.

However, due to the relatively low fracture toughness of γ-TiAl based alloys as compared to Ni-base superalloys the influence of the used surface modification on mechanical properties and ductility of γ-TiAl based alloys has to be considered. Contrary to Ni-base superalloys the mechanical properties of γ-TiAl are often reduced by a deposition process [15, 19, 20].

In the present paper we discuss, in addition to oxidation resistance, also the influence of coatings and the deposition process on the ductility of Ti-47Al-2Cr-0.2Si (in at.%) sheet material. The selected coatings, Al_2Au and $Cr_{0.43}Al_{0.53}Y_{0.02}N$ (CrAlYN), exhibit both good oxidation and thermal stability [14, 21, 22]. We show by means of four-point-bending tests that Al_2Au and CrAlYN only slightly reduce the room temperature (RT) bending strength of Ti-47Al-2Cr-0.2Si from 893 to 865 and 855 MPa, respectively. Excellent oxidation resistance with small specific mass gains after 672 h at 800 °C is obtained for CrAlYN and Al_2Au coated Ti-47Al-2Cr-0.2Si, whereas uncoated Ti-47Al-2Cr-0.2Si shows a strong mass gain during oxidation in air. Already after 168 h of oxidation time at 800 °C uncoated

and Al_2Au coated Ti-47Al-2Cr-0.2Si exhibit no plastic deformation as a thick oxide layer and large interdiffusion zone is formed. Contrary to that, four-point-bending specimen coated with CrAlYN can preserve plastic strain of 0.12 % in the outer fiber of γ-TiAl after oxidation at 800 °C for 672 h.

Compared to commercial coatings like pack-cementated Cr-Al, electroplated Ni-Al, and plasma-sprayed CoNiCrAlY, our CrAlYN coating shows better oxidation resistance and lower influence on the mechanical properties of Ti-47Al-2Cr-0.2Si.

Experimental

Intermetallic Al_2Au and $Cr_{0.43}Al_{0.53}Y_{0.02}N$ coatings were deposited by DC magnetron sputtering, a physical vapour deposition (PVD) technique, on specimen with a dimension of 45 x 8 x 1 mm^3 which were produced from Ti-47Al-2Cr-0.2Si sheet-material. This particular γ-TiAl based alloy was selected as substrate material as it exhibits relatively high ductility at room temperature but low oxidation resistance [15]. The 2.5 µm thin CrAlYN film was deposited in a mixed $Ar-N_2$ glow-discharge (0.4 Pa total pressure, ~35% N_2 partial pressure) using a $Cr_{0.36}Al_{0.66}Y_{0.02}$ target (PLANSEE SE, Austria), a sputter-power density of 6.8 W/cm^2, and a substrate temperature of 475 °C [17, 23]. The 8 µm thick Al_2Au coating was deposited in Ar glow discharge from an Al target (Ø 150 mm) with Ø 10 mm Au inlets covering 8.8% of the total target surface. The substrate temperature was 300 °C and the sputter power density was 2.7 W/cm^2. Further details on the deposition parameters are given in Refs. [23, 24].

The films are compared to commercially available coatings, which are routinely used for the oxidation protection of Ni-base superalloys, such as chrome-aluminizing by pack-cementation (Cr-Al coating), nickel-electroplating with subsequent Al-pack cementation (Ni-Al coating), and atmospheric plasma spraying of a layer of CoNiCrAlY. Details on deposition parameters, oxidation resistance and mechanical testing are reported in Refs. [15, 25].

The coated and bare Ti-47Al-2Cr-0.2Si sheets were weighed in a Scaltec SBC21 microbalance before and after isothermal oxidation at 800 °C using a Nabertherm N11/HR box-furnace for one week (168 h) and one month (672 h).

Four-point-bending tests were conducted with a Zwick Z050 machine equipped with a 10 kN load cell. The experimental arrangement is shown in Fig. 1. The tests were carried out

with a cross-head speed of 0.1 mm/min. The bending angle α is calculated from the cross-head displacement according to [25]:

$$\alpha = 2 \cdot \arctan \frac{f}{0.5 \cdot (l - l_p)},$$ (1)

and the bending strength R_{bb} is given by:

$$R_{bb} = \frac{3}{2} \cdot \frac{F \cdot (l - l_p)}{b \cdot h^2},$$ (2)

where F is the applied force, l is the distance between the lower rolls and l_p is the distance between the upper rolls (Fig. 1). The terms b and h denote the width and thickness of the specimen, respectively.

The strain in the outer fibre of the specimens was calculated using [25]:

$$\varepsilon = \frac{4 \cdot h \cdot f \cdot c}{l_p^2},$$ (3)

where f is the cross-head displacement and c is a geometry factor of the bending cell (0.27). Further test conditions were selected as given in Refs. [15, 25] to allow a full comparison of our results with already published data.
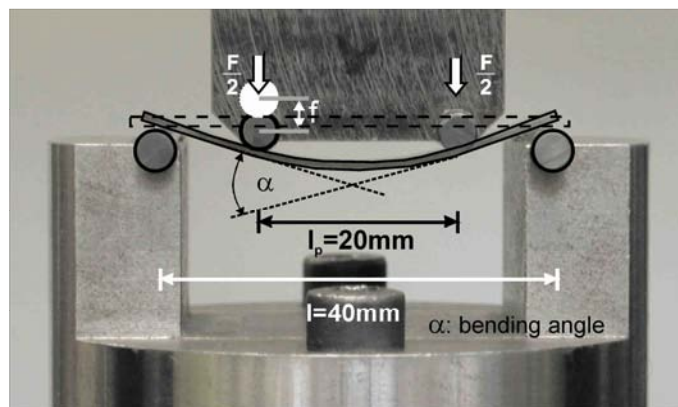

Fig.1 Four-point bending test setup [22].

Fracture surfaces, coating morphologies and interdiffusion were investigated using a Zeiss EVO 50 scanning electron microscope (SEM) equipped with an energy dispersive x-ray analysis (EDX) unit. The EDX line-scans presented are derived from elemental maps and represent an averaged pixel count. They, therefore, do not describe an exact chemical

composition, but give a good overview of the elemental distribution along the coating thickness. Quantitative elemental analyses were done on specific points of interest using metallic Ti, Al, Au, and Al_2O_3 and TiN as standards. Quantification of the latter was obtained by Rutherford backscattering spectroscopy, see Ref. [26]. For the elemental mapping and line-scans of the as-deposited and oxidized sample an electrolytic Ni support film was applied to avoid the removal of the brittle oxide layer during subsequent grinding and polishing steps.

Results and discussion

The oxidation behaviour, characterized by the specific mass change versus time (t) of Ti-47Al-2Cr-0.2Si as well as Al_2Au and CrAlYN coated Ti-47Al-2Cr-0.2Si (in the following referred to as γ-TiAl) after annealing in air at 800 °C is shown in Fig. 2. The unprotected γ-TiAl exhibits a rapidly increasing mass gain to 1.45±0.15 and 8.97±0.78 mg/cm^2 for t = 168 and 672 h, respectively. The coated materials have a much lower mass gain which is 0.79±0.002 and 0.12±0.003 mg/cm^2 after 672 h at 800 °C for Al_2Au and CrAlYN, respectively.
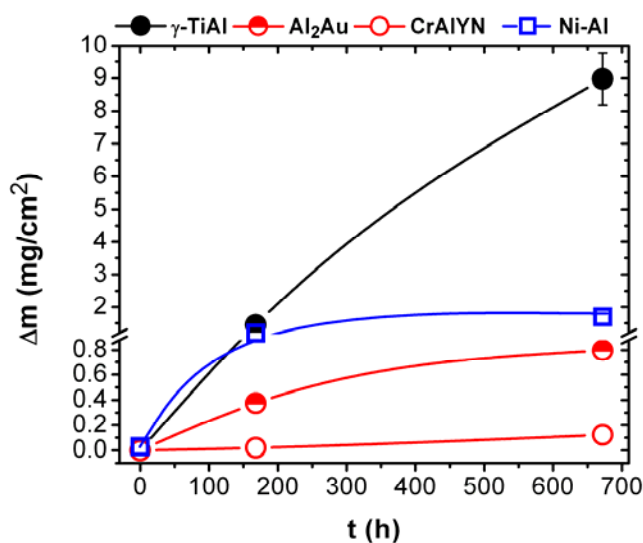

Fig.2 Specific mass change as a function of time during isothermal oxidation in air at 800 °C. The data for Ni-Al coated γ-TiAl, which showed best results in Refs. [15, 16] is added for comparison. The term γ-TiAl stands for the uncoated base material (Ti-47Al-2Cr-0.2Si).

Additionally, the values of γ-TiAl coated with commercial Ni-Al are added to Fig. 2 as they exhibited the best oxidation resistance, published in Refs. [15, 16]. The results clearly demonstrate that CrAlYN is most effective in protecting γ -TiAl against oxidation. Comparing these data to the findings from Refs. [15, 16], the specific mass gain of Ni-Al

coated γ-TiAl of ~0.8 mg/cm^2 is similar to our Al$_2$Au as shown in Fig. 2, but almost 8 times higher than for CrAlYN coated γ-TiAl. The Ni-Al, however, seems to follow a logarithmic mass gain law, whereas the oxidation behaviour of Al$_2$Au fits to a parabolic function.

The cross-sectional back-scattered electron (BSE) SEM image of γ-TiAl after oxidation for 672 h at 800 °C with respective elemental maps for O, Al and Ti are presented in Fig. 3. The material develops a more than 170 µm thick influenced zone composed of several layers. The EDX elemental maps reveal Ti-rich oxide scales at the surface, followed by a non-continuous and porous aluminium-rich region. This layer is reported to provide protection for short but not longer oxidation times [27, 28]. Further away from the surface is a mixed Al- and Ti- oxide layer. These observations correspond to previous investigations reporting rapid oxidation for Ti-47Al-2Cr-0.2Si [15, 25].
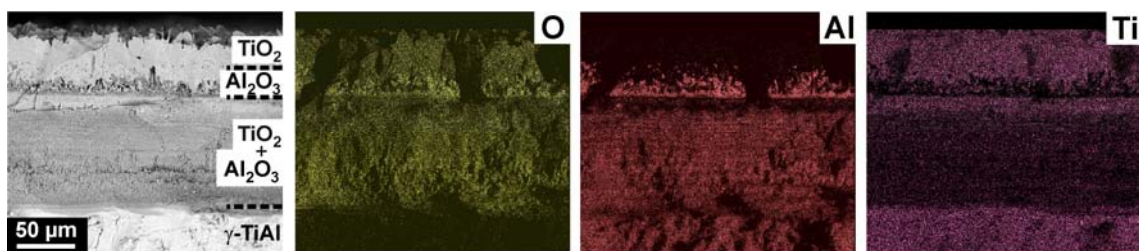

Fig.3 Back-scattered electron (BSE) SEM cross-sectional image of uncoated Ti-47Al-2Cr-0.2Si oxidized for 672 h at 800 °C and the corresponding EDX elemental maps of O, Al and Ti.

Figs. 4a and b present SEM cross-sections of Al$_2$Au- and CrAlYN- coated γ-TiAl, respectively, in the as-deposited state. The 8 µm thick as-deposited Al$_2$Au coating has a dense columnar structure, with a hardness of ~8 GPa and an indentation modulus of ~150 GPa as reported in Refs. [14, 24]. The CrAlYN film has a hardness of ~35 GPa and a modulus of 490 GPa [23], and hence provides additional support against abrasion and wear.
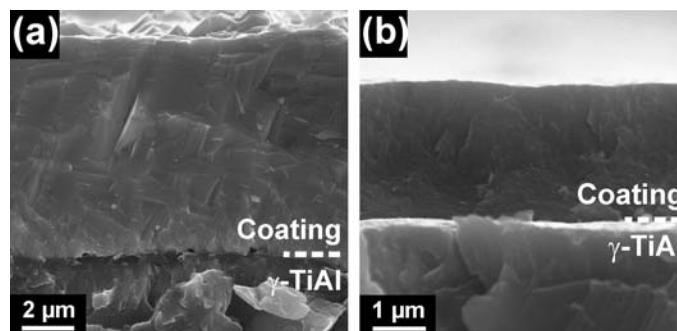

Fig.4 SEM image of the cross-section of as-deposited Al$_2$Au (a) and CrAlYN (b) on γ-TiAl.

In Fig. 5 back-scattered electron (BSE) images and corresponding EDX line-scans are presented of as-deposited CrAlYN and Al_2Au. In the BSE image of the CrAlYN coating (Fig. 5a) a sharp interface between coating and γ-TiAl substrate is visible. The EDX line-scan across the distance (d) from A to B (Fig. 5b) reveals no interdiffusion, with Cr, Al and N intensities in the coating area and only Ti and Al intensities in the substrate zone. Comparable results are obtained for the Al_2Au coated material. The BSE-SEM cross-sectional image in Fig. 5c indicates a sharp interface between coating and substrate and no coating elements are present in γ-TiAl as shown by the EDX line-scan from A to B (Fig. 5d). The increased Au intensity above the coating surface origins from a Au evaporation layer applied prior to the electrolytic Ni support layer preparation step.
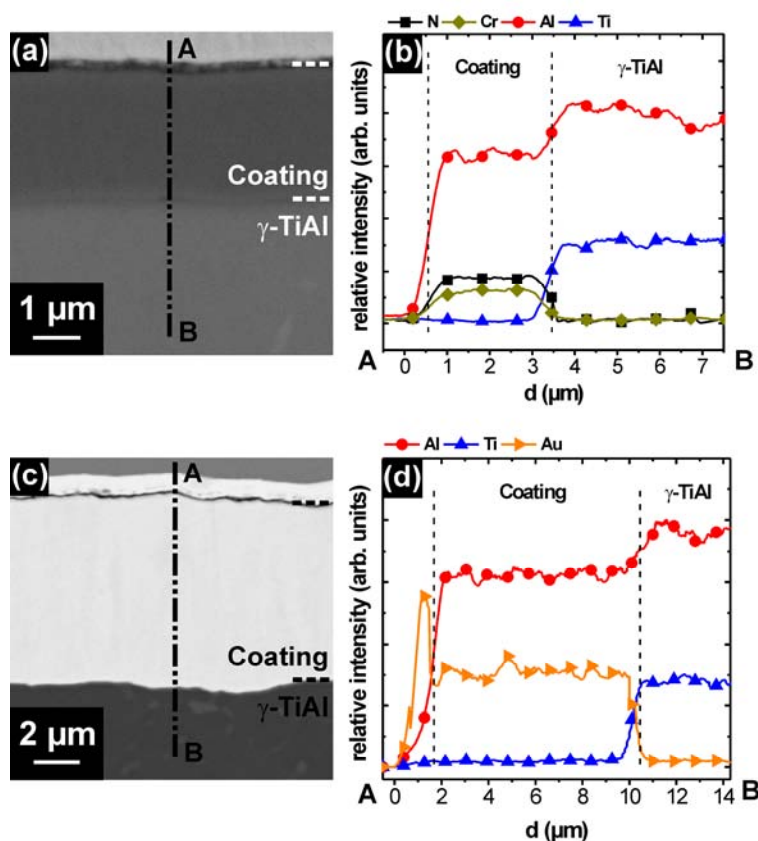

Fig.5 Back-scattered electron (BSE) SEM cross-sectional image and respective EDX line-scan from A to B of as-deposited CrAlYN on Ti-47Al-2Cr-0.2Si in (a) and (b) and BSE SEM cross-sectional image and EDX line-scan from A to B of Al_2Au (c) and (d), respectively.

The effect of 675 h of oxidation at 800 °C on Al_2Au coated γ-TiAl is presented in Fig. 6. The SEM secondary electron image of Fig. 6a reveals a porous, voided and open structure with a dense top layer. A multilayered oxide and diffusion zone is revealed by BSE imaging (Fig. 6b). According to the EDX line scan (Fig. 6c) a top layer of Al_2O_3 and TiO_2

is followed by two ~5 µm thick Au-rich layers, indicated with Au in Figs. 6b and c. The upper Au-rich layer contains Al traces and the second Au-rich layer has an increased Ti content. Underneath these layers is a >30 µm thick diffusion zone where the grain boundaries of the γ-TiAl substrate are enriched with Au. Further, Au is also detected as precipitations present in the oxide scale.
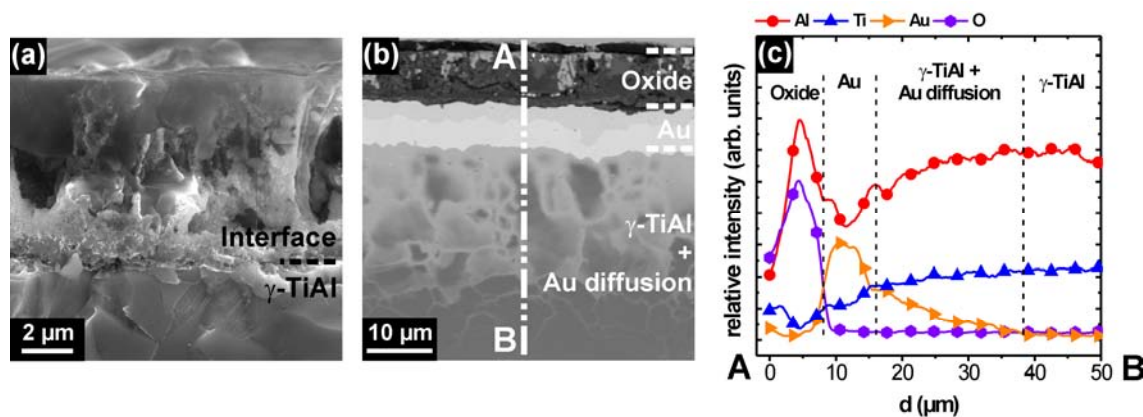

Fig.6 Al$_2$Au on Ti-47Al-2Cr-0.2Si after 672 h at 800 °C. (a) SEM cross-sectional image, (b) BSE-SEM cross-sectional image, and (c) EDX line-scan from A to B.

SEM analyses of CrAlYN coated γ-TiAl, oxidized for 672 h at 800 °C, are presented in Fig. 7. Even after one month of exposure the CrAlYN coating is still dense and uniform, see the SEM cross-sectional image, Fig. 7a. The mass contrasts observable in the BSE-SEM image (Fig. 7b) in combination with the EDX line-scan (Fig. 7c) reveal a ~1 µm oxide scale composed of Al- and Cr-rich oxides. The nitrogen content increases with increasing distance from the surface. Below the oxide a remaining CrAlYN layer is found. Underneath the former coating/γ-TiAl substrate interface an about 7 µm deep spherical diffusion zone depleted in Al and enriched in Ti and N from substrate and coating, respectively, has formed suggesting the formation of TiN [29], as visible by the equally strong Ti and N contents (Fig. 7c), and by the appearance of the semi-circular shaped zone present in the BSE-SEM cross-sectional image (Fig. 7b).

In contrast to our findings, the commercial Cr-Al and Ni-Al coatings exhibit already after deposition strong interdiffusion layers of 50-100 µm thickness, as can be expected after pack-cementation with process temperatures between 900 and 1000 °C. The CoNiCrAlY coating has a small diffusion zone, but a very rough and open microstructure. Upon oxidation only CoNiCrAlY and Ni-Al form a dense oxide layer, whereas strong local attack is reported for Cr-Al, see Refs. [15, 16].
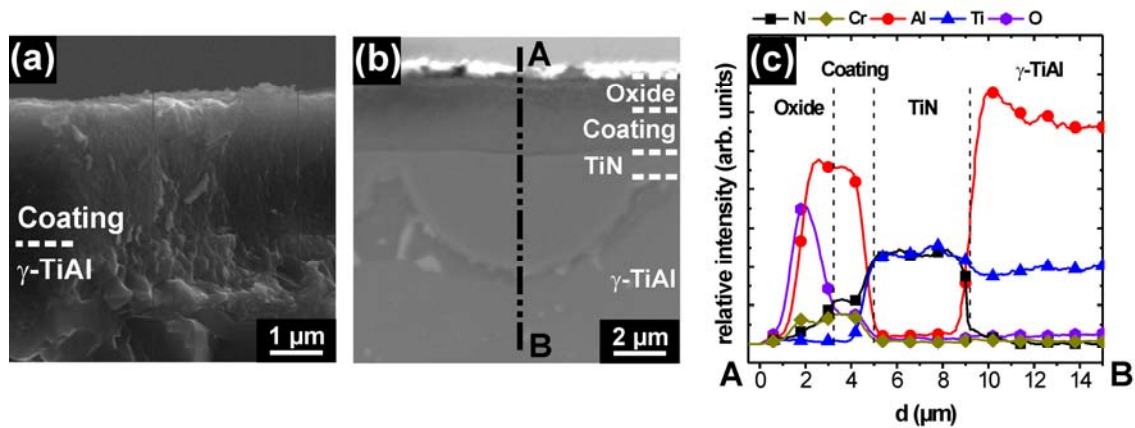
Fig.7 CrAlYN on γ-TiAl after 672 h oxidation at 800 °C in air. (a) SEM cross-sectional image, (b) BSE-SEM cross-sectional image, and (c) EDX line-scan from A to B.

The influence of coatings and thermal exposure in ambient atmosphere at 800 °C for 168 and 672 h on the mechanical properties of γ-TiAl is investigated by four-point-bending tests. The uncoated γ-TiAl has the highest bending strength of 893±55 MPa in the untreated state which rapidly decreases to 646±33 and 612±9 MPa after oxidation at 800 °C for 168 and 672 h, respectively, see Fig. 8. The bending strength before oxidation of γ-TiAl is slightly reduced by the deposition with Al_2Au and CrAlYN to 865±8.5 and 855±26 MPa, respectively.

Also the commercially available films reduce the bending strength of γ-TiAl. For pack cementated Cr-Al and Ni-Al coated γ-TiAl the bending strength is only 420 and 270 MPa and for CoNiCrAlY coated γ-TiAl R_{bb} is 850 MPa, comparable to our coated γ-TiAl [15, 16]. From the as-deposited samples we conclude, that coatings applied with diffusional processes like pack-cementation strongly decrease the strength of γ-TiAl based alloys, due to their thick interdiffusion zones in the range of 50 to 100 μm. We suggest that the much smaller decrease in R_{bb} of γ-TiAl found for PVD or plasma sprayed coatings is due to the much smaller interdiffusion between coating and substrate material.

The strong interdiffusion and the formation of voids during oxidation at 800 °C of Al_2Au coated γ-TiAl result in rapidly decreasing R_{bb} values from 865±26 to 441.0±1.4 and 368.5±12.0 MPa after 168 and 672 h, respectively, see Fig. 8. The highest bending strength after oxidation is obtained for CrAlYN coated γ-TiAl with R_{bb} values of 728.5±17.8 and 731.0±7.0 MPa after 168 and 672 h.
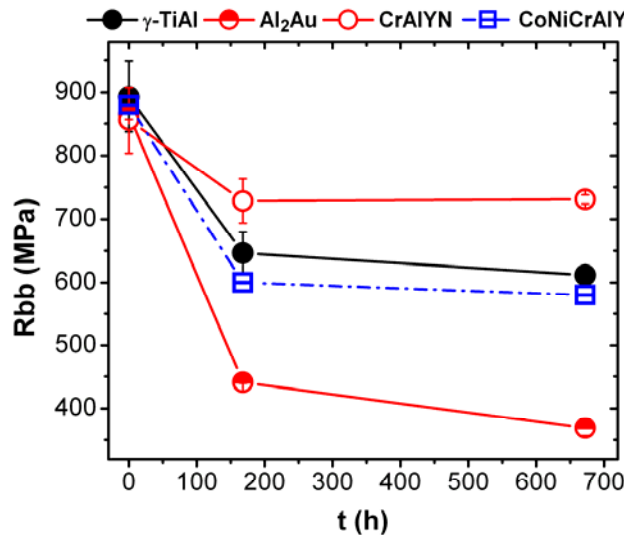
Fig.8 Bending strength R_{bb} after oxidation at 800 °C versus oxidation time. The CoNiCrAlY coating, which showed best results in Refs. [15, 16], is added for comparison.

In the case of the commercial coatings the highest R_{bb} value after oxidation at 800 °C was found for CoNiCrAlY with ~600 and ~580 MPa for t = 168 and 672 h, respectively. The bending strength of the Cr-Al and Ni-Al coated γ-TiAl slightly increased from the as-deposited value to ~570 and ~400 MPa after one month exposure. This is attributed to healing of voids generated during the diffusion based coating process [14, 17]. The R_{bb} values are, however, smaller than for uncoated γ-TiAl and much smaller than for CrAlYN coated γ-TiAl presented here.

Furthermore, the four-point-bending tests are evaluated based on the bending angle α, and the percent of plastic strain in the outer fibre, as presented in Figs. 9a and b. For uncoated γ-TiAl the ductility is drastically reduced with α decreasing from 39.0±2.2° before oxidation to 12.8±0.2 and 9.4±1.0° after one week and one month oxidation at 800 °C, respectively, due to the thick oxide layer formed (see Fig. 3). The plastic contribution to the total deformation in the outer fibre is 0.52 %. After already one week of oxidation no plastic deformation can be observed and the material cracks in the elastic regime. As reported in Refs. [15, 16, 25] the fracture mode of uncoated and Ni-Al, Cr-Al, and CoNiCrAlY coated γ-TiAl is cleavage. We also observed the same fracture mode for uncoated and our coated γ-TiAl.

Due to the strong interdiffusion and the formation of voids during oxidation, the bending angle of Al$_2$Au coated γ -TiAl is even smaller than that of the uncoated material, see Fig. 9a. The bending angle of Al$_2$Au coated γ-TiAl decreases from the as-deposited value of

27.3±0.3° to 9.2±0.5° and 7.9±0.5° after oxidation at 800 °C for 168 and 672 h, respectively. While the plastic strain covers 0.31 % for Al_2Au coated γ-TiAl before oxidation, already after one week of oxidation no plastic deformation is sustained, similar to the uncoated material, see Fig. 9b.

Although the bending angle of γ-TiAl is reduced from 39.0±2.2 to 23.3±2.5° by the deposition with CrAlYN due to its inherent brittleness, it is only further reduced to 16.8±1.6 and 17.4±0.9° after 168 and 672 h of oxidation at 800 °C, respectively (Fig. 9a). Also the plastic strain in the outer fiber is only reduced from the as-deposited value of 0.20 % to about 0.10 - 0.12 % by subsequent oxidation at 800 °C for 168 and 672 h, as shown in Fig. 9b.
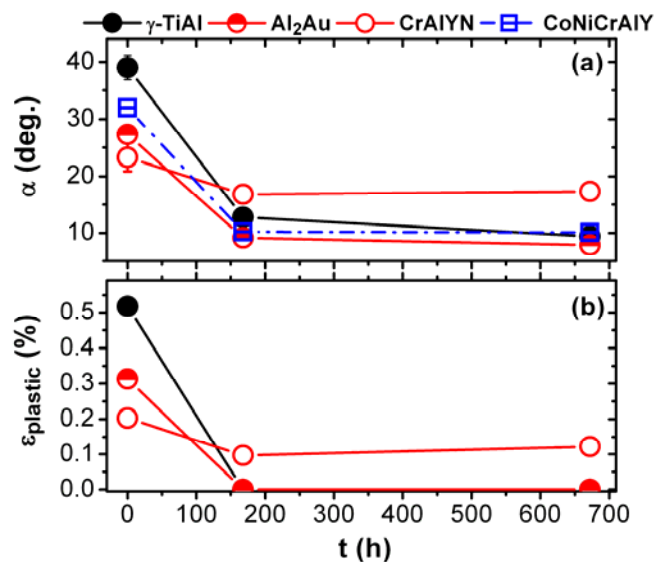

Fig.9 (a) Bending angle (α) and (b) plastic strain ($\varepsilon_{plastic}$) as a function of oxidation time (t). In (a) the data for CoNiCrAlY coated γ-TiAl, which showed best results in Refs. [15, 16] is added for comparison.

These results are much better than obtained for the commercial coatings with as-deposited bending angles of ~7.5, 8, and 32° for γ-TiAl coated with Ni-Al, Cr-Al, and CoNiCrAlY, respectively. After one week of oxidation, Ni-Al and Cr-Al coated γ-TiAl exhibit a bending angle of ~10.5 and 8.5°, whereas α for CoNiCrAlY coated γ -TiAl is reduced to ~10° (Fig. 9a). For all commercial protective coatings, α stays almost constant and no plastic deformation is observed if the oxidation time at 800 °C is longer than ~150 h.

Consequently, only our CrAlYN coated γ-TiAl samples deform plastically after annealing in ambient atmosphere at 800 °C, as CrAlYN provides both best oxidation and interdiffusion protection for the base material.

Conclusions

The low fracture toughness, ductility and oxidation resistance of γ-TiAl based alloys require the application of coatings with excellent oxidation and interdiffusion protection.

An intermetallic Al_2Au coating, which exhibits good oxidation resistance with relatively small specific mass gain after 672 h oxidation at 800 °C, exhibits a decomposed microstructure, formation of pores and a severe interdiffusion zone of ~30 µm thickness. Therefore, the ductility is even smaller than for unprotected Ti-47Al-2Cr-0.2Si having an oxidation influenced surface zone of ~170 µm.

CrAlYN provides the best oxidation resistance for γ-TiAl with a mass gain of only 0.12 mg/cm^2 in combination with the smallest interdiffusion zone (~7 µm) of all coatings tested after one month exposure at 800 °C in air. Consequently, CrAlYN coated Ti-47Al-2Cr-0.2Si shows the best performance during (RT) four-point-bending tests exhibiting plastic deformation even after long-term oxidation at 800 °C.

Based on our results we can conclude that CrAlYN, which provides excellent oxidation and interdiffusion resistance, is a very promising coating for the protection of γ-TiAl based alloys at elevated temperatures.

Acknowledgment

References

[1]   H. Clemens, H. Chladil, W. Wallgram, B. Böck, S. Kremmer, A. Otto, V. Güther, A. Bartels, Structural Aluminides for Elevated Temperature Applications, The Minerals, Metals & Materials Society, 137th Annual Meeting Proceedings, Wiley-VCH, New Orleans, 2008, p. in print.

[2]   H. Clemens, H. Kestler, Adv. Eng. Mat. 2/9 (2000) 551.

[3]   F. Appel, M. Oehring, in: C. Leyens, M. Peters (Eds.), Titanium and Titanium Alloys: Fundamentals and Applications, Wiley-VCH, Weinheim, 2003, p. 89.

[4]   H. Kestler, H. Clemens, in: C. Leyens, M. Peters (Eds.), Titanium and Titanium Alloys: Fundamentals and Applications, Wiley-VCH GmbH & Co. KGaA, Weinheim, 2003, p. 351.

[5]   V.A.C. Haanappel, H. Clemens, M.F. Stroosnijder, Intermetallics 10/3 (2002) 293.

[6]   V.A.C. Haanappel, M.F. Stroosnijder, Surf. Coat. Technol. 105/1-2 (1998) 147.

[7]   V.A.C. Haanappel, J.D. Sunderkotter, M.F. Stroosnijder, Intermetallics 7/5 (1999) 529.

[8]   H.F. Chladil, H. Clemens, H. Leitner, A. Bartels, R. Gerling, F.P. Schimansky, S. Kremmer, Intermetallics 14/10-11 (2006) 1194.

[9]   A. Donchev, E. Richter, M. Schutze, R. Yankov, J. Alloys Compd. 452/1 (2008) 7.

[10]   A. Donchev, E. Richter, M. Schutze, R. Yankov, Intermetallics 14/10-11 (2006) 1168.

[11]   M. Fröhlich, R. Braun, C. Leyens, Surf. Coat. Technol. 201/7 (2006) 3911.

[12]   R. Braun, M. Frohlich, W. Braue, C. Leyens, Surf. Coat. Technol. 202/4-7 (2007) 676.

[13]   M. Moser, P.H. Mayrhofer, R. Braun, Materials Research Society Symposium Proceedings, 2007, p. 431.

[14]   M. Moser, P.H. Mayrhofer, I.M. Ross, W.M. Rainforth, J. Vac. Sci. Technol., A 25/5 (2007) 1402.

[15]   H.-P. Martinz, H. Clemens, W. Knabl, in: Y.-W. Kim, D.M. Dimiduk, M.H. Loretto (Eds.), Gamma Titanium Aluminides - The Minerals, Metals & Materials Society, Warrandale, Pa., 1999, p. 829.

[16]   H.-P. Martinz, H. Clemens, W. Knabl, in: G. Kneringer, P. Rödhammer, P. Wilhartitz (Eds.), 14th International Plansee Seminar, Plansee AG, Reutte, 1997, p. 887.

[17]   F. Rovere, P.H. Mayrhofer, J. Vac. Sci. Technol., A 26/1 (2008) 29.

[18]   R. Braun, D. Müßener, M. Moser, F. Rovere, P.H. Mayerhofer, C. Leyens, Structural Aluminides for elevated Temperature Application, The Minerals, Metals & Materials Society, 137th annual meeting proceedings, New Orleans, 2008.

[19]   C.H. Koo, T.H. Yu, Surf. Coat. Technol. 126/2-3 (2000) 171.

[20]   G.W. Goward, Surf. Coat. Technol. 108-109/1-3 (1998) 73.

[21] F. Rovere, P.H. Mayrhofer, J.M. Schneider, A. Reinholdt, J. Mayer, Surf. Coat. Technol. submitted (2008).

[22] M. Moser, P.H. Mayrhofer, H. Clemens, Structural Aluminides for Elevated Temperature Applications, The Minerals, Metals & Materials Society, 137th Annual Meeting Proceedings, Wiley-VCH, New Orleans, 2008, p. in print.

[23] F. Rovere, P.H. Mayrhofer, J. Vac. Sci. Technol., A 25/5 (2007) 1336.

[24] M. Moser, P.H. Mayrhofer, I.M. Ross, W.M. Rainforth, J. Appl. Phys. 102/2 (2007).

[25] J.D. Sunderkötter, W. Knabl, H.-P. Martinz, H. Clemens, M.F. Stroosnijder, in: Y.-W. Kim, D.M. Dimiduk, M.H. Loretto (Eds.), Gamma Titanium Aluminides - The Minerals, Metals & Materials Society, Warrandale, Pa, 1999, p. 769.

[26] P.H. Mayrhofer, F. Kunc, J. Musil, C. Mitterer, Thin Solid Films 415/1-2 (2002) 151.

[27] C. Lang, M. Schütze, in: H.J. Grabke, M. Schütze (Eds.), Oxidation of Intermetallics, Wiley-VCH Verlag GmbH, Weinheim, 1996, p. 245.

[28] F. Dettenwanger, E. Schumann, J. Rakowski, G.H. Meier, M. Rühle, in: H.J. Grabke, M. Schütze (Eds.), Oxidation of Intermetallics, Wiley-VCH Verlag GmbH, Weinheim, 1996, p. 265.

[29] P.H. Mayrhofer, F. Rovere, M. Moser, C. Strondl, R. Tietema, Scripta Mater 57/3 (2007) 249.